



# Jordan Journal of PHYSICS

An International Peer-Reviewed Research Journal

Volume 11, No. 1, April 2018, Shaban 1439 H

**Jordan Journal of Physics (JJP):** An International Peer-Reviewed Research Journal funded by the Scientific Research Support Fund, Jordan, and published biannually by the Deanship of Research and Graduate Studies, Yarmouk University, Irbid, Jordan.

**EDITOR-IN-CHIEF:**

**Ibrahim O. Abu Al-Jarayesh**

*Department of Physics, Yarmouk University, Irbid, Jordan.*

*[ijaraysh@yu.edu.jo](mailto:ijaraysh@yu.edu.jo)*

EDITORIAL BOARD:	ASSOCIATE EDITORIAL BOARD
<p><b>Prof. Dia-Eddin M. Arafah</b> <i>President, AL- al Bait University, Mafrqa, Jordan.</i> <i><a href="mailto:darafah@ju.edu.jo">darafah@ju.edu.jo</a></i></p> <p><b>Prof. Nabil Y. Ayoub</b> <i>President, American University of Madaba, Madaba, Jordan.</i> <i><a href="mailto:nabil.ayoub@gju.edu.jo">nabil.ayoub@gju.edu.jo</a></i></p> <p><b>Prof. Jamil M. Khalifeh</b> <i>Department of Physics, University of Jordan, Amman, Jordan.</i> <i><a href="mailto:jkhalifa@ju.edu.jo">jkhalifa@ju.edu.jo</a></i></p> <p><b>Prof. Sami H. Mahmood</b> <i>Department of Physics, University of Jordan, Amman, Jordan.</i> <i><a href="mailto:s.mahmood@ju.edu.jo">s.mahmood@ju.edu.jo</a></i></p> <p><b>Prof. Nihad A. Yusuf</b> <i>Princess Sumaya University for Technology, Amman, Jordan.</i> <i>E-mail: <a href="mailto:n.yusuf@psut.edu.jo">n.yusuf@psut.edu.jo</a></i></p> <p><b>Prof. Marwan S. Mousa</b> <i>Department of Physics, Mu'tah University, Al-Karak, Jordan.</i> <i><a href="mailto:mmousa@mutah.edu.jo">mmousa@mutah.edu.jo</a></i></p> <p><b>Prof. Akram A. Rousan</b> <i>Department of Applied Physical Sciences, Jordan University Of Science and Technology, Irbid, Jordan.</i> <i><a href="mailto:akram@just.edu.jo">akram@just.edu.jo</a></i></p> <p><b>Prof. Mohammad Al-Sugheir</b> <i>Department of Physics, The Hashemite University, Zarqa, Jordan.</i> <i><a href="mailto:msugh@hu.edu.jo">msugh@hu.edu.jo</a></i></p>	<p><b>Prof. Mark Haggmann</b> <i>Desert Electronics Research Corporation, 762 Lacey Way, North Salt Lake 84064, Utah, U. S. A.</i> <i><a href="mailto:MHaggmann@NewPathResearch.Com">MHaggmann@NewPathResearch.Com</a></i></p> <p><b>Prof. Richard Forbes</b> <i>University of Surrey, FEPS (X1), Guildford, Surrey GU2 7XH, U. K.</i> <i><a href="mailto:R.Forbes@surrey.ac.uk">R.Forbes@surrey.ac.uk</a></i></p> <p><b>Prof. Roy Chantrell</b> <i>Physics Department, The University of York, York, YO10 5DD, UK.</i> <i><a href="mailto:roy.chantrell@york.ac.uk">roy.chantrell@york.ac.uk</a></i></p> <p><b>Prof. Susamu Taketomi</b> <i>2-35-8 Higashisakamoto, Kagoshima City, 892-0861, Japan.</i> <i><a href="mailto:staketomi@hotmail.com">staketomi@hotmail.com</a></i></p>

**Editorial Secretary:** Majdi Al-Shannaq.

**Manuscripts should be submitted to:**

Prof. Ibrahim O. Abu Al-Jarayesh  
Editor-in-Chief, Jordan Journal of Physics  
Deanship of Research and Graduate Studies  
Yarmouk University-Irbid-Jordan  
Tel. 00 962 2 7211111 Ext. 2075  
E-mail: [jjp@yu.edu.jo](mailto:jjp@yu.edu.jo)  
Website: <http://Journals.yu.edu.jo/jjp>

# Jordan Journal of PHYSICS

An International Peer-Reviewed Research Journal

---

Volume 11, No. 1, April 2018, Shaban 1439 H

---

## INTERNATIONAL ADVISORY BOARD

**Prof. Dr. Ahmad Saleh**

*Department of Physics, Yarmouk University, Irbid, Jordan.*  
[salema@yu.edu.jo](mailto:salema@yu.edu.jo)

**Prof. Dr. Aurore Savoy-Navarro**

*LPNHE Université de Paris 6/IN2P3-CNRS, Tour 33, RdC 4,  
Place Jussieu, F 75252, Paris Cedex 05, France.*  
[auore@lpnhep.in2p3.fr](mailto:auore@lpnhep.in2p3.fr)

**Prof. Dr. Bernard Barbara**

*Laboratoire Louis Neel, Salle/Room: D 108, 25, Avenue des  
Martyrs BP 166, 38042-Grenoble Cedex 9, France.*  
[Barbara@grenoble.cnrs.fr](mailto:Barbara@grenoble.cnrs.fr)

**Prof. Dr. Bruno Guiderdoni**

*Observatoire Astronomique de Lyon, g, avenue Ch. Antre-F-69561,  
Saint Genis Laval Cedex, France.*  
[Bruno.guiderdoni@olos.univ-lyon1.fr](mailto:Bruno.guiderdoni@olos.univ-lyon1.fr)

**Prof. Dr. Buford Price**

*Physics Department, University of California, Berkeley, CA 94720,  
U. S. A.*  
[bprice@berkeley.edu](mailto:bprice@berkeley.edu)

**Prof. Dr. Colin Cough**

*School of Physics and Astronomy, University of Birmingham, B15  
2TT, U. K.*  
[c.gough@bham.ac.uk](mailto:c.gough@bham.ac.uk)

**Prof. Dr. Desmond Cook**

*Department of Physics, Condensed Matter and Materials Physics  
Research Group, Old Dominion University, Norfolk, Virginia  
23529, U. S. A.*  
[Dcook@physics.odu.edu](mailto:Dcook@physics.odu.edu)

**Prof. Dr. Evgeny Sheshin**

*MIPT, Institutskij per. 9, Dogoprudnyi 141700, Russia.*  
[sheshin@lafeet.mipt.ru](mailto:sheshin@lafeet.mipt.ru)

**Prof. Dr. Hans Ott**

*Laboratorium Fuer Festkorperphysik, ETH Honggerberg, CH-  
8093 Zurich, Switzerland.*  
[ott@solid.phys.ethz.ch](mailto:ott@solid.phys.ethz.ch)

**Prof. Dr. Herwig Schopper**

*President SESAME Council, Chairman Scientific Board UNESCO  
IBSP Programme, CERN, 1211 Geneva, Switzerland.*  
[Herwig.Schopper@cern.ch](mailto:Herwig.Schopper@cern.ch)

**Prof. Dr. Humam Ghassib**

*Department of Physics, The University of Jordan, Amman 11942,  
Jordan.*  
[humamg@ju.edu.jo](mailto:humamg@ju.edu.jo)

**Prof. Dr. Khalid Touqan**

*Chairman of Jordan Atomic Energy Commission, Amman, Jordan.*

**Prof. Dr. Nasr Zubeidey**

*President: Al-Zaytoonah University of Jordan, Amman, Jordan.*  
[President@alzaytoonah.edu.jo](mailto:President@alzaytoonah.edu.jo)

**Prof. Dr. Patrick Roudeau**

*Laboratoire de l'Accelérateur, Lineaire (LAL), Université Paris-  
Sud 11, Batiment 200, 91898 Orsay Cedex, France.*  
[roudeau@mail.cern.ch](mailto:roudeau@mail.cern.ch)

**Prof. Dr. Paul Chu**

*Department of Physics, University of Houston, Houston, Texas  
77204-5005, U. S. A.*  
[Ching-Wu.Chu@mail.uh.edu](mailto:Ching-Wu.Chu@mail.uh.edu)

**Prof. Dr. Peter Dowben**

*Nebraska Center for Materials and Nanoscience, Department of  
Physics and Astronomy, 255 Behlen Laboratory (10th and R  
Streets), 116 Brace Lab., P. O. Box 880111, Lincoln, NE 68588-  
0111, U. S. A.*  
[pdowben@unl.edu](mailto:pdowben@unl.edu)

**Prof. Dr. Peter Mulser**

*Institute fuer Physik, T.U. Darmstadt, Hochschulstr. 4a, 64289  
Darmstadt, Germany.*  
[Peter.mulser@physik.tu-darmstadt.de](mailto:Peter.mulser@physik.tu-darmstadt.de)

**Prof. Dr. Rasheed Azzam**

*Department of Electrical Engineering, University of New Orleans  
New Orleans, Louisiana 70148, U. S. A.*  
[razzam@uno.edu](mailto:razzam@uno.edu)

**Prof. Dr. Shawqi Al-Dallal**

*Department of Physics, Faculty of Science, University of Bahrain,  
Manamah, Kingdom of Bahrain.*

**Prof. Dr. Wolfgang Nolting**

*Institute of Physics / Chair: Solid State Theory, Humboldt-  
University at Berlin, Newtonstr. 15 D-12489 Berlin, Germany*  
[Wolfgang.nolting@physik.hu-berlin.de](mailto:Wolfgang.nolting@physik.hu-berlin.de)

**Prof. Dr. Ingo Hofmann**

*GSI Darmstadt, Planckstr. 1, 64291, Darmstadt, Germany.*  
[i.hofmann@gsi.de](mailto:i.hofmann@gsi.de)

**Prof. Dr. Jozef Lipka**

*Department of Nuclear Physics and Technology, Slovak University  
of Technology, Bratislava, Ilkovicova 3, 812 19 Bratislava,  
Slovakia.*  
[Lipka@elf.stuba.sk](mailto:Lipka@elf.stuba.sk)





The Hashemite Kingdom of Jordan



Yarmouk University

Jordan Journal of  
**PHYSICS**

An International Peer-Reviewed Research Journal  
Funded by the Scientific Research Support Fund

**Special Issue**

**Volume 11, No. 1, April 2018, Shaban 1439 H**



## Instructions to Authors

Instructions to authors concerning manuscript organization and format apply to hardcopy submission by mail, and also to electronic online submission via the Journal homepage website (<http://jjp.yu.edu.jo>).

### Manuscript Submission

1- **E-mail to :** [jjp@yu.edu.jo](mailto:jjp@yu.edu.jo)

2- **Online:** Follow the instructions at the journal homepage website.

Original *Research Articles*, *Communications* and *Technical Notes* are subject to critical review by minimum of two competent referees. Authors are encouraged to suggest names of competent reviewers. *Feature Articles* in active Physics research fields, in which the author's own contribution and its relationship to other work in the field constitute the main body of the article, appear as a result of an invitation from the Editorial Board, and will be so designated. The author of a *Feature Article* will be asked to provide a clear, concise and critical status report of the field as an introduction to the article. *Review Articles* on active and rapidly changing Physics research fields will also be published. Authors of *Review Articles* are encouraged to submit two-page proposals to the Editor-in-Chief for approval. Manuscripts submitted in *Arabic* should be accompanied by an Abstract and Keywords in English.

### Organization of the Manuscript

Manuscripts should be typed double spaced on one side of A4 sheets (21.6 x 27.9 cm) with 3.71 cm margins, using Microsoft Word 2000 or a later version thereof. The author should adhere to the following order of presentation: Article Title, Author(s), Full Address and E-mail, Abstract, PACS and Keywords, Main Text, Acknowledgment. Only the first letters of words in the Title, Headings and Subheadings are capitalized. Headings should be in **bold** while subheadings in *italic* fonts.

**Title Page:** Includes the title of the article, authors' first names, middle initials and surnames and affiliations. The affiliation should comprise the department, institution (university or company), city, zip code and state and should be typed as a footnote to the author's name. The name and complete mailing address, telephone and fax numbers, and e-mail address of the author responsible for correspondence (designated with an asterisk) should also be included for official use. The title should be carefully, concisely and clearly constructed to highlight the emphasis and content of the manuscript, which is very important for information retrieval.

**Abstract:** A one paragraph abstract not exceeding 200 words is required, which should be arranged to highlight the purpose, methods used, results and major findings.

**Keywords:** A list of 4-6 keywords, which expresses the precise content of the manuscript for indexing purposes, should follow the abstract.

**PACS:** Authors should supply one or more relevant PACS-2006 classification codes, (available at <http://www.aip.org/pacs/pacs06/pacs06-toc.html>)

**Introduction:** Should present the purpose of the submitted work and its relationship to earlier work in the field, but it should not be an extensive review of the literature (e.g., should not exceed 1 ½ typed pages).

**Experimental Methods:** Should be sufficiently informative to allow competent reproduction of the experimental procedures presented; yet concise enough not to be repetitive of earlier published procedures.

**Results:** should present the results clearly and concisely.

**Discussion:** Should be concise and focus on the interpretation of the results.

**Conclusion:** Should be a brief account of the major findings of the study not exceeding one typed page.

**Acknowledgments:** Including those for grant and financial support if any, should be typed in one paragraph directly preceding the References.

**References:** References should be typed double spaced and numbered sequentially in the order in which they are cited in the text. References should be cited in the text by the appropriate Arabic numerals, enclosed in square brackets. Titles of journals are abbreviated according to list of scientific periodicals. The style and punctuation should conform to the following examples:

**1. Journal Article:**

- a) Heisenberg, W., Z. Phys. 49 (1928) 619.
- b) Bednorz, J. G. and Müller, K. A., Z. Phys. B64 (1986) 189
- c) Bardeen, J., Cooper, L.N. and Schrieffer, J. R., Phys. Rev. 106 (1957) 162.
- d) Asad, J. H., Hijjawi, R. S., Sakaji, A. and Khalifeh, J. M., Int. J. Theor. Phys. 44(4) (2005), 3977.

**2. Books with Authors, but no Editors:**

- a) Kittel, C., "Introduction to Solid State Physics", 8<sup>th</sup> Ed. (John Wiley and Sons, New York, 2005), chapter 16.
- b) Chikazumi, S., C. D. Graham, JR, "Physics of Ferromagnetism", 2<sup>nd</sup> Ed. (Oxford University Press, Oxford, 1997).

**3. Books with Authors and Editors:**

- a) Allen, P. B. "Dynamical Properties of Solids", Ed. (1), G. K. Horton and A. A. Maradudin (North-Holland, Amsterdam, 1980), p137.
- b) Chantrell, R. W. and O'Grady, K., "Magnetic Properties of Fine Particles" Eds. J. L. Dormann and D. Fiorani (North-Holland, Amsterdam, 1992), p103.

**4. Technical Report:**

Purcell, J. "The Superconducting Magnet System for the 12-Foot Bubble Chamber", report ANL/HEP6813, Argonne Natl. Lab., Argonne, III, (1968).

**5. Patent:**

Bigham, C. B., Schneider, H. R., US patent 3 925 676 (1975).

**6. Thesis:**

Mahmood, S. H., Ph.D. Thesis, Michigan State University, (1986), USA (Unpublished).

**7. Conference or Symposium Proceedings:**

Blandin, A. and Lederer, P. Proc. Intern. Conf. on Magnetism, Nottingham (1964), P.71.

**8. Internet Source:**

Should include authors' names (if any), title, internet website, URL, and date of access.

**9. Prepublication online articles (already accepted for publication):**

Should include authors' names (if any), title of digital database, database website, URL, and date of access.

For other types of referenced works, provide sufficient information to enable readers to access them.

**Tables:** Tables should be numbered with Arabic numerals and referred to by number in the Text (e.g., Table 1). Each table should be typed on a separate page with the legend above the table, while explanatory footnotes, which are indicated by superscript lowercase letters, should be typed below the table.

**Illustrations:** Figures, drawings, diagrams, charts and photographs are to be numbered in a consecutive series of Arabic numerals in the order in which they are cited in the text. Computer-generated illustrations and good-quality digital photographic prints are accepted. They should be black and white originals (not photocopies) provided on separate pages and identified with their corresponding numbers. Actual size graphics should be provided, which need no further manipulation, with lettering (Arial or Helvetica) not smaller than 8 points, lines no thinner than 0.5 point, and each of uniform density. All colors should be removed from graphics except for those graphics to be considered for publication in color. If graphics are to be submitted digitally, they should conform to the following minimum resolution requirements: 1200 dpi for black and white line art, 600 dpi for grayscale art, and 300 dpi for color art. All graphic files must be saved as TIFF images, and all illustrations must be submitted in the actual size at which they should appear in the journal. Note that good quality hardcopy original illustrations are required for both online and mail submissions of manuscripts.

**Text Footnotes:** The use of text footnotes is to be avoided. When their use is absolutely necessary, they should be typed at the bottom of the page to which they refer, and should be cited in the text by a superscript asterisk or multiples thereof. Place a line above the footnote, so that it is set off from the text.

**Supplementary Material:** Authors are encouraged to provide all supplementary materials that may facilitate the review process, including any detailed mathematical derivations that may not appear in whole in the manuscript.



## Revised Manuscript and Computer Disks

Following the acceptance of a manuscript for publication and the incorporation of all required revisions, authors should submit an original and one more copy of the final disk containing the complete manuscript typed double spaced in Microsoft Word for Windows 2000 or a later version thereof. All graphic files must be saved as PDF, JPG, or TIFF images.

Allen, P.B., “.....”, in: Horton, G.K., and Muradudin, A. A., (eds.), “Dynamical.....”, (North.....), pp....

## Reprints

Twenty (20) reprints free of charge are provided to the corresponding author. For orders of more reprints, a reprint order form and prices will be sent with the article proofs, which should be returned directly to the Editor for processing.

## Copyright



Submission is an admission by the authors that the manuscript has neither been previously published nor is being considered for publication elsewhere. A statement transferring copyright from the authors to Yarmouk University is required before the manuscript can be accepted for publication. The necessary form for such transfer is supplied by the Editor-in-Chief. Reproduction of any part of the contents of a published work is forbidden without a written permission by the Editor-in-Chief.

## Disclaimer

Opinions expressed in this Journal are those of the authors and neither necessarily reflects the opinions of the Editorial Board or the University, nor the policy of the Higher Scientific Research Committee or the Ministry of Higher Education and Scientific Research. The publisher shoulders no responsibility or liability whatsoever for the use or misuse of the information published by JJP.

## Indexing

JJP is currently indexing in:

	<b>Emerging Sources Citation Index (ESCI)</b>	
---	---	---



Jordan Journal of  
P H Y S I C S

An International Peer-Reviewed Research Journal

---

---

Volume 11, No. 1, April 2018, Shaban 1439 H

---

---

**Editorial Preface**

This special issue of Jordan Journal of Physics (JJP) presents 8 selected papers presented at the international conference that was held under the patronage of HRH Princess Sumaya bint El Hassan and hosted by Al al-Bayt University between 27-29/4/2017 in Mafraq/ Jordan under the title: "Jordanian Life Sciences for Sustainable Development (JLSSD)". These papers were subjected to standard refereeing of JJP.



Jordan Journal of  
**PHYSICS**

An International Peer-Reviewed Research Journal

---

---

Volume 11, No. 1, April 2018, Shaban 1439 H

---

---

**4th Int. Conf. on Materials in Jordan:  
Jordanian Life Sciences for Sustainable Development (JLSSD)  
April 27 – 29<sup>th</sup> 2017  
Al al-Bayt University, Mafraq, Jordan**

**Conference Preface**

Previously organized, Int. Conferences/ Humboldt Kollegs and workshops, were held between 2008 – 2011. Workshops have dealt with Archaeology, Water or Astronomy while the two conferences in 2009 and 2011 dealt with materials in Jordan. The 3<sup>rd</sup> Int. Conf. in 2014 dealt with "Building Int. Networks for Enhancement of Research in Jordan".

Although these conferences had the German Jordanian University (GJU) as the only academic institution that took part in the organization of the first Conference in 2009. Ten universities and institutions were involved in the organization of the conference in 2011, which reflects the wide interest in the activities which the Jordanian Club of Humboldt Fellows (JCHF) organizes. Patronage of these Kollegs ranged from Prime Minister to Ministers of Higher Education and Scientific research and to the Minister of Energy and Mineral Resources.

The Conf. in 2014 titled "Research Enhancement in Jordan" and the role of networks in this effect was held with contributions from various research topics ranging from, chemistry, physics, pharmacy, humanities, arts, medicine and archaeology.

Her Royal highness (HRH) Princess Sumaya Bint El Hassan, president of the El Hassan Science City, Chairman of the Royal Scientific Society, patronized the Conf. providing her vision at the importance of networks to enhance research. Minister of Higher Education and Scientific Research introduced how best to invest in Int. cooperation.

This 4<sup>th</sup> Int. Conf. held between April 27 -29<sup>th</sup>, 2017 "Jordanian Life Sciences for Sustainable Development" at Al al-Bayt University in Mafraq was held under the patronage of HRH Princess Sumaya Bint El Hassan. Nobel Prize winner, German scientist Professor "Erwin Neher" from the Max Planck Institute for Biophysical Chemistry, Goettingen, was the main invited Keynote speaker who gave a talk titled "Ion Channels: their discovery, their function,, and their role in disease." That lecture was attended by 300 hundred Professors, students and specialists. The conference has been dedicated to Nelia Wanderka the top German scientist and leader in German-Jordanian cooperation.

Opening talks were given by: Prof. Marwan S. Mousa, President of JCHF, Ambassador of Germany HE Brigitta Siefker-Eberle, Prof. Hani Hayajneh, Ambassador Scientist of Alexander von Humboldt Foundation (AvH), Chairman of the Conf. Prof. Dia Eddin Arafah, president of AABU. This was closed by the talk of Minister Mohammad Hamdan representing HRH Princess Sumaya Bint El Hassan.

Present in the Conf. were top scientists, Chairmen of the AvH Associations in MENA region and Europe, Dr. Jaime Sperberg, first Sec. and head of Cultural Dept. of the German Embassy in Jordan, Gabrielle von Fircks the Director of DAAD in Jordan, Katharina Schmidt Director of German Protestant Institute of Archaeology, Dr. Rene Klaff head of Regional office of Friederich Naumann Foundation for MENA.

Workshops on various topics related to life sciences were held. Young scientists participated at two days pre-Conf. training workshop, held at the Det. of Physics, The University of Jordan, chaired by Prof. Dr. Hans Limbach from FU/Berlin and involved eleven postgraduate students from six MENA countries (Syria, Egypt, Tunis, Algeria, Gaza and Jordan).

All these Conferences were supported by the **Science Research Support Fund** in Jordan and the **AvH**.

Tours after the Conference were organized to enable participants to visit Universities, research institutions in addition to visiting main historic sites of Jordan.

Fully refereed proceedings were published, at excellent Journals, from all these Int. conferences. Volume 8 with two issues 2 and 3 were published at JJP in 2015. From this 4<sup>th</sup> Int Conference, an issue with top articles and contributions was published at Applied Microscopy V 47, No 3, Sept. 2017 and excellent articles will appear in this JJP volume. Contributions in this JJP issue come from top Int. scientists and labs such as Helmholtz Berlin Zentrum for Materials and Energy, GSI Helmholtz Zentrum, Darmshtadt, Los Alamos National lab, USA, Goethe Univ. Frankfurt, Brookhaven Nat. lab, Upton, NY, USA Jagiellonian Univ. in Poland, Penza State Univ., Russia, Lastid Lab, Univ. Ibn Tofail, Morocco, Lab LN2E, Marrakech, Univ. of Aveiro, Portugal. This in addition to contributions from Jordanian universities.

### **Marwan S. Mousa**

Director of the Conference  
President of the Jordanian Club of Humboldt Fellows  
President of the Jordanian Physics Society  
Member of Trustees Council of Jadara University  
Elected Fellow of the Institute of Physics (IOP) UK  
Fellow of the Int. Field Emission Society (IFES)  
Prof. of Materials  
Dept. of Physics  
Mu'tah University  
Al-Karak, Jordan  
Tel: 00962-79-5659761  
Fax: 00 962-3-2375540  
email: marwansmousa@yahoo.com & mmousa@mutah.edu.jo

Jordan Journal of  
**PHYSICS**

An International Peer-Reviewed Research Journal

Volume 11, No. 1, April 2018, Shaban 1439 H

**4th Int. Conf. on Materials in Jordan:  
Jordanian Life Sciences for Sustainable Development (JLSSD)  
April 27 – 29<sup>th</sup> 2017  
Al al-Bayt University, Mafrq, Jordan**

**Conference Organizing Committee:**

- Prof. Dr. Dia Eddin Arafah, President of Al al-Bayt University (Chairman of the Conference).
- Prof. Dr. Marwan S. Mousa (President of the Jordanian Club of Humboldt Fellows, President of the Jordanian Physics Society, Mu'tah Univ) (Director of the Conference).
- Prof. Dr. John Banhart (Institute of Applied Materials, HZB& Prof. at Technical Univ. Berlin).
- Dr. Nelia Wanderka (Helmholtz Zentrum Berlin for Materials and Energy, Berlin, Germany).
- Prof. Dr. Yaseen Al-Soud, Dean of Sciences, AABU.

**Conference Scientific Committee:**

Prof. Dr. Marwan S. Mousa	marwansmousa@yahoo.com, mousa@mutah.edu.jo
Prof. Dr. Hussam D. Al-Hamaydeh	Husdam64@yahoo.com
Prof. Dr. Mohammad El-Khateeb	kateeb@just.edu.jo
Prof. Dr. Khalifeh Abu Saleem	k.abusaleem@jaec.gov.jo
Prof. Dr. Tareq Qirim	Qirim70@yahoo.com
Prof. Dr. Yaseen Al-Soud	alsoud@aabu.edu.jo
Prof. Dr. Talal Abu Rjai	aburjai@ju.edu.jo
Prof. Dr. Shaher Momani	s.momani@ju.edu.jo , shaherm@yaho.com
Prof. Dr. Hani Hayajneh	hani@yu.edu.jo
Prof. Dr. Hani Khoury	khouryhn@ju.edu.jo
Prof. Dr. Lauy Rashan	luayrashan@yahoo.com
Prof. Dr. Bothina Hammad	b.hamad@ju.edu.jo
Prof. Dr. Saed Dababneh	dababneh@bau.edu.jo
Prof. Dr. Yousef Hiary	hiary@ju.edu.jo
Prof. Dr. Issa Makhlof	makhlof@yahoo.com
Prof. Dr. Ibrahim Abu Aljarayseh	ijaraysh@yu.edu.jo
Prof. Dr. Rula Darwish	rulad@ju.edu.jo , rulamdarwish@yahoo.com
Prof. Dr. Riad Taha Al-Kasasbeh	rjordanjo@mail.ru
Prof. Dr. Mohammad S. Abu-Darwish	maa973@yahoo.com
Prof. Dr. Mohammed-Ali Al-Omari	alakmoh@just.edu.jo
Prof. Dr. Ali Zuhair Elkarmi	karmi@hu.edu.jo
Prof. Dr. Tayel El Hassan	tayel.elhasan@gmail.com
Prof. Ibrahim Odeh	iodeh@yu.edu.com
Prof. Dr. Ala'aldeen Al-Halhouli	a.al-halhouli@tu-bs.de
Prof. Dr. Ahmad Al Ajlouni	aajlouni@just.edu.jo
Prof. Dr. Mahdi S. Alshamasin	mahdism@hotmail.com
Prof. Dr. Mahmoud Al-Hussein	m.alhussein@ju.edu.jo

Prof. Dr. Mohammad Al Share	alshareem@mutah.edu.jo
Prof. Dr. Nathir A. Al-Rawashdeh	nathir@just.edu.jo
Prof. Dr. Borhan Aldeen A. Albiss	Baalbiss@just.edu.jo
Prof. Dr. Muhammad Ali Farajat	alfarajat@yahoo.com
Dr. Husam Al-Nasser	hnasser@aabu.edu.jo
Dr. Muath Tarawneh	muath_ph@yahoo.com
Dr. Feras Al Tarifi	faltarifi@hikma.com
Dr. Adnan Lahham	Adnan.lahham@gju.edu.jo
Dr. Feras Afaneh	feras.afaneh@gmail.com , afaneh@hu.edu.jo
Dr. Galeb Saraireh	g_saraireh@aou.edu.jo
Dr. Baker Jawabrah Al Horani	b.jawabrah@aum.edu.jo
Dr. Yahia Al-Khatatbeh	y.alkhatatbeh@psut.edu.jo
Dr. Yousif Eltous	yousifeltous@yahoo.com
Dr. Qais H.I. Safasfeh	qsafasfeh@ttu.edu.jo
Dr. Jacob H. Jacob	jjacob@aabu.edu.jo
Dr. Wael Al-Zereini	w_zereini@yahoo.com
Dr. Ehab Al-Shamaileh	ehab@ju.edu.jo
Dr. Khaled Al- Nawaysch	Khalid.na@arabpotash.com
Dr. Hmoud Dmour	hmoud79@mutah.edu.jo
Dr. Mahmoud T. Al Kalaldehy	Kaladeh82@yahoo.com
Dr. Noor Shqeirat	noorshoq@yahoo.com
Dr. Hana Hammad	hammad@ju.edu.jo
Dr. Omar Al Omari	alomari.omar@yahoo.com
Dr. Yazan Al Tell	yazztal@yahoo.com
Dr. Ali Taani	Ali82taani@gmail.com

#### **Conference Int. Scientific Committee:**

1. Prof.Dr. Erwin Neher, Nobel Prize Winner (Max- Planck-Institute Biophys. Chem, Goettingen, Germany).
2. Prof. Dr. John Banhart (Inst. of Applied Materials, HZB& Prof. at Technical Univ. Berlin).
3. Dr. Nelia Wanderka (Helmholtz Zentrum Berlin for Materials & Energy, Berlin, Germany).
4. Prof. Dr. Peter Langer (Rostock University, Rostock Germany).
5. Prof. Dr. Florin Ionescu (Konstanz Univ., Konstanz, Germany).
6. Prof. Dr. H.C. Thomas Efferth (Johannes Gutenberg Univ, Mainz, Germany).
7. Prof. Dr. Guido Schmitz (Stuttgart Univ., Stuttgart, Germany).
8. Prof. Dr. Dirk Selmar (Technical Univ., Braunschweig, Germany).
9. Dr. Mark Hagmann (Univ. of Utah, Salt Lake City, Utah, USA).
10. Dr. Ahmad Telfah (Leibnitz-Inst.fuerAnalytischeWissenschaften, Dortmund, Germany).
11. Dr. Richard Forbes (Faculty of Eng. and Sciences, Surrey Univ., UK).
12. Prof. Dr. Thomas Kelly (Cameca, Madison WI, USA).
13. Prof. Dr. Simon Ringer (Univ. of Sydney, Australia).
14. Prof. Dr. Gregory Thomson (Univ. of Alabama, USA).
15. Prof. Dr. Bernard Deconihout (Univ. of Rouen, France).
16. Prof. Dr. Majda Sekkal-Rahal (Univ. SidiBel Abbas, Algeria).
17. Prof. Dr. Mohamed Ellouze (Sfax Univ., Tunisia).
18. Prof. Dr. Abdelhadi Soudi (Rabat Univ., Morocco).
19. Prof. Dr. Hadeef Redjem (Univ. Oum El Bouaghi, Algeria).
20. Prof. Dr. Mohammed Shabat (VP, Islamic Univ, Gaza).
21. Prof. Dr. IldikoTulbure (University "1 December 1918, Alba Iulia, Romania).
22. Prof. Dr. Boguslaw Buszewski (Nicolaus Copernicus Univ., Torun, Poland).
23. Prof. Dr. Ashraf Abadi (Pharmacy Faculty Dean, German Univ. Cairo).
24. Prof. Dr. Claudio Borri (Univ. Di Firenze, Italy).



Jordan Journal of  
**P H Y S I C S**

An International Peer-Reviewed Research Journal

---

---

Volume 11, No. 1, April 2018, Shaban 1439 H

---

Table of Contents:

<b>Technical Note</b>	<b>Pages</b>
<b>Some Remarks on the Meaning of Isoelectric Point of Glycine</b> Yu.P. Pereygin, M. Jaskula and I.G. Koltshugina	1-3
<b>English Articles</b>	<b>Pages</b>
<b>Morphological Characterization of Eutectic Si and Ge Phases in the Corresponding Al-15Si and Al-20Ge Alloys Using FIB Tomography</b> N. Wanderka, H. Kropf and M. Timpel	5-15
<b>Field Electron Emission from Pyrograf III PR-1 Carbon Nanotube Fibers Embedded in Glass</b> M. S. Mousa, M.-A. H. Al-Akhras and S. I. Daradkeh	17-25
<b>Neutron-Induced Reactions in Nuclear Astrophysics</b> R. Reifarh, D. Brown, S. Dababneh, Y. A. Litvinov and S. M. Mosby	27-34
<b>Modeling the Electrical Impedance of Epoxy Polymer/Carbon Black Composite Materials</b> Z. Samir, R. Belhimria, S. Boukheir, M. E. Achour and L. C. Costa	35-43
<b>Advancing Nuclear Astrophysics Using Next-Generation Facilities and Devices</b> C. Langer, N. Klapper, C. Köppchen, S. Dababneh and R. Reifarh	45-58
<b>Characterization of Composite Electron Sources (Metal - Insulator - Vacuum)</b> A. M. Al-Qudah, S. S. Alnawasreh, M. A. Madanat, O. Trzaska, D. Matykiewicz, S. S. Alrawshdeh, M. J. Hagmann and M. S. Mousa	59-68
<b>Equations of Motion for Ideal Hydrodynamics in Rotating Frame Using Caputo's Definition</b> Emad K. Jaradat and Rabea'h A. Al-Fuqaha	69-76



### Some Remarks on the Meaning of Isoelectric Point of Glycine

Yu.P. Perelygin<sup>a</sup>, M. Jaskula<sup>b</sup> and I.G. Koltshugina<sup>a</sup>

<sup>a</sup> Penza State University, Penza, Russia.

<sup>b</sup> Jagiellonian University, Cracow, Poland.

---

Received on: 24/7/2017;

Accepted on: 8/10/2017

---

#### Introduction

One of the most important characteristics of proteins, their components aminoacids, colloids and minerals is the so-called *isoelectric point (IEP)*.

At the IEP, the values of the electric charge of protein and its conductivity are the smallest and the proteins show the smallest mobility; therefore, many of them are precipitated or transitioned from the form of sol into the form of gel. At this point, proteins have smallest viscosity and swelling ability as well as osmotic pressure. The knowledge of these properties is useful for the separation of proteins by electrophoresis or for the successful flotation of minerals.

Usually, the IEP is given as concrete pH value [1, 2], while in reality, it should be a range, sometimes very wide.

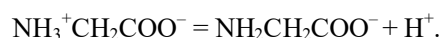
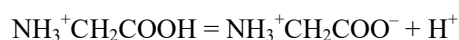
The problem will be discussed below on an example of glycine (*monoaminomonocarboxylic acid*), which is widely used in medicine [3], analytical chemistry [4, 5] and industry in the electrochemical deposition of metals and alloys [6].

#### Glycine and Ion Equilibria

The IEP value is the pH at which the solution of glycine contains only zwitterion  $\text{NH}_3^+\text{CH}_2\text{COO}^-$  and the concentrations of cationic and anionic forms are equal to zero. For glycine, the isoelectric point is reported as equal to 6.05 [7]. However, in reality, the transition of

$\text{NH}_3^+\text{CH}_2\text{COOH}$  (acidic solution) into  $\text{NH}_3^+\text{CH}_2\text{COO}^-$  and further into  $\text{NH}_2\text{CH}_2\text{COO}^-$  (basic solution) does not happen instantaneously at the strictly determined pH, but in some pH range. Therefore, the calculation of that range is interesting from both theoretical and practical points of view. In our estimations, we assumed that more than 95% of glycine present in the solution occurred in the zwitterion form.

Following equilibria exist in the solution of glycine:



The equilibrium constants are, respectively, equal to [7]:

$$K_1 = \frac{[\text{H}^+][\text{NH}_3^+\text{CH}_2\text{COO}^-]}{[\text{NH}_3^+\text{CH}_2\text{COOH}]} = 4,47 \cdot 10^{-3}$$

$$K_2 = \frac{[\text{H}^+][\text{NH}_2\text{CH}_2\text{COO}^-]}{[\text{NH}_3^+\text{CH}_2\text{COO}^-]} = 2,0 \cdot 10^{-10}$$

The solution of the two equations above together with the mass balance equation:

$$[\text{NH}_3^+\text{CH}_2\text{COO}^-] + [\text{NH}_2\text{CH}_2\text{COO}^-] + [\text{NH}_3^+\text{CH}_2\text{COOH}] = c$$

give the following expression determining the fraction of zwitterion in the solution

$$\left( \alpha = \frac{[NH_3^+CH_2COO^-]}{c} \right) \text{ (where } c \text{ is the total}$$

concentration of glycine), depending on pH

$$\alpha = \frac{[H^+]K_1}{[H^+]^2 + K_1K_2 + K_1[H^+]} \quad (1)$$

or taking into account that  $[H^+] = 10^{-pH}$

$$\alpha = \frac{10^{-pH} K_1}{10^{-2pH} + K_1K_2 + K_110^{-pH}} \quad (2)$$

As it follows from the last two equations, the relative fraction of zwitterion concentration  $NH_3^+CH_2COO^-$  in the solution as well as the relative fractions of cations  $NH_3^+CH_2COOH$  and anions  $NH_2CH_2COO^-$  do not depend on the initial concentration of glycine,  $c$ , and depend only on the pH of the electrolyte.

If  $\alpha$  is equal to unity, from the last equation one obtains the expression for the calculation of the isoelectric point value:

$$pI = -\frac{1}{2}(\lg K_1 + \lg K_2), \quad (3)$$

which coincides with the formula given in literature [7].

From Fig. 1, which shows the relative concentrations of the zwitterion, cations and anions of glycine, depending on pH of the solution, it follows that the relative fraction of glycine zwitterion  $\alpha$  is close to unity; not only at the specific pH, but also in the relatively wide pH range. In the considered case, that range spans from 4 to 8, which is in agreement with the titration curve [7, p. 61] (Fig. 2).

Introduction of a small amount of alkali into aminoacetic acid solution after the neutralization of the carboxyl group of glycine dramatically changes the pH value from 4 to 8.

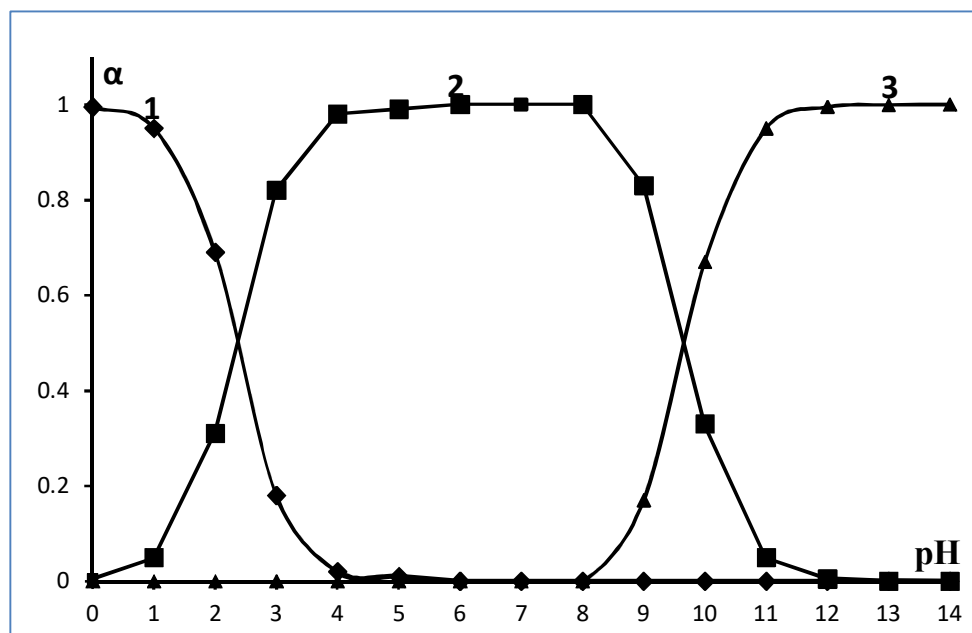


FIG. 1 The relative fractions of concentration of  $NH_3^+CH_2COOH$  (1),  $NH_3^+CH_2COO^-$  (2) and  $NH_2CH_2COO^-$  (3) in the solution of glycine at various pH values.

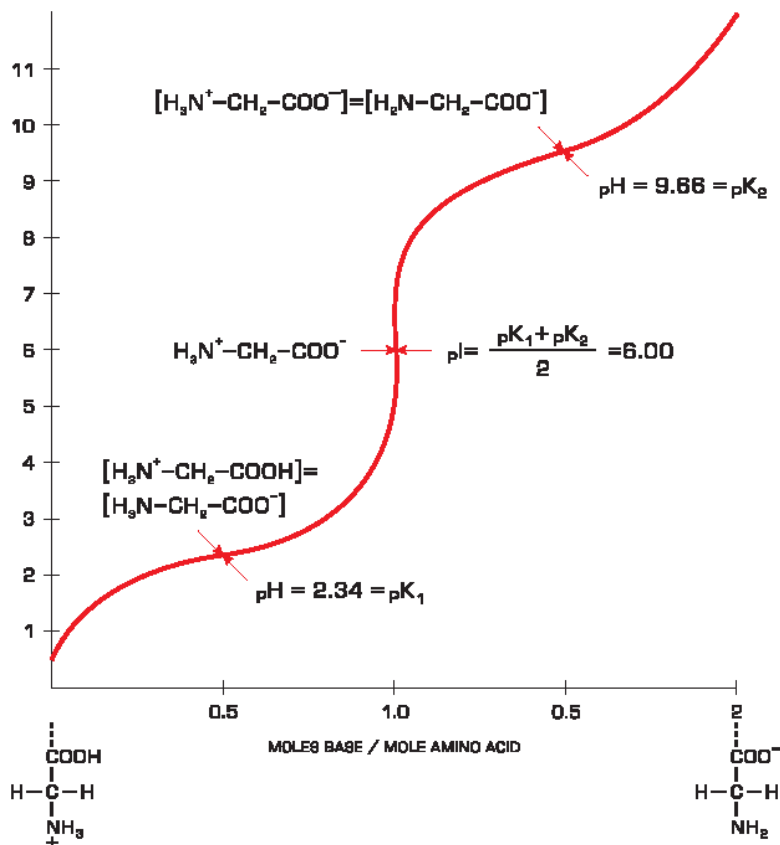


FIG. 2 The titration curve of glycine [7].

## Final Remarks

The solution of Eq. (2) for  $\alpha \geq 0.95$  results in the pH interval between 3.47 and 8.4, at which the above given relative fraction of zwitterion in solution is really observed.

Apparently, similar reasoning can be applied to other amino-acids. Thus, for the amino-acids, the characteristic value of the isoelectric point should not be given as one point only, but rather as a pH range in which zwitterion with the relative fraction near to unity exists.

## References:

- [1] Bhagavan, N.V., "Medical Biochemistry", (Harcourt Academic Press, San Diego, 2002), p.31.
- [2] McMurry, J., "Organic Chemistry with Biological Applications 2e", (Brooks/Cole Cengage Learning, 2007), p.797.
- [3] Mashkovsky, M.D., "Medicinal Products (in Russian: Lekarskie Sredstva)", (Moskva RIA Novaja Volna, 2007), 1206pp.
- [4] Kreshkov, A.P., "Fundamentals of Analytical Chemistry. Theoretical basis. Qualitative analysis (on Russian: Osnovy analytichnoj khimii. Teoreticheskie osnovy. Katshestvennyj analiz)", (Moskva, Izd. Khimia, 1965), Vol. 1, 472 pp..
- [5] Lurie, Ju.Ju., "Handbook of Analytical Chemistry (in Russian: Spravochnik po Analyticheskoi Khimii)", (Moskva, Khimia, 1971), 454 pp.
- [6] Evreinova, N.B., "Electrodeposition of iron group metals from sulfate electrolytes in the presence of aminoacetic acid. (on Russian: Elektroosazhdenije metallov grupy zheleza iz sulfatnykh elektrolitov w prisutstvii aminouksoosnoj kisloty)", Ph.D. Thesis, (St. Petersburg, 2010), p. 20.
- [7] Dawes, E.A., "Quantitative Problems in Biochemistry". (Longman: London and New York, [Russian Edition Moskva, Mir, 1983, 376pp]).



### Morphological Characterization of Eutectic Si and Ge Phases in the Corresponding Al-15Si and Al-20Ge Alloys Using FIB Tomography

N. Wanderka<sup>a</sup>, H. Kropf<sup>a</sup> and M. Timpel<sup>b</sup>

<sup>a</sup> Helmholtz Zentrum Berlin für Materialien und Energie GmbH, Hahn-Meitner Platz 1, 14109 Berlin, Germany.

<sup>b</sup> Department of Industrial Engineering, University of Trento, via Sommarive 9, 38123 Trento, Italy.

---

Received on: 25/10/2017;

Accepted on: 4/1/2018

---

**Abstract:** The three-dimensional morphology of the eutectic Ge phase in samples modified by Ca and Y in the hypoeutectic Al-20Ge alloy has been investigated by focused ion beam tomography. Addition of Ca (0.2 wt.%) caused a modification of the eutectic Ge phase from a branched plate-like morphology to a compressed cylinder-like shape of smaller dimensions. Addition of Y (0.2 wt.%) resulted in a transformation of the eutectic Ge phase with two types of morphology. One type is vermicular-like in 2D and refined plate-like in 3D, while the other appears as a holey Ge matrix with an embedded eutectic Al phase of rod-like morphology. The morphology of the modified eutectic Ge has been discussed in terms of possible growth mechanisms compared with that of the as-cast non-modified Al-20Ge alloy and that of well-known Sr-modified eutectic Si in Al-Si system.

**Keywords:** Hypoeutectic Al-Ge alloys, Modification of eutectic Ge phase, Focused ion beam tomography, Scanning electron microscopy.

## Introduction

Aluminium-silicon eutectic alloys are important industrial foundry materials. Small additions of sodium [1] or strontium produce a spectacular change of the eutectic silicon microstructure. The refinement or modification of the eutectic silicon from a uniform lamellar (plate-like) structure to fibrous structure is accompanied by a great improvement of mechanical properties, like tensile strength, elongation and hardness of the alloy. The modification effect in Al-Si alloys has been the subject of numerous studies for decades and a large number of theories was proposed to understand the modification phenomena [2-7]. With the development of a new analytical method, namely laser-assisted atom probe tomography (APT) that allows the examination of element distributions on the atomic scale, Timpel et al. [8, 9] and Barrirero et al. [10],

investigated the modification of Al-Si alloys by Sr addition. These studies showed that unlike previous beliefs, it was not the single modifying atom, i.e., Sr, but Al-Si-Sr co-segregations that are responsible for modification of the eutectic Si phase in the Al-Si system. Timpel et al. [8, 9] demonstrated that such co-segregations are absorbed at the “twin-plane re-entrant edges” (TPRE growth mechanism) on the internal eutectic Al/Si interface and prevent further growth in the current direction, thus the Si crystal changes its growth to energetically favored directions.

Modification of the eutectic Si phase from lamellar plate-like to a fine fibrous structure has also been obtained by additions of Ba, Ca and Eu [7, 11-13], even though the level of modification is different from one case to another. The strongest modifier among them has been found

to be Sr. In the past, modifiers were selected mainly in such a way that the atomic radius of the modifier only slightly differs from that of Si. Addition of modifiers like Y and Yb to the Al-7Si alloy was found to only refine the eutectic Si [11].

Comparable to the binary Al-Si eutectic alloy, Ge and Al form the similar simple eutectic binary Al-Ge system. According to their phase diagrams, the eutectic point in Al-Si is at 12.7 wt.% Si (eutectic temperature at 577 °C) and in Al-Ge at 53 wt.% Ge (at 424 °C) [14]. Both Si and Ge have a diamond crystal structure; therefore, it may be expected that the modification phenomenon is similar in both binary eutectic systems. Unlike Al-Si alloys, which have been extensively studied, the Al-Ge system has rarely been investigated [2, 15]. Hellawell [2] reported on the growth and structure of eutectics with Si and Ge based on observations mainly by optical microscopy. Li et al. [15] recently reported on the effect of trace elements Ca and Y on the eutectic Ge phase in an Al-20Ge alloy. A detailed microstructure characterization was performed on the nanometer scale using high-resolution transmission electron microscopy (HRTEM) and APT. However, a morphological characterization of the complex irregular shapes of the modified eutectic Ge phase in two dimensions (2D) using optical microscopy, scanning electron microscopy (SEM) or TEM is difficult. This information in three dimensions (3D) from the nanometer to micrometer range is missing. The nano-sectioning method using focused ion beam (FIB), which is able to produce 3D tomograms from 2D SEM images as described by Lasagni et al. [16], was successfully applied for visualization of Fe-rich phases, their location within the eutectic Al-Si grains [17,18] or of as-cast and modified structures of an Al-12Si alloy [19].

The objective of the present work is therefore the study of the morphological changes of the eutectic Ge phase by additions of Ca and Y to draw conclusions of the possible growth mechanisms based on the observations using FIB tomography. The results obtained for the Al-Ge system have been compared with those of an Al-15Si alloy modified by Sr. In addition, the microstructure has been characterized by SEM images of the sample surface.

## Experimental

Two types of alloy with nominal composition Al-20Ge and Al-15Si (composition in wt.%) were prepared using arc melting. The Al-20Ge alloy was prepared from high-purity Al and Ge (99.998% purity) at Montanuniversität Leoben, Austria. Additions of 0.2Y (wt.%) and 0.2Ca (wt.%) with purity of 99.8% (both Y and Ca) were added to the Al-20Ge alloy. The Al-15Si (wt.%) alloy was cast at the Faculty of Metallurgical and Materials Engineering of the Indian Institute of Technology Madras, Chennai, India. The alloy components were of commercial purity. More details about sample preparation and composition of Al-15Si alloy can be found in Ref. [17]. The Al-15Si alloy was modified by 62 ppm Sr. The cooling rate of the Al-20Ge alloy was ~3.3 K/sec and that of the Al-15Si alloy ~6.5 K/sec.

All samples for SEM investigations have undergone standard metallographic preparation procedures like mechanical polishing, grinding and finally polishing with a colloidal silica suspension. A Zeiss 1540 EsB CrossBeam<sup>®</sup> workstation, which combines a FIB column with a SEM column, was employed for the microstructure characterization. The imaging of the sample surface was performed with a low acceleration voltage of 2-5 kV using the InLens<sup>®</sup> secondary electron (SE) detector. The use of the low acceleration voltage allows to obtain high-resolution images [20]. The Zeiss 1540 EsB CrossBeam<sup>®</sup> workstation was also employed for 3D visualization of the eutectic Ge and the eutectic Si using FIB-energy-selective backscattered (FIB-EsB) tomography by serial sectioning and imaging as described in Refs. [17, 21]. Slices of about 25 nm (50 nm) thickness for Al-20Ge (Al-15Si) were cut out of the sample by a 30 keV Ga ion beam at an ion current of 500 pA, resulting in a constant voxel size of  $25 \times 25 \times 25 \text{ nm}^3$  ( $50 \times 50 \times 50 \text{ nm}^3$ ). The in-column EsB electron detector was used for imaging the 2D slices with an acceleration voltage of 2 kV and a grid voltage of -1.5 kV. Since the EsB detector allows the detection of elastically backscattered (high-angle) electrons with a high-resolution signal at the nanometer scale, the eutectic microstructure of the alloys was well resolved and sufficient imaging contrast was obtained. The 3D reconstruction of the investigated volumes was performed using the software VG Studio MAX 2.0.



## Results

### Microstructure of the Alloys Investigated by SEM

The microstructure of the investigated Al-20Ge, Al-20Ge-0.2Ca and Al-20Ge-0.2Y alloys is demonstrated in Figs. 1a, b and c, d, respectively. The Al-20Ge alloy (Fig. 1a) consists of primary  $\alpha$ -Al dendrites, as well as eutectic Al and Ge phases. The eutectic Ge phase imaged by SE InLens<sup>®</sup> detector can be distinguished by the light grey contrast, whereas primary  $\alpha$ -Al dendrites and eutectic Al phase are imaged in dark grey. The eutectic Ge phase

shows a branched network consisting of lamellae and corrugated crystals. The microstructure of the Al-20Ge-0.2Ca and Al-20Ge-0.2Y alloys differs from that of the Al-20Ge alloy by a finer eutectic Ge phase in the presence of Ca and Y and a clear change in the morphology of the crystals, as can be seen in Figs. 1b, c and d. Furthermore, apart from the  $\alpha$ -Al dendrites and the eutectic Al and Ge phases that form in the binary system, intermetallic phases with lengths of several tens of  $\mu\text{m}$  were also found. The intermetallic phases are well discernable because of their rod- or needle-like morphology in 2D. In the corresponding alloys, they are of  $\text{Al}_2\text{Ge}_2\text{Ca}$  (not shown here) and  $\text{Al}_2\text{Ge}_2\text{Y}$  type.

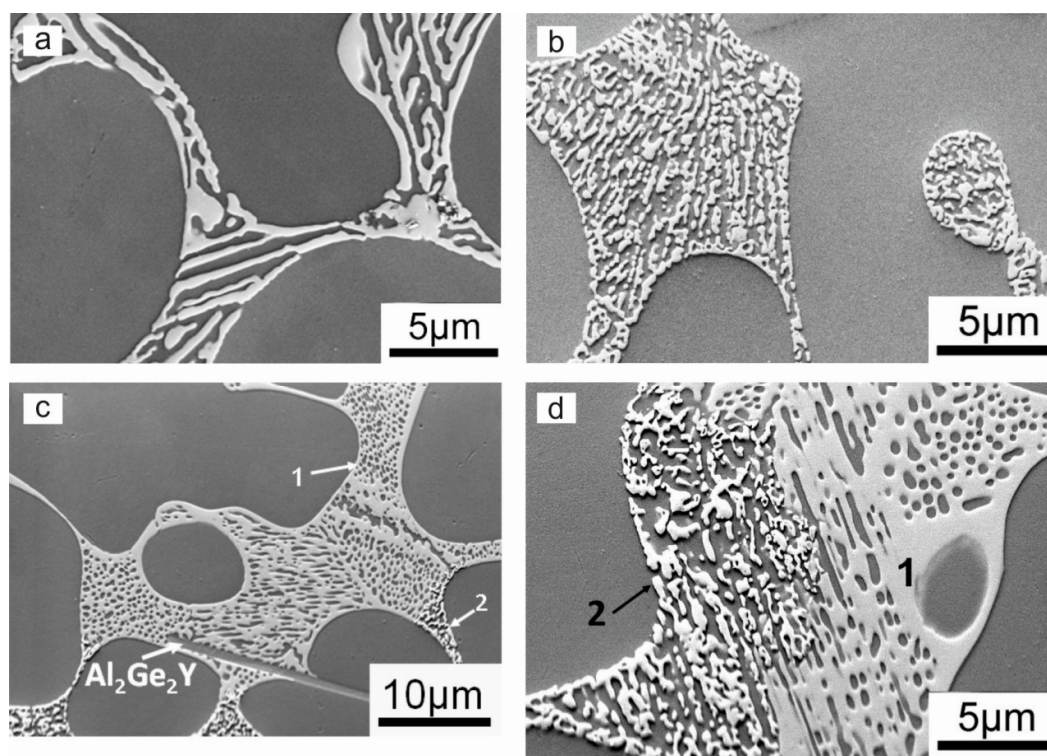


FIG. 1. Microstructure of a) Al-20Ge, b) Al-20Ge-0.2Ca and c) Al-20Ge-0.2Y alloys visualized by the InLens<sup>®</sup> SE detector; d) enlarged view of the eutectic microstructure of the Al-20Ge-0.2Y alloy.

The morphology of the eutectic Ge phase in Figs. 1b and c, d (region marked by 2 in Figs. 1c and d) is similar. However, Ca additions produced a quite uniform eutectic Ge phase (Fig. 1b) regarding size and morphology, while in the alloy with Y additions (Figs. 1c and d), there are two regions (marked by 1 and 2) with different structures. Region 1 indicates a holey Ge matrix with an embedded eutectic Al phase of rod-like morphology, while the structure of the region 2 appears as small eutectic Ge precipitates of irregular shape. The eutectic Ge phase in region

1 is slightly darker in contrast than in region 2. The eutectic Al phase inside region 1 looks like small rods with diameters ranging from 0.25 to 0.38  $\mu\text{m}$  and their length axis lies between 1.26 and 5.85  $\mu\text{m}$ . A typical intermetallic  $\text{Al}_2\text{Ge}_2\text{Y}$  phase with rod-like morphology is shown in Fig. 1c.

The typical microstructure of the unmodified and the Sr-modified Al-15Si alloy is illustrated in Fig. 2a, b and 2c, d, respectively. It is noteworthy that for the comparison of their

microstructure (i.e., compare Fig. 2a, c and 2 b, d, respectively) the magnification of the SEM images has been adapted to the size of the corresponding microstructure. The eutectic Si phase (bright contrast) exhibits coarse plates in the unmodified alloy (Fig. 2a, b), while in the Sr-

modified alloy (Fig. 2c, d) it appears as a much finer and mixed structure of thin Si platelets and fibrous Si. The difference in the magnification emphasizes the modification effect (i.e., higher magnification needed for the Sr-modified Al-Si microstructure).

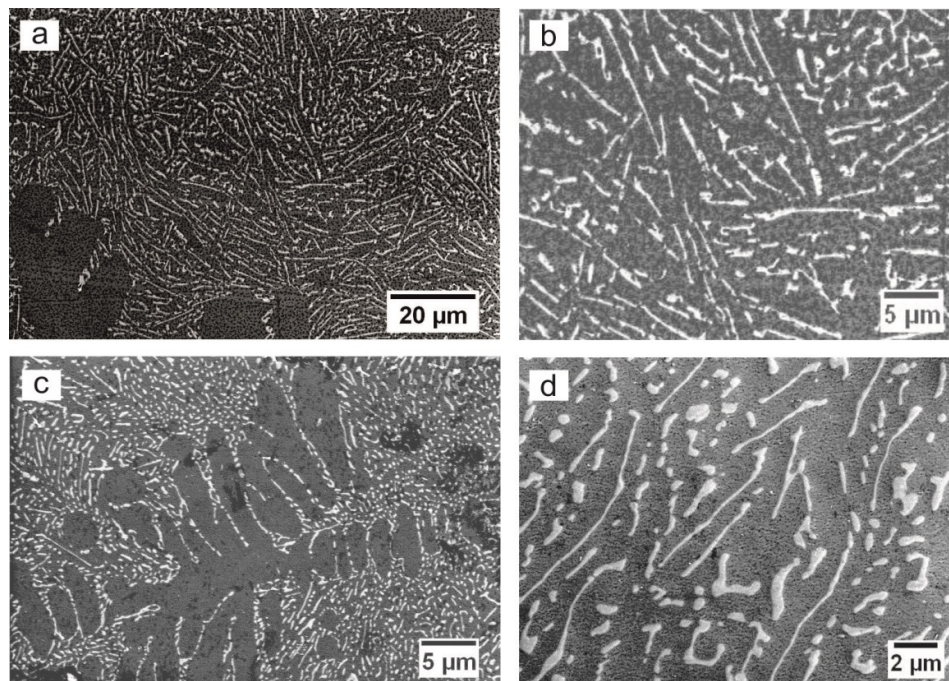


FIG. 2. Microstructure of a,b) unmodified and c,d) Sr-modified Al-Si alloy visualized by the InLens<sup>®</sup> SE detector. Note the difference in the magnification of the SEM images.

## FIB Tomography

### *Al-20Ge-based Alloys*

Figs. 3, 4 and 5 show the Al-Ge eutectic microstructure of the Al-20Ge, Al-20Ge-0.2Y and Al-20Ge-0.2Ca alloys in 3D by means of FIB-EsB tomography. In the unmodified Al-20Ge alloy, the eutectic Ge (in cyan) and eutectic Al phase (in blue) are illustrated in Fig. 3a within an analyzed volume of  $11 \times 6 \times 4 \mu\text{m}^3$ . The primary  $\alpha$ -Al phase is marked by A. A separate visualization of the 3D morphology of the eutectic Ge phase is shown in Fig. 3b. It should be noted that the dimension in  $z$  direction is reduced from 4 to  $1.56 \mu\text{m}$  in order to better visualize the real size and shape of the eutectic Ge phase. The lamella-like eutectic Ge phase in 2D observed by SEM (Fig. 1a) consists of plates in 3D as can be seen after the FIB tomography shown in Fig. 3b. The 3D image clearly indicates that the eutectic Ge phase grows in a branched manner, thus forming an interconnected Ge

network. The average thickness of the coarse branched Ge plates in the  $xy$ -imaging plane was measured to be  $0.84 \mu\text{m}$  and the length axis can reach sizes larger than  $10 \mu\text{m}$ .

Fig. 4a shows the 3D microstructure of Al-20Ge-0.2Ca alloy in an analyzed volume of  $11 \times 6 \times 4.7 \mu\text{m}^3$ . For the sake of clarity, only a part ( $11 \times 0.6 \times 3.8 \mu\text{m}^3$ ) of the entire volume is shown in Fig. 4b and a magnified part is illustrated in Fig. 4c. As can be seen from Fig. 4b and c, the eutectic Ge phase is much finer than in the unmodified alloy. Its morphology appears as compressed cylinder-like structures that have an elliptical cross-section. The average width of the ellipses is  $\sim 0.35 \mu\text{m}$  and their length is about  $1.65 \mu\text{m}$ . The height of the compressed cylinders is difficult to measure, but it is roughly bigger than the length of the cylinder axis truncated by the analyzed volume. The compressed cylinders are often connected with each other, forming a network.

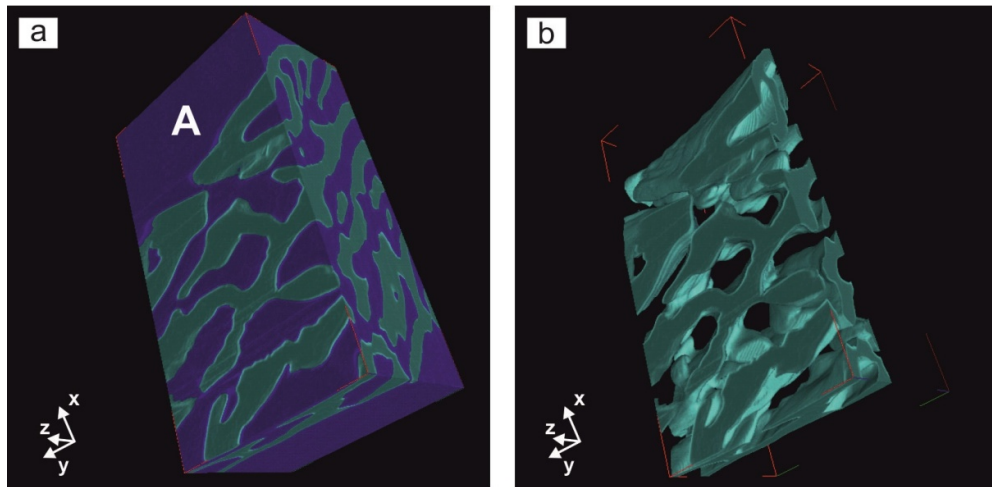


FIG. 3. a) 3D morphology of the eutectic Ge phase (cyan) embedded in the eutectic Al phase (blue) in an investigated volume of  $11 \times 6 \times 4 \mu\text{m}^3$  of unmodified Al-20Ge alloy; primary  $\alpha$ -Al phase is marked by A; b) the eutectic Ge phase is presented in a reduced volume of  $11 \times 6 \times 1.56 \mu\text{m}^3$ .

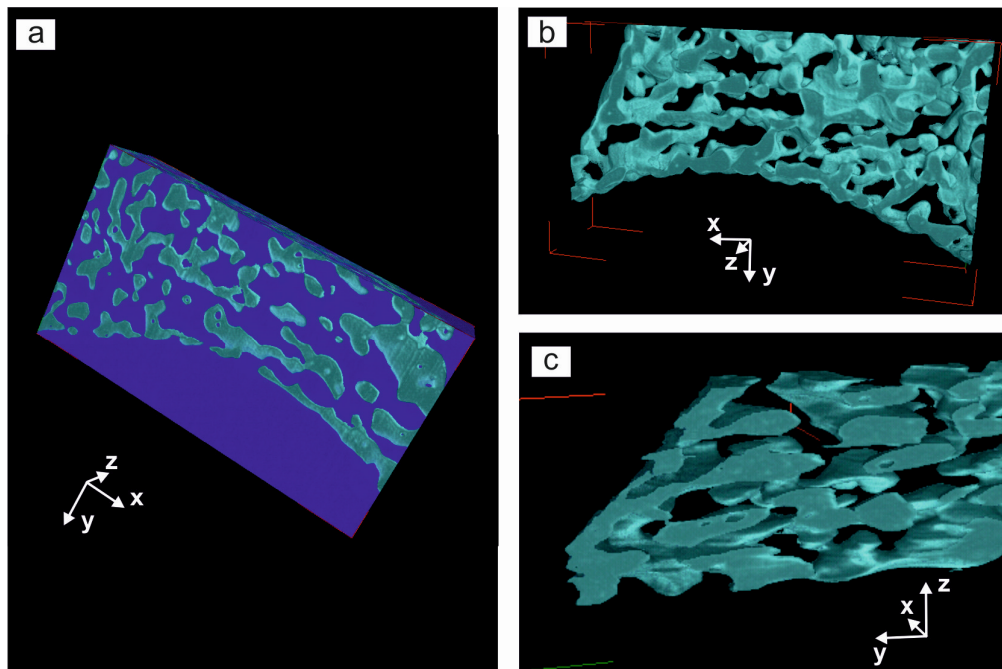


FIG. 4. a) 3D morphology of the eutectic Ge phase (cyan) embedded in the eutectic Al phase (blue) in an investigated volume of  $11 \times 6 \times 4.7 \mu\text{m}^3$  of the Al-20Ge-0.2Ca alloy; b) the eutectic Ge phase is presented in a reduced volume of  $11 \times 0.6 \times 3.8 \mu\text{m}^3$ ; c) enlarged view of a part of the eutectic Ge phase with compressed cylinder-like morphology shown in b).

For the Al-20Ge-0.2Y alloy, Fig. 5a demonstrates the 3D microstructure in an investigated volume of  $11 \times 6 \times 4 \mu\text{m}^3$ . The microstructure consists of the eutectic Ge and Al phases and primary  $\alpha$ -Al phase which is marked by A. Two different morphologies of the eutectic Ge phase were observed, marked by 1 and 2, which is in agreement with the SEM

observations of the sample surface (Fig. 1c and d). These two different morphologies of the eutectic Ge phase can be more clearly seen from the thin volume section (thickness  $\sim 0.16 \mu\text{m}$ ), as shown separately in Fig. 5b and c for the eutectic Ge and Al phase, respectively. The eutectic Ge phase in region 1 has a higher volume fraction than that in region 2. The 3D morphology of the

eutectic Ge phase in region 1 does not appear as plates, but as a holey eutectic Ge matrix (Fig. 5b, see higher magnification in Fig. 5c), in which the eutectic Al phase with a rod-like morphology (Fig. 5d, region 1) is embedded. The diameter of the rod-like eutectic Al phase as measured from 3D images is about  $0.4 \pm 0.05 \mu\text{m}$  (where the error corresponds to the  $2\sigma$  deviation). The value

lies in the range of the typical diameter measured from the SEM image in Fig. 1c (i.e.,  $0.25\text{--}0.38 \mu\text{m}$ ). In contrast, the eutectic Ge phase in region 2 exhibits a complex structure with highly curved surfaces and a vermicular-like shape as can be seen in the thin slice of the investigated volume. The diameter of the vermicular-shaped eutectic Ge phase is about  $0.2 \mu\text{m}$ .

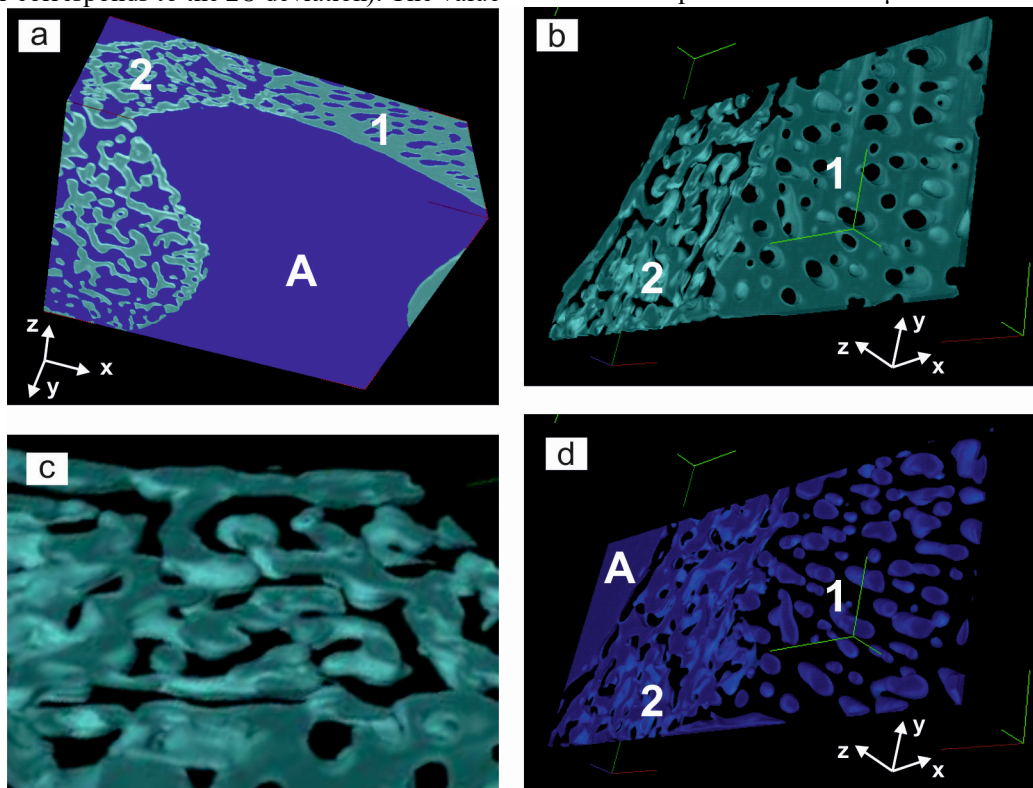


FIG. 5. 3D morphology of the eutectic Ge phase (cyan) embedded in the eutectic Al phase (blue) in an investigated volume of  $11 \times 6 \times 4 \mu\text{m}^3$  of the Al-20Ge-0.2Y alloy: a) two regions with different morphologies of the eutectic Ge phase are marked by 1 and 2; primary  $\alpha$ -Al is marked by A; b) eutectic Ge; c) higher magnification of region 2 and d) eutectic Al phases are presented in a reduced volume of  $11 \times 6 \times 0.16 \mu\text{m}^3$ .

#### Al-15Si-based Alloys

Fig. 6 displays the morphology of the 3D eutectic Al-Si microstructure of the unmodified (Fig. 6a,b) and Sr-modified (Fig. 6c,d) Al-15Si alloy. The unmodified Si phase with plate-like morphology is illustrated in Fig. 6b and the Sr-modified Si phase is shown in Fig. 6c. The eutectic Si plates are very thin with a thickness between  $0.2 \mu\text{m}$  and  $0.5 \mu\text{m}$ . They are truncated by the surface of the analyzed volume and therefore, their total length could be much larger

than visualized by the data set. The Sr-modified eutectic Si phase shows a partially modified structure (Fig. 6d), which is in agreement with the corresponding SEM images of the sample surface (Fig. 2c and d) and previous observations of the alloy using FIB-EsB tomography [17]. The diameter of the eutectic Si fibers is in the range between  $0.3 \mu\text{m}$  and  $0.7 \mu\text{m}$ , whereas the thin Si platelets are much smaller and thinner than the Si plates in the unmodified Al-15Si alloy.

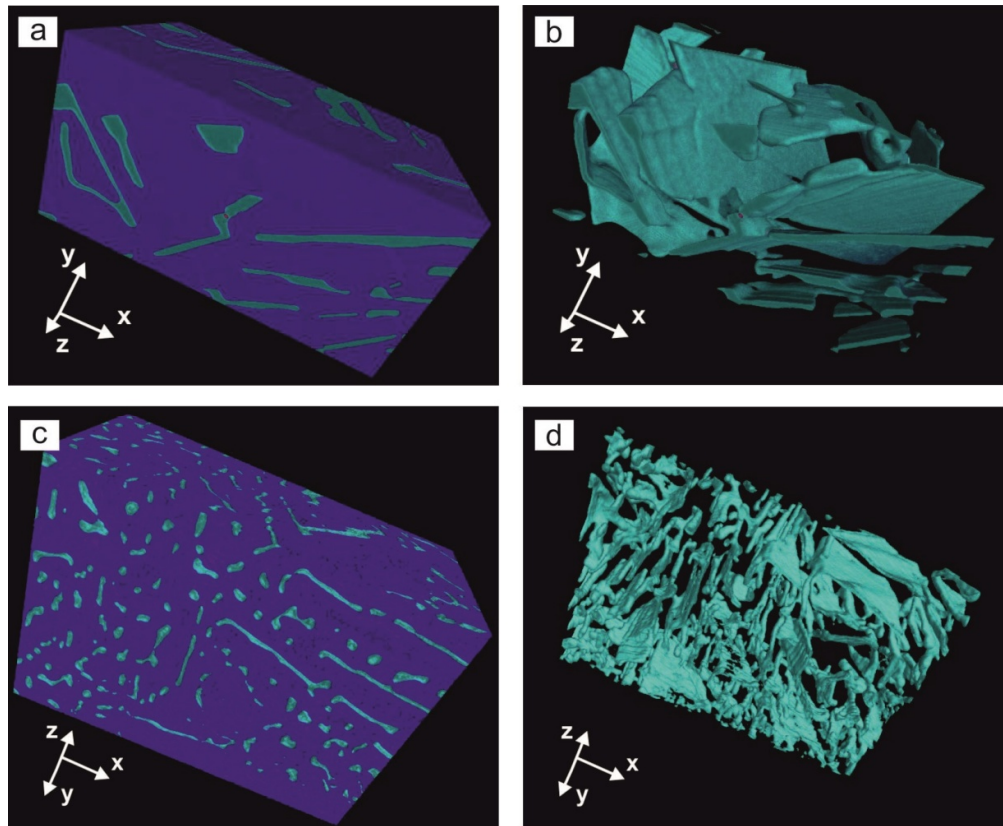


FIG. 6. a) 3D morphology of the eutectic Si phase (cyan) embedded in the eutectic Al phase (blue) in an investigated volume of  $20 \times 10 \times 13 \mu\text{m}^3$  of the unmodified Al-15Si alloy; b) unmodified eutectic Si phase only; c) 3D morphology of the eutectic Si phase (cyan) embedded in the eutectic Al phase (blue) in an investigated volume of  $27 \times 19 \times 12 \mu\text{m}^3$  of the Sr-modified Al-15Si alloy; d) Sr-modified eutectic Si phase only.

## Discussion

### Unmodified Al-Si and Al-Ge Alloys

Both the Al-Si- and the Al-Ge-based alloys mainly comprise the irregular binary eutectic microstructure, which is the type of eutectic that can be typically found in metal/non-metal systems. The eutectic Al phase is non-faceted, while the eutectic Si-/Ge- phase is faceted. In such systems, the eutectic develops an irregular structure, as the growth of the Si and Ge crystals is strongly anisotropic along the close-packed  $\{111\}$  planes of the diamond cubic structure, resembling large plates as can be seen from the FIB tomography shown in Figs. 3a, b and 6a, b. The plate-like phases have a significant kinetic barrier to grow in certain directions as is the case in particular for the eutectic Si phase. Branching of Si and Ge crystals or termination of growth occurs, i.e., no constant lamellar spacing exists during growth of irregular eutectics. According

to Fisher and Kurz [22], the faceted Si and Ge plates lead ahead of the eutectic Al matrix, since they have the smallest constitutional undercooling, and the non-faceted eutectic Al phase follows. In contrast to the regular eutectic, where the two phases grow with a similar growth rate, the irregular eutectic Al and Si/Ge phases grow with different growth rates. However, coupled growth is always maintained. As soon as the eutectic Si/Ge phase begins to grow, Al is rejected at the solidification front and *vice versa*, Si or Ge atoms are rejected on the solidification front of the eutectic Al phase. This alternating sequence of solute rejection leads to a non-isothermal growth interface, which locally provides conditions for simultaneous growth of both eutectic phases. This growth mechanism has also been observed during *in-situ* solidification of an Al-10Si-0.3Fe alloy during X-ray synchrotron tomography experiments [23].

However, besides the similarities of the two systems, there are also differences in the microstructure as seen in Figs. 3a, b and 6a, b. The unmodified Al-Ge alloy exhibits a much larger volume fraction of eutectic Ge (36.5 vol.% [2]) compared to the eutectic Si (13.6 vol.% [17]) phase in the unmodified Al-Si alloy. Consequently, the eutectic Ge plates are much coarser than the eutectic Si plates when comparing the width of the plates seen in Fig. 3a and 6a, respectively. The overall morphology and formation of the 3D network of the eutectic Ge and Si plates (compare Figs. 3b and 6b) are also different. The cause lies in the different growth mechanism of Si and Ge. The eutectic Si crystal grows mainly as individual faceted plates with {100} faces. The eutectic Ge crystal, besides faceted crystals, shows also corrugated crystals with alternating {111} faces. The formation of corrugated crystals can be explained by the fact that Ge forms growth twins much easier and there is no preferential growth texture in <100> direction as in Si. Otherwise, Hellawell [2] argued the complex regular growth forms of the eutectic Ge phase as a consequence of the more symmetrical form of the Al-Ge phase diagram [14].

### **Modification by Sr, Ca and Y**

#### *Al-15Si Alloy Modified by Sr*

The phenomenon of modification of the eutectic Si phase by Na [1], Sr [7-10, 24, 25], Ba, Ca, Y and Yb [11] has been widely studied. Many mechanisms of growth and nucleation of the eutectic Si phase were proposed for modification, but only a few mechanisms were established and are commonly accepted, such as "poisoning of TPRES" [4, 26] and "impurity-induced twinning" (IIT) [7]. According to Nogita et al. [11], among Ba, Ca, Y and Yb, the best modification of the eutectic Si phase has been obtained by addition of Ba. Addition of Ca produced also a very fine Si fibrous structure. Y and Yb only refined the eutectic Si phase, but it remains plate-like. It is noteworthy that the twin density in the eutectic Si phase was found to be similar for all the modified samples, even though Ba and Ca showed strong modification, whereas Y and Yb only refined the eutectic Si phase. The conclusion is that the IIT mechanism does not strongly influence the change of the eutectic Si growth direction. In fact, the recently gained knowledge at the atomic scale using APT [8, 9] evidences is that within the eutectic Si phase (in

an Al-10Si-based commercial alloy), nanometer sized rod-like Si-Al-Sr co-segregations, which form at the solidification front, restrict the growth direction. The plate-shaped branched networks shown in Fig. 6a, b finally change into a branched coral network of fibers (Fig. 6c, d) by adding the modifying element Sr. In the Sr-modified Al-15Si alloy, a mixed morphology (i.e., thin platelets and fibrous structure) of the eutectic Si phase is visible (Fig. 6c, d). The lower Sr content (62 ppm) in this alloy results in an only partially modified morphology of the eutectic Si phase during eutectic solidification, whereas a well-modified structure of the eutectic Si phase can be achieved at Sr levels in the range of 80 - 120 ppm (depending on the alloy purity and cooling rate) [25].

#### *Al-20Ge Modified by Ca*

The sufficient amount of the eutectic modifiers Ca and Y to produce a significant change in the morphology of the eutectic Ge phase has not been determined so far, but the effect of Ca and Y on an Al-7Si-based (A356.0) alloy has been investigated by Nogita et al. [11]. The maximum modification of the eutectic Si phase (transition from flakes to fibers) was achieved by 210 ppm Ca, while Y additions in the range between 700 and 5200 ppm cause only a refinement of the Si plates. The present results for the Al-Ge system reveal a refined eutectic Ge phase by additions of both Ca and Y. However, a large excess of Ca and Y (0.2 wt.% in the present study) produces also  $\mu\text{m}$ -sized intermetallic compounds of the type  $\text{Al}_2\text{Ge}_2\text{Ca}$  (not shown here, but they are present in the alloy with Ca additions) and  $\text{Al}_2\text{Ge}_2\text{Y}$ , which are typical characteristics of an over-modified alloy. This result is in agreement with observations by Hellawell [2]. Ludwig et al. [12] reported that  $\text{Al}_2\text{Si}_2\text{Ca}$  intermetallic phases occur already at 39 ppm (300 ppm) Ca addition to an Al-7Si commercial purity (high-purity) alloy. An increased level of Sr (500 ppm) to an Al-7Si alloy produced also large Sr-containing intermetallic phases. However, Dahle et al. [25] suggested that in addition to the formation of Sr-containing intermetallic phases, the high amount of Sr was rather correlated with the reversion of eutectic nucleation. It appears that the formation of intermetallic compounds depends on many factors, such as modifier type and content, metalloid type and the purity of the alloy.

In the Al-Ge alloy with Ca addition, the size and morphology of the eutectic Ge phase change from coarse branched Ge plates (unmodified alloy) to compressed cylinder-like morphology of smaller dimensions, being connected and building a network. The formation of the network can be explained based on the impingement of individual Ge particles during their growth. According to their morphology, the growth of individual Ge particles occurs in two preferential directions (one is the main axis of the compressed cylinder and the other one is the longer axis of the elliptical cross-section). The crystals of the modified eutectic Ge phase are coarser but shorter than the crystals of the modified eutectic Si phase. In contrast, Ca produces Si fibers in Al-Si alloys [11] with only one preferential growth direction, i.e., along the fibers. As mentioned above, studies on the Al-Ge system are rather rare [2, 15], but there is a significant amount of research on the Al-Si system. However, since Si and Ge crystals exhibit the same diamond structure, we assume that their behavior with respect to modification is similar. In the Al-Si system, the addition of the modifier usually causes a decrease of the eutectic temperature and a shift of the eutectic point to higher Si concentrations. An increase in the recalescence undercooling and a decrease of the eutectic temperature by Sr addition to an Al-10Si alloy have also been reported by McDonald et al. [24]. Ludwig et al. [12] showed that 50 ppm Ca addition to Al-7Si (A356 commercial purity alloy) refined the eutectic Si phase, but coarsened it in the high-purity alloy [12], whereas Ca additions higher than 300 ppm do not change the morphology of the eutectic Si phase [12]. Ludwig et al. [12] suggested that Ca suppresses the nucleation and growth and thereby alters the morphology of the eutectic Si phase. The morphology transition of the eutectic Ge phase in the present work could be then explained by the larger kinetic undercooling with Ca addition. The growth rate of the modified eutectic Ge phase should be lower than that of the unmodified one, indicating that the overgrowth by the eutectic Al matrix occurs more frequently and the crystal shape will become more complex. The density of twins in both the unmodified and the Ca-modified eutectic Ge phase has been observed to be very low [15], which indicates that the IIT mechanism plays no significant role in the modification of the eutectic Ge phase. Although the number of

twins greatly increases in Sr-modified Al-Si alloys, Timpel et al. [8, 9] and Barrirero et al. [10] came to the same conclusion that the IIT mechanism does not significantly affect the growth direction of the eutectic Si phase. As mentioned above, the rod-like Al-Si-Sr co-segregations restrict the growth direction of the eutectic Si phase. In the case of the eutectic Ge phase in the Al-20Ge system, Li et al. [15] reported on the presence of rod-like Al-Ge-Ca co-segregations with a diameter of  $\sim 3$  nm and a length of  $\sim 58$  nm as measured by APT. Their total length could be longer, because they were truncated on one side of the surface of the analyzed APT volume. They contain Al ( $32.02 \pm 2.78$ ) at.%, Ge ( $58.28 \pm 2.18$ ) at.%, Ca ( $5.98 \pm 3.27$ ) at.% and O ( $3.72 \pm 3.13$ ) at.%. We assume that such types of co-precipitates induced the morphological change of the Ge crystals similar to that of Si in Al-Si alloys [8-10]. However, more detailed investigations are required to clarify whether the high amount of Ca (2000 ppm) as modifier or the Ge itself is responsible for the formation of the compressed cylinder-like morphology instead of fibers.

#### *Al-20Ge Refined by Y*

As shown in Figs. 1c, d and Fig. 5, the microstructure of Al-20Ge with Y addition differs from that with Ca addition. Moreover, there are two regions (1 and 2) in the eutectic Ge phase, which clearly depict different morphologies. It should be mentioned that the volume fraction of Ge in region 1 is much larger than that in region 2 (see Fig. 1c). The holey eutectic Ge phase (Fig. 5b) of region 1 contains a rod-like eutectic Al phase (Fig. 5d). The colonies of the eutectic Al rods are all oriented more or less in the same direction within a single eutectic Ge grain. The explanation for the obtained microstructure in region 1 can be as follows: the eutectic reaction starts with the formation of the Ge crystals nucleating at the Al dendrites and Ge builds a continuous phase front around Al dendrites. Ge grows forward and the Al solute is rejected at the solid-liquid front, leading to the formation of Al clusters. Such clusters segregate and grow to rod-like structures. During further solidification, the Ge crystals tend to overgrow the eutectic Al rods due to their higher growth rate. This growth process is continuously repeated and at the end of solidification, it creates the microstructure of region 1 presented in Figs. 1c, d and 5b. Regarding the orientation

of the eutectic Al rods within a eutectic Ge grain, it can be concluded that the eutectic Al rods strongly depend on the orientation of the eutectic Ge phase and grow epitaxially on a  $\{111\}$  plane in the  $\langle 110 \rangle$  direction. Columnar eutectic Al phase with a strong texture in  $\langle 110 \rangle$  direction has also been observed in a Sr-modified Al-Si alloy [6]. The composition of these eutectic Al rods could not be measured yet. However, APT measurements [15] showed much smaller Y-enriched particles embedded in the eutectic Ge phase. The composition of the Y particles was measured to be  $\text{Al}_{69}\text{Ge}_9\text{Y}_{22}$ , which is close to the stable equilibrium phase  $\text{Al}_3\text{Y}$ , assuming that Al is partially substituted by Ge. Li et al. [15] reported on another type of particles containing Y with the composition  $\text{Al}_{42}\text{Ge}_{49}\text{Y}_5\text{O}_4$ . This composition, however, does not correspond to the stable  $\text{Al}_2\text{Ge}_2\text{Y}$  intermetallic phase that was observed by SEM (see Fig. 1c). A tendency to form nanometer sized Al-rich (14 at.% Al) clusters within the eutectic Ge phase of the as-cast Al-Ge alloy has been already reported by Li et al. [15]. Although the maximum solubility of Al in Ge according to the binary Al-Ge phase diagram is less than 2 at. % at  $400^\circ\text{C}$  [14], the eutectic Ge phase in the as-cast alloy showed a significantly high concentration of Al (5.4 at.%) [15].

Region 2 shows an irregularly shaped eutectic Ge phase. At the first glance, the morphology of the Y-modified eutectic Ge phase looks similar to that modified with Ca. However, a closer inspection of the FIB tomograms reveals that region 2 looks like a miniature of the unmodified eutectic Ge phase illustrated in Fig. 3b. Indeed, the thickness (0.2  $\mu\text{m}$ ) of the eutectic Ge phase with Y additions is four times smaller than that of the unmodified alloy (0.84  $\mu\text{m}$ ), but the morphology is still the same. The microstructure of region 2 indicates a significant decrease in the size of the eutectic Ge phase, i.e., a refinement. Our observations are in good agreement with the results presented by Nogita et al. [11], where only plate-like refinement by Y in an Al-7Si alloy has been found. Refinement of the eutectic Si phase is known to be obtained in high-purity hypoeutectic Al-Si alloys without Sr additions [24, 27] when compared to that of commercial purity alloys.

Our conclusion concerning the role of Y addition to an Al-20Ge alloy is that it creates a constitutionally undercooled zone thus

increasing the number of nuclei, which refines the microstructure.

## Summary

Morphological changes of the eutectic Ge phase by addition of the modifiers Ca and Y to an Al-20Ge alloy and of the eutectic Si phase by addition of the modifier Sr to an Al-15Si alloy have been investigated using FIB tomography. There are a number of similar, but also different, features in the two eutectic binary alloys:

- Both alloys in the unmodified state show a plate-like morphology of the eutectic Si/Ge phases. The eutectic Si grows as individual (but interconnected) plates and the eutectic Ge as a highly branched network of coarse plates. This is a result of the preferential growth in one direction of the eutectic Si phase, whereas the eutectic Ge phase can grow without any preferential direction. The eutectic Si plates are much thinner than the eutectic Ge plates, which is due to the higher volume fraction of the eutectic Ge phase in Al-Ge-based alloys.
- The addition of Sr and Ca modifies the eutectic Si and Ge phase, respectively. However, the addition of Sr changes the morphology of the eutectic Si phase from plate-like to fine fibers, whereas the addition of Ca changes the morphology of the eutectic Ge phase from branched plates to compressed cylinder-like shapes. The difference in the morphologies of the two modified eutectic microstructures can be ascribed to the different growth behaviors of the Si and Ge crystals.
- Addition of Y to the Al-20Ge alloy only results in a refinement of the eutectic Ge phase. Two types of refinement region can be obtained. The morphology of the eutectic Ge phase in one region is similar to that of the unmodified alloy, but four times smaller. The eutectic Ge phase in the second region represents a holey eutectic Ge phase with an embedded rod-like eutectic Al matrix.

## Acknowledgments

The authors would like to thank Prof. J.H. Li, Montanuniversität Leoben, Austria, as well as Prof. B.S. Murty, Indian Institute of Technology Madras, Chennai, India, for providing the alloy samples.



## References

- [1] Pacz, A., Alloy, U.S. Patent No. 1387900 (1921).
- [2] Hellowell, A., *Prog. Mater. Sci.*, 15 (1970) 3.
- [3] Hanna, M.D., Lu, S.-Z. and Hellowell, A., *Metall. Trans. A.*, 15 (1984) 459.
- [4] Kobayashi, K.F. and Hogan, L.M., *J. Mater. Sci.*, 20 (1985) 1961.
- [5] Shamsuzzoha, M. and Hogan, L.M., *J. Cryst. Growth*, 76 (1986) 429.
- [6] Shamsuzzoha, M. and Hogan, L.M., *Philos. Mag. A*, 54 (1986) 459.
- [7] Lu S.Z. and Hellowell, A., *Metal. Mater. Trans. A*, 18 (1987) 1721.
- [8] Timpel, M., Wanderka, N., Schlesiger, R., Yamamoto, T., Lazarev, N., Isheim, D., Schmitz, G., Matsumura, S. and Banhart, J., *Acta Mater.*, 60 (2012) 3920.
- [9] Timpel, M., Wanderka, N., Schlesiger, R., Yamamoto, T., Isheim, D., Schmitz, G., Matsumura, S. and Banhart, J., *Ultramicroscopy*, 132 (2013) 216.
- [10] Barrirero, J., Engstler, M., Ghafoor, N., de Jonge, N., Odén, M. and Mücklich, F., *J. Alloys Compd.*, 611 (2014) 410.
- [11] Nogita, K., Drennan, J. and Dahle, A.K., *Mater. Trans.*, 44 (2003) 625.
- [12] Ludwig, T.H., Schaffer, P. and Arnberg, L., *Metal. Mater. Trans. A*, 44 (2013) 3783.
- [13] Li, J., Hage, F., Wiessner, M., Romaner, L., Scheiber, D., Sartory, B., Ramasse, Q. and Schumacher, P., *Sci. Rep.*, 5 (2015) 13802.
- [14] Hansen, M. and Anderko, K., "Constitution of binary alloys", (McGraw-Hill Publ. Co., Inc., New York/Toronto/London, 1958).
- [15] Li, J.H., Wanderka, N., Balogh, Z., Stender, P., Kropf, H., Albu, M., Tsunekawa, Y., Hofer, F., Schmitz, G. and Schumacher, P., *Acta Mater.*, 111 (2016) 85.
- [16] Lasagni, F., Lasagni, A., Holzapfel, C., Mücklich, F. and Degischer, H.P., *Adv. Eng. Mater.*, 8 (2006) 719.
- [17] Timpel, M., Wanderka, N., Murty, B.S. and Banhart, J., *Acta Mater.*, 58 (2010) 6600.
- [18] Timpel, M., Wanderka, N., Grothausmann, R. and Banhart, J., *J. Alloys Compd.*, 558 (2013) 18.
- [19] Lasagni, F., Lasagni, A., Marks, E., Holzapfel, C., Mücklich, F. and Degischer, H.P., *Acta Mater.*, 55 (2007) 3875.
- [20] Reimer, L., "Scanning electron microscopy: physics of image formation and microanalysis", (Springer, Berlin, 1998).
- [21] Uchic, M.D., Holzer, L., Inkson, B.J., Principe, E.L. and Munroe, P., *MRS Bulletin* 32 (2007) 408.
- [22] Fisher, D.J. and Kurz, W., *Acta Metall.*, 28 (1980) 777.
- [23] Yu, J.M., Wanderka, N., Rack, A., Daudin, R., Boller, E., Markötter, H., Manzoni, A., Vogel, F., Arlt, T., Manke, I. and Banhart, J., *Acta Mater.*, 129 (2017) 194.
- [24] McDonald, S.D., Nogita, K. and Dahle, A.K., *Acta Mater.*, 52 (2004) 4273.
- [25] Dahle, A.K., Nogita, K., Zindel, J.W., McDonald, S.D. and Hogan, L.M., *Metal. Mater. Trans. A*, 32 (2001) 949.
- [26] Day, M.G. and Hellowell, A., *Proc. Roy. Soc. A*, 305 (1968) 473.
- [27] Yu, J.M. Wanderka, N., Mische, G. and Banhart, J., *Intermetallics*, 72 (2016) 53.



### Field Electron Emission from Pyrograf III PR-1 Carbon Nanotube Fibers Embedded in Glass

M. S. Mousa<sup>a</sup>, M.-A. H. Al-Akhras<sup>b</sup> and S. I. Daradkeh<sup>a</sup>

<sup>a</sup> Department of Physics, Mutah University, Al-Karak 61710, Jordan.

<sup>b</sup> Department of Physics, Jordan University of Science and Technology, Irbid, Jordan.

---

Received on: 24/7/2017;

Accepted on: 17/1/2018

---

**Abstract:** This study investigates the field electron emission properties of Pyrograf-III carbon nanotube fibers (CNTFs). Field emitters were manufactured by employing a drawing technique using a glass puller. A field electron microscope with a tip (cathode) to screen (anode) separation of approximately 10 mm was used to characterize the emitters. The current-voltage ( $I$ - $V$ ) characteristics of the CNTFs showed a shallow increase in the emitted current with increasing applied voltage, until a threshold voltage ( $V_{TH}$ ) is reached, after which a “switch-on” phenomenon occurs. The  $I$ - $V$  characteristics are then linear. Fowler-Nordheim plots and field electron emission patterns are also discussed and it is shown that it is possible to get a single bright emission spot.

**Keywords:** Field electron emission, Carbon nanotube fibers (CNTFs).

## Introduction

Field electron emission (FE) involves electron emission from surfaces that is caused by high electric fields. It has been extensively studied since the late 1920s, after Fowler and Nordheim (FN) developed (in 1928) the first good model for electron emission from planar surfaces. Fowler and Nordheim assumed a single electron band, with the electron distribution in thermodynamic equilibrium at 0 K and an emitter with a flat planar surface of constant uniform local work function, with a uniform field outside it.

Carbon nanotubes (CNTs) have attracted many researchers, from a wide range of fields from academia to industry. This is not only because of their uniqueness when compared with conventional materials, but also because they are very promising FE materials, due to their properties, which include high aspect ratio, mechanical and chemical stability [2] and high

melting point as compared with conventional metal emitters. This enhanced performance has encouraged the development of many applications.

There are several types of CNT. Multi-walled carbon nanotubes (MWCNTs) were discovered in 1991 by Sumio Ijima. He found an extremely thin needle-like material when examining carbon materials using electron microscopy [3] and found the "needles" to be composed of multi-wall tubes nesting concentrically. Later, in 1993, a single-walled carbon nanotube was discovered [4]. Carbon nanotube fibers (CNTFs) are a newly designed composite material [5] based on carbon nanotubes, as shown in Fig. 1. CNTFs have radii that are much smaller than those of conventional continuous or milled carbon fibers (5-10)  $\mu\text{m}$ , but are significantly larger than those of carbon nanotubes (1-10) nm [5].

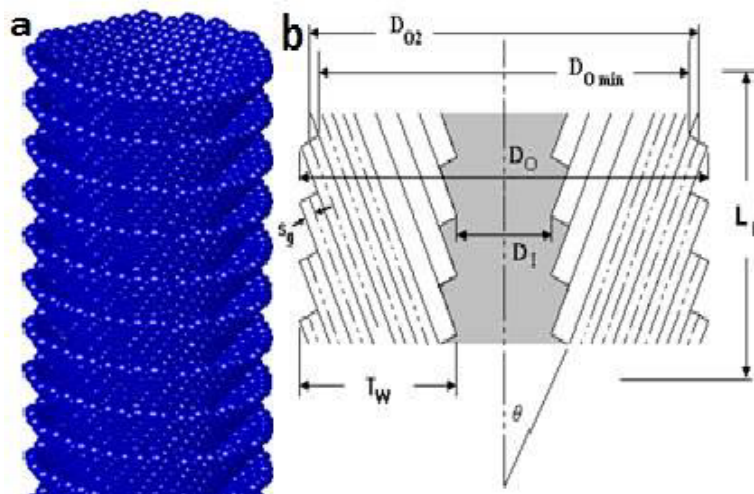


FIG. 1. (a) Artist's depiction of pyrograf II stacked-cup carbon nanotubes. (b) Cross-sectional view showing the internal structure of the pyrograf product stacked-up carbon nanotubes.

As a result of their tremendous properties, many potential applications have been proposed for CNTs and there is much interest in applications for life both now and in the future. Such applications may include electrochemical devices, hydrogen storage, sensors, high frequency electronics and more [6, 7].

In our work, the main aim behind choosing this design of emitter was to try to get emission images that consist of single bright spots. If this can be achieved, this type of electron source might be suitable as an electron microscope source.

According to the Fowler-Nordheim model (e.g., [8]), emission from planar or large-radius surfaces produces straight lines in a so-called Fowler-Nordheim (FN) plot [i.e., a plot of  $\ln(I/V^2)$  vs.  $1/V$  or alternatively  $\log_{10}(I/V^2)$  vs.  $1/V$ ]. However, almost all experimental FN plots for CNT field emitters deviate from straight lines. Possible reasons have been discussed elsewhere [8, 9].

Field electron emission (FE) occurs when the electric field strength is a few V/nm. In order to produce such high electric fields, the emitter is usually formed by a tiny tip, which has an apex radius ranging from several nanometers to sub-micrometers [10]. There are several ways to produce such a tip; we manufactured our tips by employing a drawing technique using a glass puller. To make sure that the CNTFs protrude, we break the apex of the glass tube. Fig. 2 shows a schematic diagram of the glass puller [11].

In this paper, we will discuss the current – voltage characteristics and FN plots extracted

from Pyrograf III PR-1 CNTFs. The average fiber diameter is (100-200) nm and the length is (30-100)  $\mu\text{m}$ .

## Materials and Methods

As already indicated, our emitters were prepared by the technique of pulling heated glass capillary tubes into a fine point [12]. In this technique, two bearings are located accurately on plates supported by three stainless steel rods fixed rigidly to the frame of the control unit. This frame is strong enough to serve as a stable base for the instrument. A glass tube (outside diameter = 1mm, internal diameter = 0.1 mm) fits inside these bearings, between the upper and lower chucks, with a furnace loop located around it. The CNTFs were entered into the opposite ends of each glass tube with a wire plunger and the apex was broken deliberately, so that they would protrude at the end. The lower chuck spindle can slide vertically, in order to pull the glass tube under gravity [11].

A result of applying this technique is shown in Fig. 3.

The analyses were carried out using a standard field electron emission microscope [12]. The system had been evacuated to a pressure of  $10^{-7}$  mbar after baking at around 140 °C overnight. The axial tip-screen separation is standardized at approximately 10 mm [11]. The current-voltage characteristics and related Fowler-Nordheim (FN) plots have been investigated for two samples.

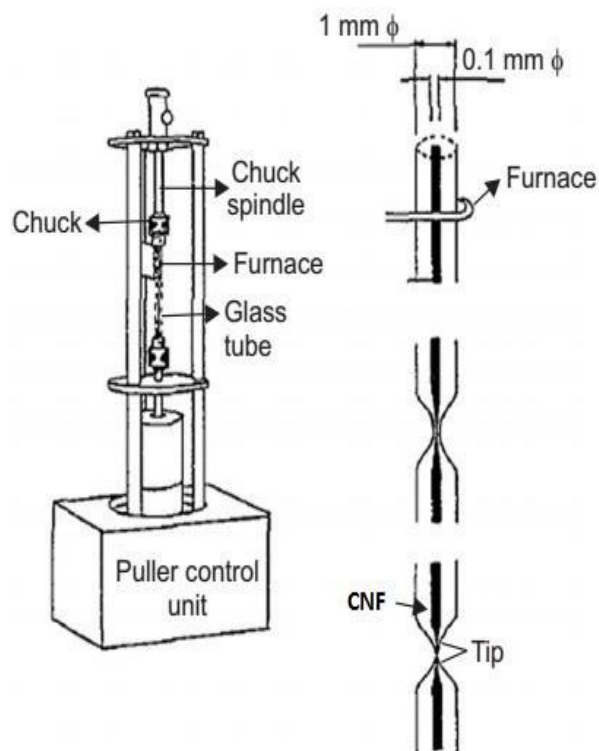


FIG. 2. A schematic diagram of the glass puller.

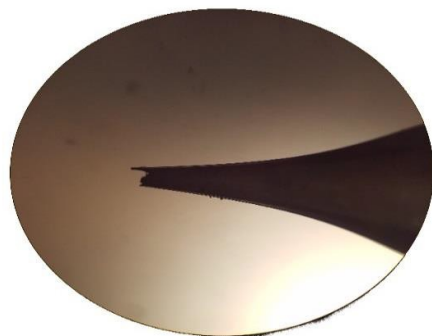


FIG. 3. Optical image of a glass capillary tube that contains CNTFs. Sample No. (CNTF-26) tip at X 50 magnification.

## Results and Discussion

The behavior of the Pyrograf III PR-1 carbon nanotube fiber is shown in Fig. 4 as the  $I$ - $V$  characteristics. Increasing the applied voltage very slowly caused an increase in the emission current until a certain value ( $V_{sw}$ ) is reached, where electron emission is suddenly initiated by a “switch-on” process. This involves the switching-on of the emission current from zero to a value of a few tenths of  $\mu\text{A}$ . In sample CNTF-26, this switch-on occurs at  $V_{sw} = 1000$  V, with an emission current of  $4.8 \mu\text{A}$ , as Fig. 4 shows. Fig. 5 shows the emission image at  $V_{sw}$ .

On further increasing the applied voltage, the emission current reaches  $8.49 \mu\text{A}$  at  $V = 1350$  V.

On decreasing the voltage, a constant-resistance regime was detected, down to a voltage  $V_C = 320$  V, at which a regime change occurs (at emission current of  $1.11 \mu\text{A}$ ). Beyond this, the current falls smoothly towards zero as the applied voltage is decreased to a threshold value  $V_{TH} = 120$  V (this is the gate voltage threshold for measurable field emission current, defined as  $5$  pA). Fig. 6 shows this  $I$ - $V$  behavior, the related FN plot at decreasing voltage and some emission images that show an electron image spot that is bigger and brighter at higher applied voltage.

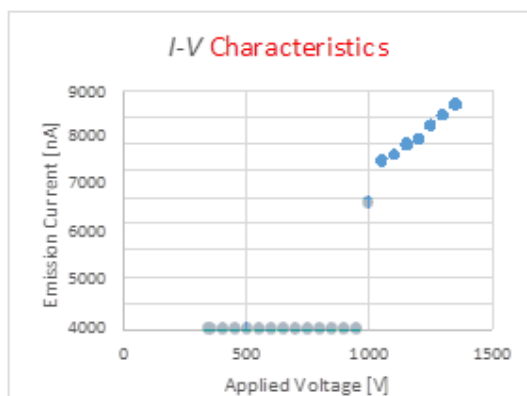


FIG. 4. Increasing voltage: the I-V characteristics for CNTF-26.



FIG. 5. Increasing voltage: field electron microscope image at  $V_{sw} = 1000$  V,  $I_{sw} = 4.8$   $\mu$ A.

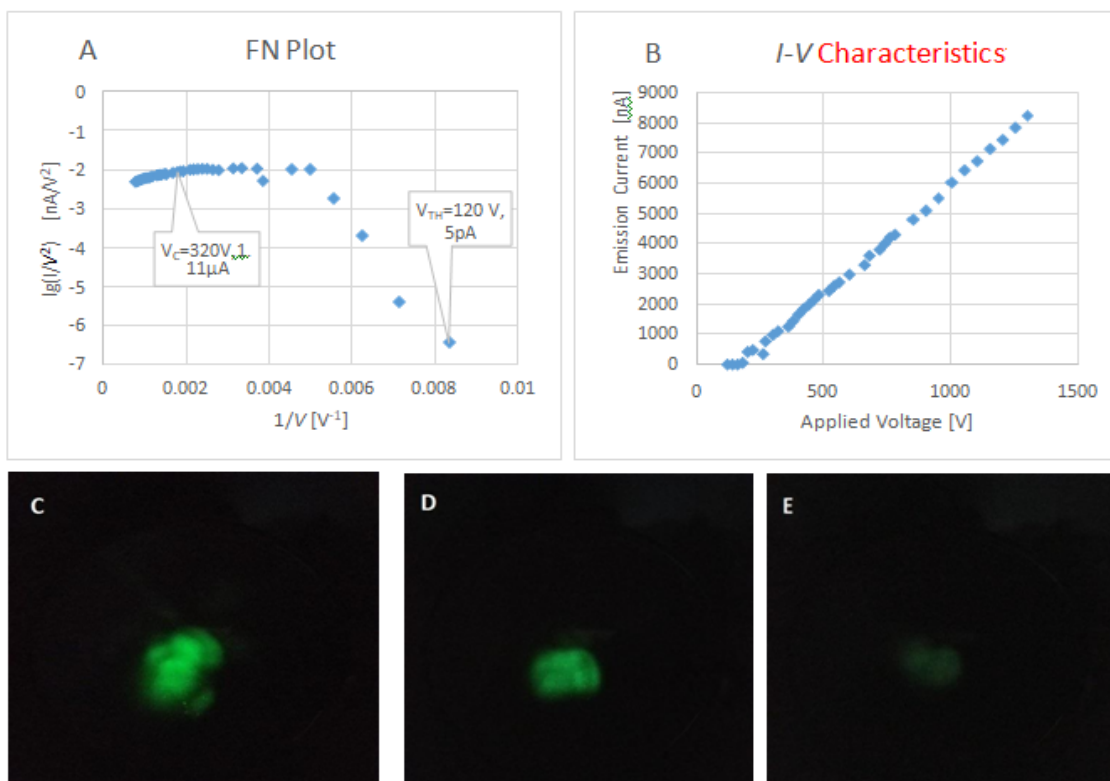


FIG. 6. Decreasing voltage: (A) FN Plot of tip CNTF-26 with slope (-1394.01) decade V. (B) I-V characteristics (C) Emission image at  $V_{SAT} = 740$  V;  $4$   $\mu$ A (D) Emission image at  $V = 600$  V;  $2.98$   $\mu$ A. (E) Emission image at  $V = 320$  V;  $1.11$   $\mu$ A.

Studies were also carried out on a second tip (Pyrograf III PR-1 CNTF No. 25). The optical micrograph in Fig. 7A shows the shape of the end of the glass tube in which the tip is embedded. The voltage was cycled up and down two times and the  $I$ - $V$  characteristics and FN plots have been studied for both cycles.

As the applied voltage is slowly increased, the emission current increases from  $I=20$  pA to  $I=12.3$   $\mu$ A. Figs. 7B and 7C show that for this emitter, the switch-on occurs at  $V_{sw} = 750$  V, at an emission current of 3.6  $\mu$ A. The current then increases linearly, again indicating a constant-resistance regime. On reducing the applied voltage, the linear region extends down to  $V=350$  V, at an emission current of 1.09  $\mu$ A.

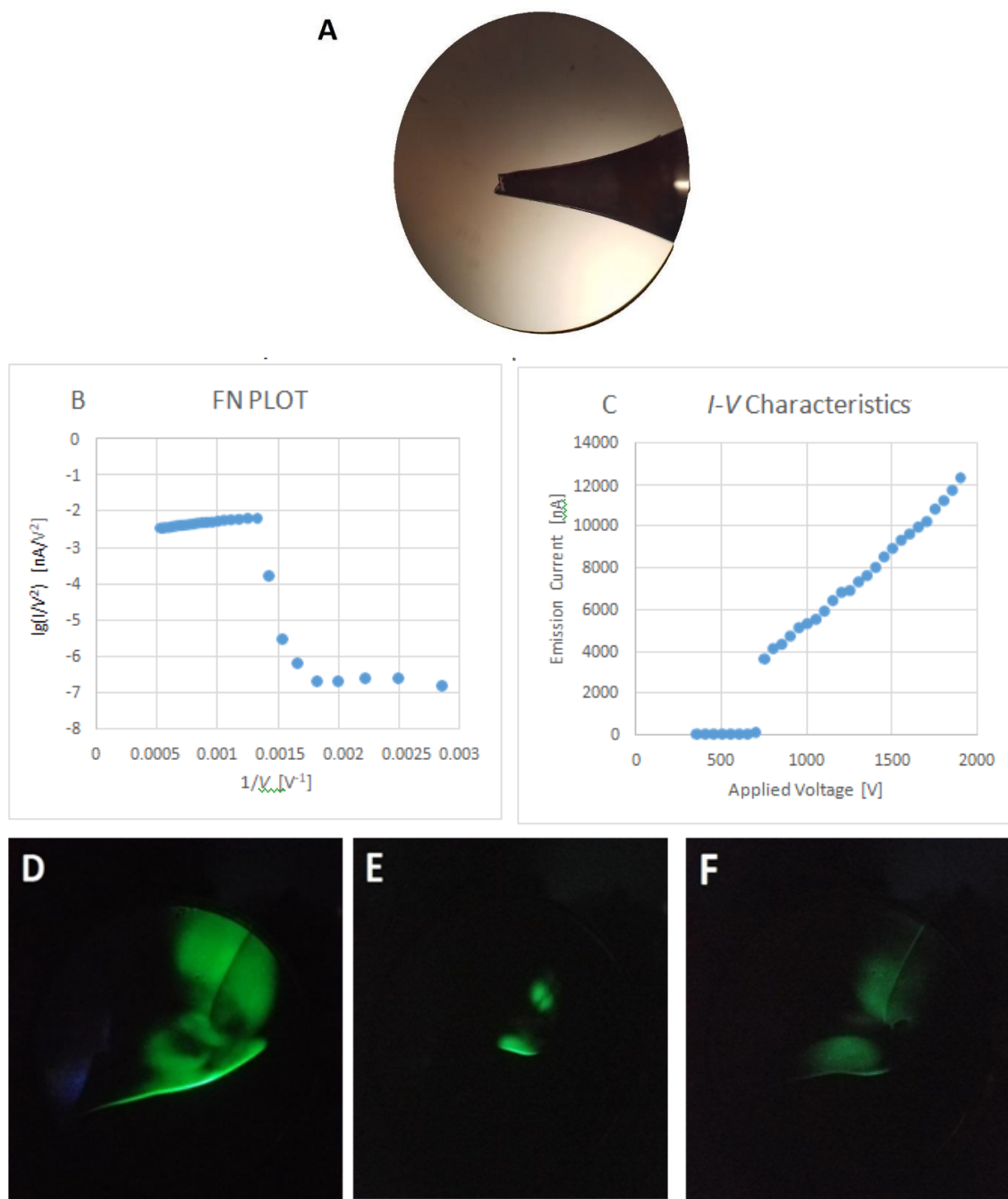


FIG. 7. (A) Optical image of a glass capillary tube that contains CNTFs. Sample No. (CNTF-25) tip at X 50 magnification. (B) FN plot.(C)  $I$ - $V$  characteristics. (D) Emission image at  $V_{sw} = 750$  V; 3.6  $\mu$ A. (E) Emission image before switch-on at  $V=700$  V; 80 nA. (F) Emission image at  $V_{SAT} = 350$  V; 1.09  $\mu$ A.

In both cases, the FN plot "saturates" even though the current-voltage relationship is linear. This shows clearly that FN-plot saturation can be a mathematical effect that occurs even though the emission current does not physically saturate.

We then repeated the experiment for the same tip (CNTF Pyrograf III PR-1 No. 25) under the same conditions. Fig. 8 and the following figures show the cycle of increasing and decreasing the applied voltage. Figs. 8A and 8B show that the emission current increases from 20

pA to 8.34  $\mu\text{A}$ , without showing "switch-on" phenomenon as voltage increases from 200 V to 1450 V. When the voltage is decreased, the emission current decreases linearly from 8  $\mu\text{A}$  to 8 pA, beyond which the current falls smoothly towards zero as the applied voltage is decreased to a threshold value  $V_{\text{TH}} = 150$  V (where the emission current is 8 pA), as Fig. 9 shows.

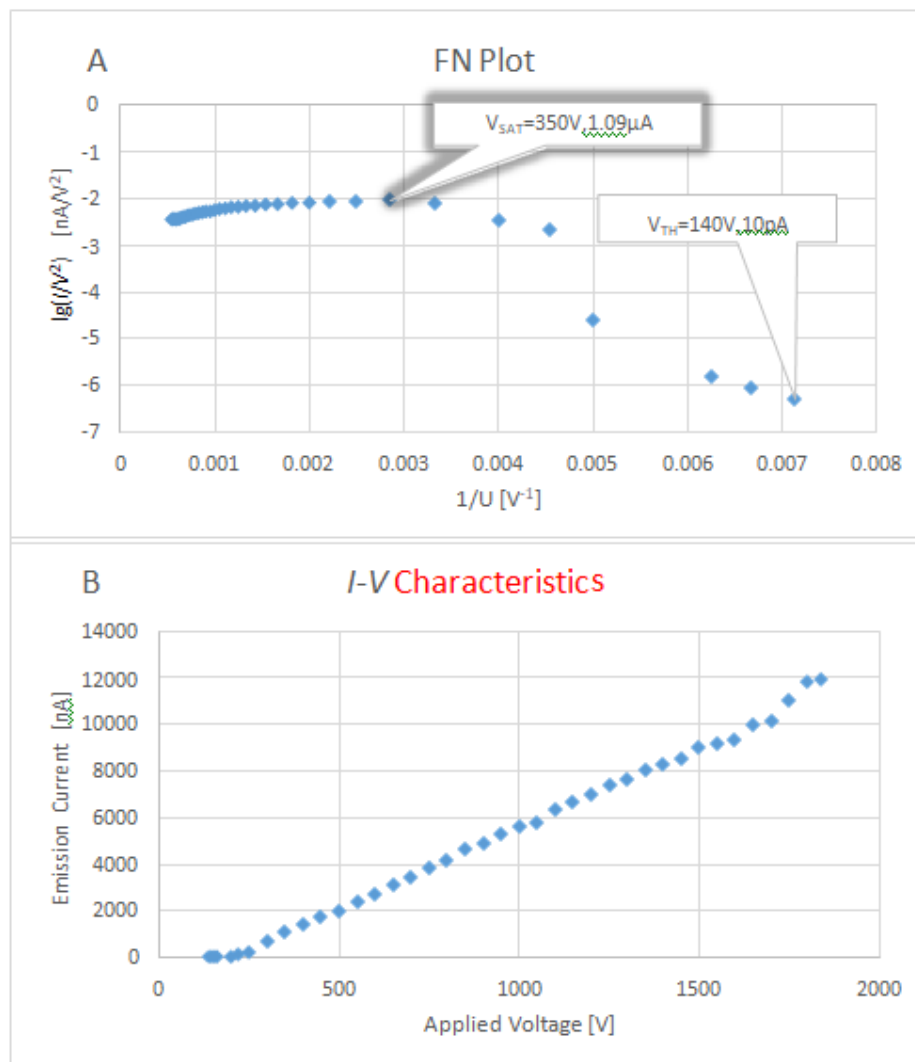


FIG. 8. CNTF-26 decreasing voltage. (A) FN plot with slope (-1296) decade V. (B) I-V characteristics.

Fig. 11 shows a collection of emission images during the second cycle of voltage. In contrast to the first cycle, the emitter produces a single bright spot and we notice that increasing the applied voltage causes the spot to spread.

As indicated above, the current-voltage characteristics are linear, suggesting that there is a large resistance somewhere in the circuit. This causes the FN plots to be non-linear and may also lead to voltage drops in the circuit that would cause shifts in the total electron energy



distribution. If these shifts happen, they would probably make this form of emitter unsuitable as an electron microscope source. There may also be other reasons behind the non-linearity in the

FN plots, such as adsorption effects, emission-current dependence in the field enhancement factor or local conversion length and conceivably space-charge effects.

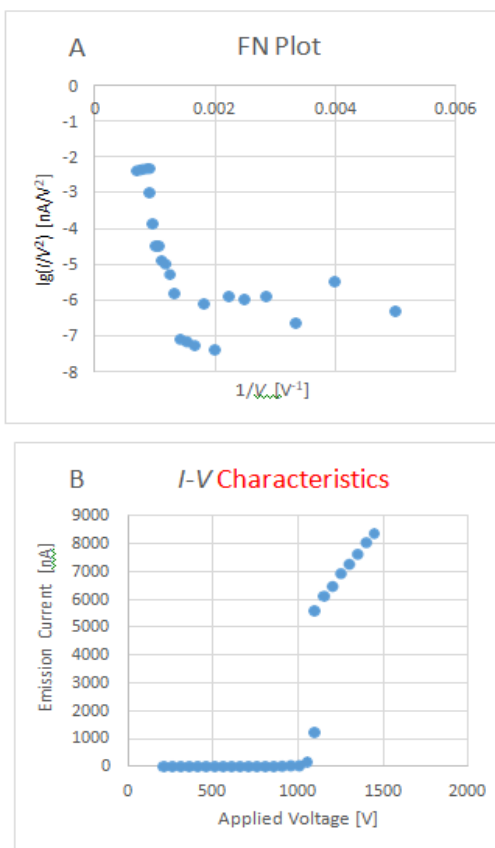


FIG. 9. Increasing voltage: (A) FN Plot for tip CNTF-25 (B) I-V characteristics range (200-1450)V with emission current range (20 pA - 8.34  $\mu$ A).

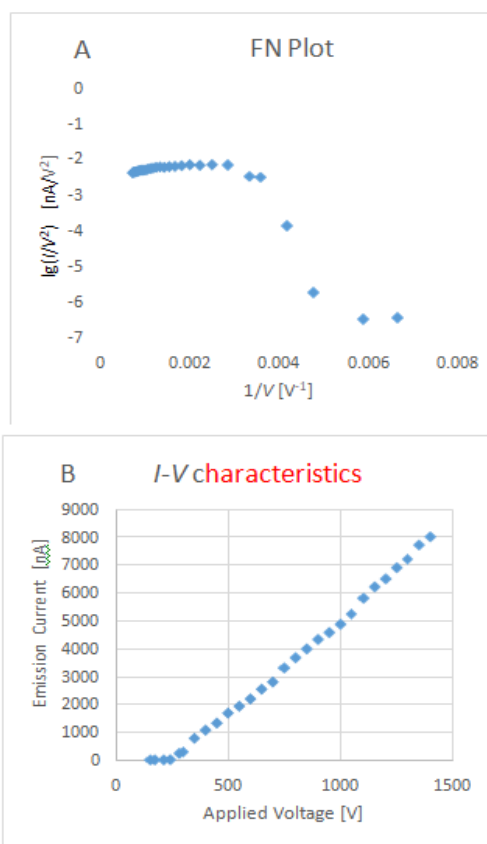


FIG. 10. Decreasing voltage: (A) FN plot for tip CNTF-25. (B) I-V characteristics range (150-1400) V, with emission current range (8 pA - 8  $\mu$ A).

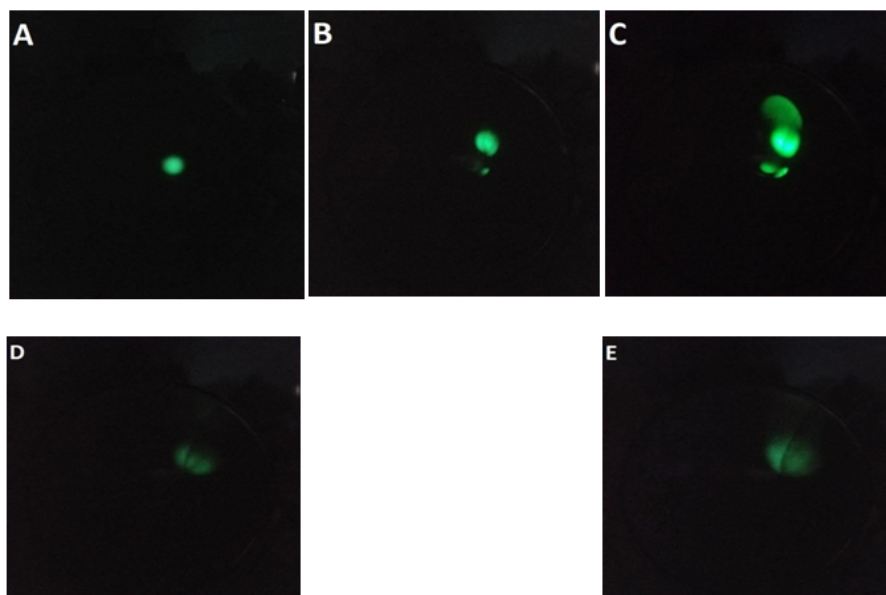


FIG. 11. By increasing voltage, emission images at voltage values: (A) 850 V,  $I=7.2$  nA. (B) 950 V,  $I=20.81$  nA. (C) 1050 V,  $I=0.157$   $\mu$ A. By decreasing voltage (D)  $V=280$  V,  $I=0.24$   $\mu$ A. (E)  $V=300$  V,  $I=0.29$   $\mu$ A.

We also note that, in some emission images in Fig. 7, there are irregularities and a bright streak at the edge of the image. The cause of this could be the irregular shape of the CNTFs or possibly charging of the end of the glass tube (Forbes, private communication, 2017).

The importance of CNTs and related materials has led scientists to make extensive investigations to understand their FE behavior. For CNTFs, detailed studies have been conducted by Cahay and collaborators [13], who looked at many of the factors that influence FE, including the density of active field emitters (assuming that the CNTFs splay apart at the ends into individual CNTs), the emission mechanism, the emission geometry, the fiber condition, current-voltage loop behavior and outgassing issues. Fig. (12) compares their  $I$ - $V$  characteristics with ours.

Fig. (12A) shows Cahay's characteristics [13] for CNTFs at different separations ( $d_{\text{gap}}$ ) between

anode and cathode (2, 1.75, 1.50, 1.25 mm), where  $E_{\text{AG}}$  is the "apparent gap field" defined by  $V/d_{\text{gap}}$  and  $V$  is the measured voltage between anode and the grounded cathode. These characteristics should be compared with our characteristics as shown in Figs. 7C and 9A. The two sets of characteristics are not quite the same, because the characteristics as found by Cahay et al. [13] exhibit a departure from linearity at high fields and voltages. Also, in our experiments, the distance between cathode and anode was 10 mm and the highest emission current ranged between 8 and 12.2  $\mu\text{A}$ ; in Cahay's experiments (at significantly smaller gaps), the highest emission current ranged between 0.6 and 2.2 mA. There are various possible reasons for the differences between our results and Cahay's results, including the likelihood that Cahay's emitters have a different physical structure from ours. We hope to explore these matters further in future studies.

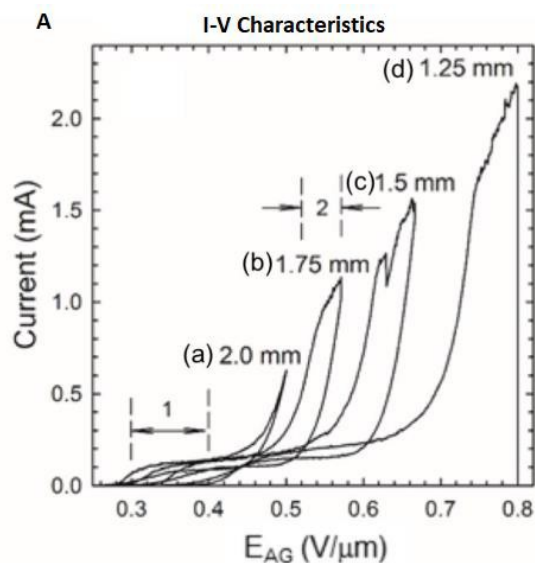


FIG. 12. I-V characteristics for CNTFs after Cahay [13], for different distances between anode and cathode.

## Conclusions

Pyrograf III PR-1 carbon nanotube fiber emitters have been prepared by employing a drawing technique using a glass puller and their  $I$ - $V$  characteristics, FN plots and emission images have been studied. These sources seem capable of producing a single bright field electron emission spot. This may be of potential use in some electron-beam applications, but these emitters will probably be unsuitable as electron microscope sources, for the following reasons. We have been employing a locally

smooth emitter tip, embedded in a glass tube. The single emission spot occurs at low applied voltage, where the number of separate emission sites is lowest. Because of the nonmetallic nature of the tip, field penetration, fluctuation of the applied potential, shifts in the position of the emitting levels, and particularly if the current flow through the emitter leads to significant voltage loss (in accordance with Ohm's law), there may be current-dependent shifts in the emitter energy distribution. These shifts would make the source unsuitable as a source for an electron microscope (or for any other electron

beam instrument where sharp focusing is required).

The most interesting feature of our results is perhaps the fact that our current-voltage characteristics are linear; hence the measured current-voltage characteristics do not obey any Fowler-Nordheim-like equation and the related FN plots have a curious characteristic non-linear shape. Experimental FE situations that generate linear  $I$ - $V$  characteristics are relatively unusual.

We have also established that our CNTFs appear to have slightly different behavior from those of Cahay et al. [13]; the reasons for this difference remain to be explored.

### Acknowledgment

We thank Dr. Richard G. Forbes, of the University of Surrey, UK, for discussion and helpful comments.

---

### References

- [1] Forbes, R.G., J. Vac. Sci. Technol. B, 26 (2008) 788.
- [2] Lan, Y., Wang, Y. and Ren, Z., Adv. Phys., 60 (2011) 553.
- [3] Ijima, S., Nature, 354 (1991) 56.
- [4] Ijima, S. and Ichihashi, T., Nature, 363 (1993) 603.
- [5] See: [www.apsci.com](http://www.apsci.com)
- [6] Bandaru, P.R., J. Nanosci. Nanotechnol., 7 (2007) 1239.
- [7] Baughman, R.H., Zakhidov, A.A. and de Heer, W.A., Science, 297 (2002) 287.
- [8] Forbes, R.G., Deane, J.H.B., Fischer, A. and Mousa, M.S., Jordan J. Phys., 8 (2015) 125.
- [9] Dean, K.A. and Chalamala, B.R., Appl. Phys. Lett., 76 (2000) 375.
- [10] Li, Y.-H., Sun, Y.-H. and Yeow, J.T.W., Nanotechnology, 26 (2015) 242001.
- [11] Bani Ali, E.S. and Mousa, M.S., Appl. Microsc., 46 (2016) 244.
- [12] Mousa, M.S. and Hibbert, D.B., J. Phys. D: Appl. Phys., 26 (1993) 697.
- [13] Cahay, M., Murray, P.T., Back, T.C., Fairchild, S., Boeckl, J., Bulmer, J., Koziol, K.K.K., Gruen, G., Sparkes, M., Orozco, F. and O'Neill, W., Appl. Phys. Lett., 105 (2014) 172107.



### Neutron-Induced Reactions in Nuclear Astrophysics

R. Reifarh<sup>a</sup>, D. Brown<sup>b</sup>, S. Dababneh<sup>c</sup>, Y. A. Litvinov<sup>d</sup> and S. M. Mosby<sup>e</sup>

<sup>a</sup> Goethe University Frankfurt, Frankfurt, Germany.

<sup>b</sup> Brookhaven National Laboratory, Upton, NY, USA.

<sup>c</sup> Department of Physics, Faculty of Science, Al-Balqa Applied University, Salt, Jordan.

<sup>d</sup> GSI Helmholtz Zentrum für Schwerionenforschung, Darmstadt, Germany.

<sup>e</sup> Los Alamos National Laboratory, Los Alamos, USA.

---

Received on: 24/7/2017;

Accepted on: 19/11/2017

---

**Abstract:** The quest for the origin of the chemical elements, which we find in our body, in our planet (Earth), in our star (Sun) or in our galaxy (Milky Way), could only be resolved with a thorough understanding of the nuclear physics properties of stable and unstable atomic nuclei. While the elements until iron are either created during the big bang or during fusion reactions in stars, most of the elements heavier than iron are produced *via* neutron-induced reactions. Therefore, neutron capture cross-sections of stable and unstable isotopes are important.

So far, time-of-flight or activation methods have been applied very successfully, but these methods reach their limits once the isotopes with half-lives shorter than a few months are of interest. A combination of a radioactive beam facility, an ion-storage ring and a high-flux reactor or a spallation source would allow a direct measurement of neutron-induced reactions over a wide energy range of isotopes with half-lives down to minutes.

The idea is to measure neutron-induced reactions on radioactive ions in inverse kinematics. This means that the radioactive ions will pass through a neutron target. In order to efficiently use the rare nuclides as well as to enhance the luminosity, the exotic nuclides can be stored in an ion-storage ring. The neutron target can be the core of a research reactor, where one of the central fuel elements is replaced by the evacuated beam pipe of the storage ring. Alternatively, a large moderator surrounding a spallation source can be intersected by the beam pipe of an ion-storage ring. Using particle detectors and Schottky spectroscopy, most of the important neutron-induced reactions, such as (n, $\gamma$ ), (n,p), (n, $\alpha$ ), (n,2n) or (n,f), could be investigated.

**Keywords:** Neutron-induced reactions, Neutron target, Nucleosynthesis, Storage rings.

## Introduction

The quest for the origin of the chemical elements, which we find in our body, in our planet (Earth), in our star (Sun) or in our galaxy (Milky Way), could only be resolved with a thorough understanding of the nuclear physics properties of stable and unstable atomic nuclei [1, 2]. While the elements until iron are either created during the big bang or during fusion reactions in stars, most of the elements heavier than iron are produced *via* neutron-induced reactions of about equal contributions from the

slow (s) and the rapid (r) neutron capture process [3], see FIG. 1. Therefore, neutron capture cross-sections of stable and unstable isotopes are important for a quantitative understanding.

During the s process, a given reaction can affect the abundance of only a few local isotopes, typically downstream of the reaction or a large number acting globally on the neutron exposure [4]. Neutron capture cross-sections play an important role also during the r process. In hot r-process scenarios, they become

important during the freeze-out phase [5, 6]. In cold r-process models, like neutron star mergers, neutron capture rates are important even during the merging process [7].

Even the production of the rare proton-rich isotopes can be affected by neutron capture processes. Those nuclei are typically produced by sequences of proton-induced or gamma-induced reactions starting from an s- or r-process seed [8]. Neutron captures on proton-rich, short-lived nuclei affect the final abundance distribution of the important p nuclei  $^{92,94}\text{Mo}$  [9].

So far, time-of-flight or activation methods have been applied very successfully close or at the valley of stability, but these methods reach their limits once isotopes with half-lives shorter than a few months are of interest [10]. A combination of a radioactive beam facility, an ion-storage ring and a high-flux reactor or a spallation source would allow a direct measurement of neutron-induced reactions over a wide energy range of isotopes with half-lives down to minutes [11, 12].

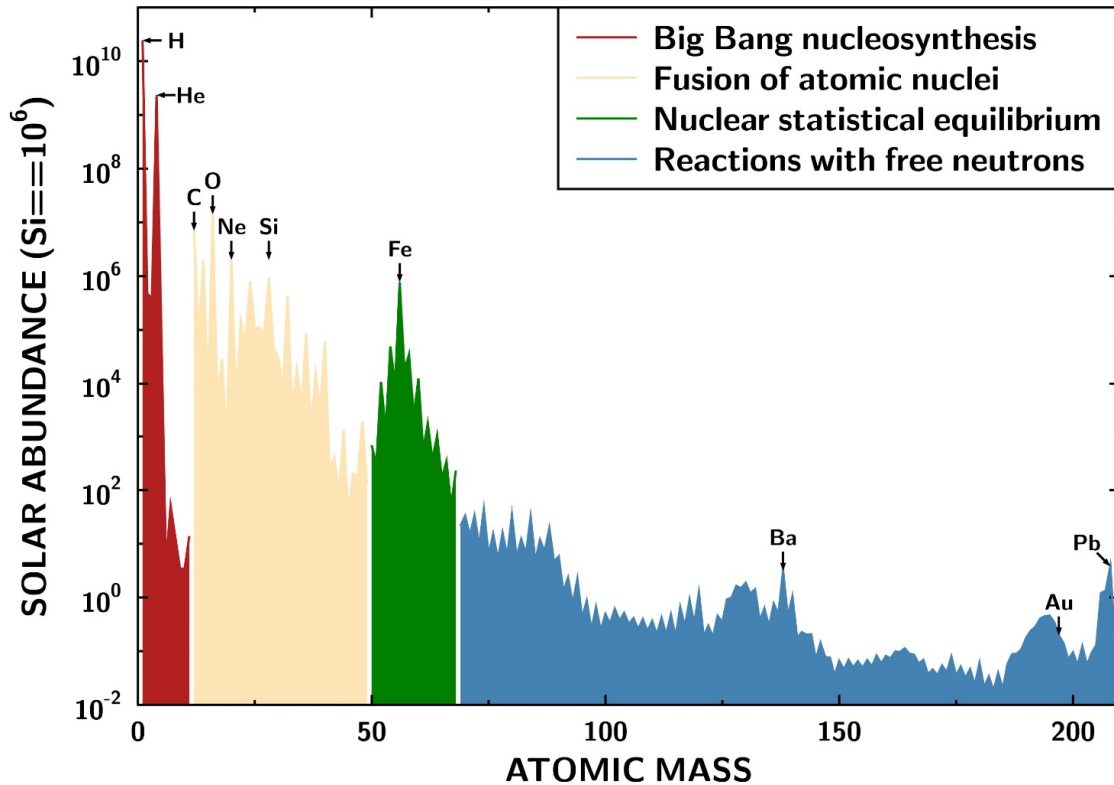


FIG. 1. The solar abundances of the atomic nuclei as a function of their mass [13]. The structures observed can be explained by different processes contributing to the overall nucleosynthesis. The lightest elements—hydrogen, helium—are produced in the Big Bang (red), while the elements up to iron are synthesized during stellar burning phases *via* fusion of charged particles (beige). During the extremely hot last stellar burning phase—the silicon burning—the isotopes around iron (mass 56), which are most tightly bound, are produced in the nuclear statistical equilibrium (green). Almost all of the elements with higher proton numbers than iron are produced through neutron-induced processes (blue).

### A Spallation-Based Neutron Target

The idea is to measure neutron-induced reactions on radioactive ions in inverse kinematics. This means that the radioactive ions will pass through a neutron gas. In contrast to charged particle-induced reaction rates like  $(p,\gamma)$  or  $(\alpha,\gamma)$ , where the inversion of kinematics implies a target of stable atoms like hydrogen or

helium, the challenge is now to provide a target of free neutrons. In order to efficiently use the rare nuclides as well as to enhance the luminosity, the exotic nuclides should be stored in an ion-storage ring [14]. The neutron target can be the core of a research reactor, where one of the central fuel elements is replaced by the evacuated beam pipe of the storage ring [11]. Alternatively, a large moderator surrounding a

spallation source can be intersected by the beam pipe of an ion-storage ring [12], see FIG. 2. In this paper, we discuss parameter studies, which go beyond the basic concept published in previous papers. In particular, the geometry of the moderator needs to be studied very carefully, since large amounts of valuable material are necessary. A second aspect is the design of the spallation target itself, which can be optimized in terms of geometry and material. All simulations

presented here were performed with 4 different energies: 200 MeV, 800 MeV, 4 GeV and 20 GeV. These energies were chosen, since they correspond to accelerators in operation or under construction, which might be used in combination with a spallation target. We will show later that the neutron density increases with the proton energy. Reduced beam energy can therefore be compensated by increased beam current.

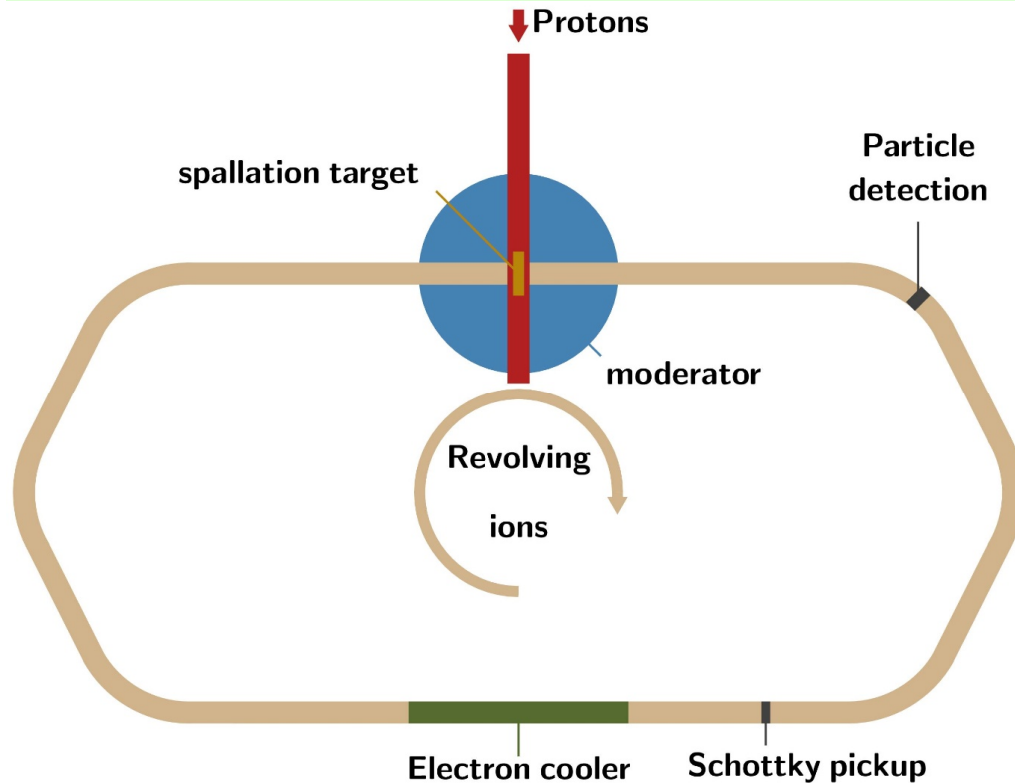


FIG. 2. Sketch of the proposed setup to investigate neutron-induced reactions in inverse kinematics. The isotopes under investigation will be stored in a ring, which penetrates a neutron moderator. This moderator acts as a trap for neutrons produced during a spallation reaction. Therefore, the neutron gas acts as a neutron target. See [12] for more details. The particle detectors can be silicon detectors just outside the unreacted beam [14].

### Moderator Material

All the simulations published so far [12] have been performed assuming a heavy-water moderator. However, other materials should be considered too, in particular if the moderator is not very large. FIG. 3 shows the results for a 800 MeV proton beam hitting a small tungsten target. Different moderator materials and thicknesses have been investigated. It is very interesting to see that materials like beryllium or even regular (light) water have a better performance than heavy water for small moderators. But, most materials reach a maximum neutron density already within the limits of the investigated

moderator thicknesses. The explanation can be found in FIG. 4. Already 1 m of moderator material absorbs a significant fraction of the neutrons, except for heavy water. Therefore, a further enlargement of the moderator does not improve the performance anymore, since the neutrons are already absorbed inside the moderator, mostly *via* neutron captures on the moderator material. Beryllium is the best material below a moderator radius of 1.5 m. Deuterated polyethylene ( $\text{CD}_2$ ) is the best option for moderators between 1.5 and 2 m radius. Heavy water is only the best option for very large moderators.

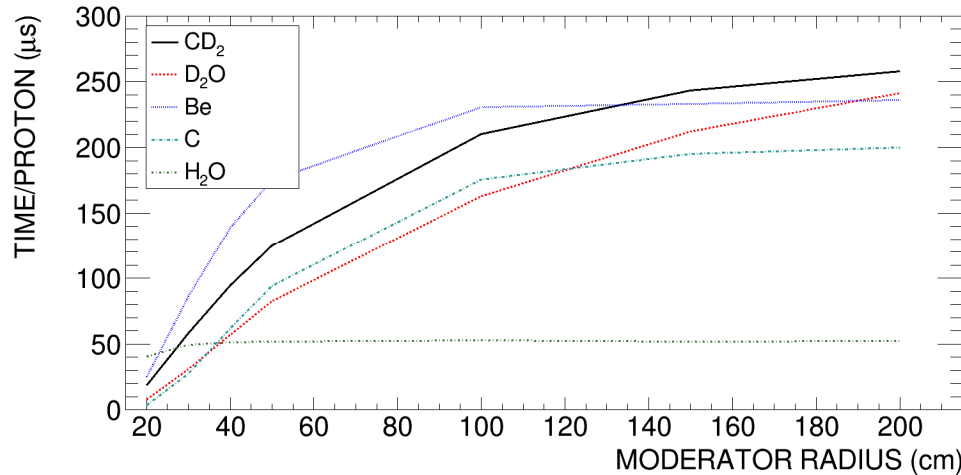


FIG. 3. Total time per impinging proton spent by neutrons inside the beam pipe. The total time is directly proportional to the density of the neutron target. The simulations were performed with a proton beam of 800 MeV hitting a tungsten cylinder of 10 cm length and 3 cm diameter.

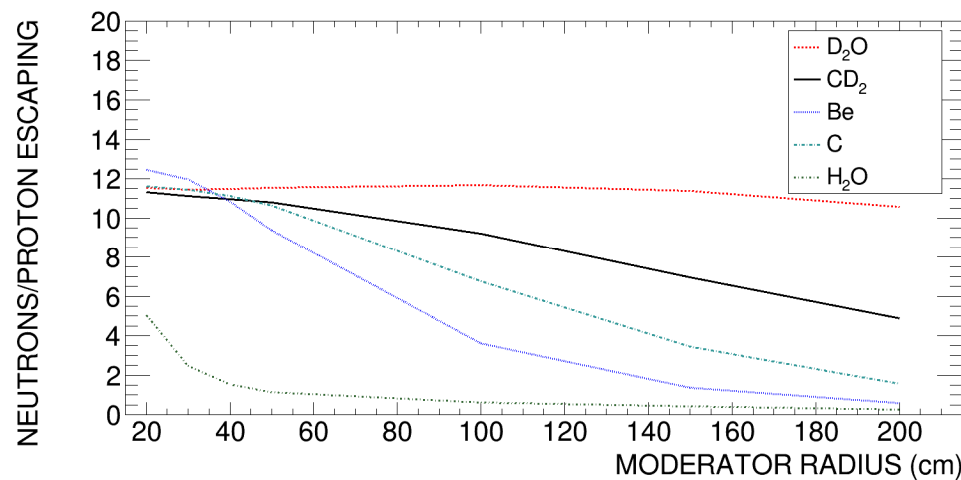


FIG. 4. Number of neutrons escaping the moderator. The simulations were performed with a proton beam of 800 MeV hitting a tungsten cylinder of 10 cm length and 3 cm diameter.

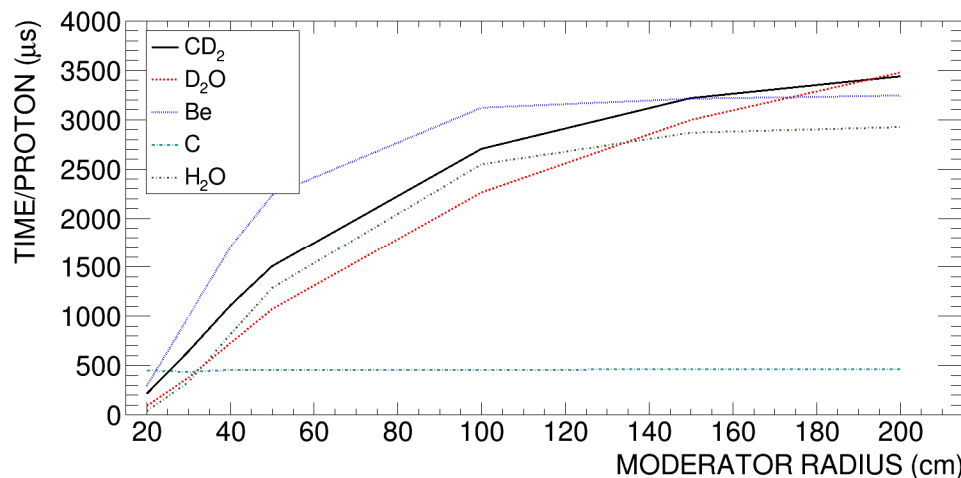


FIG. 5. Total time per impinging proton spent by neutrons inside the beam pipe. The total time is directly proportional to the density of the neutron target. The simulations were performed with a proton beam of 20 GeV hitting a tungsten cylinder of 50 cm length and 4.8 cm diameter.



A similar effect can be observed for a 20 GeV proton beam hitting a large tungsten target of 50 cm length and 4.8 cm diameter, see FIG. 5 and FIG. 6. Also here, beryllium would be the best choice for moderators smaller than 1.5 m. Above 1.5 m, CD<sub>2</sub> and D<sub>2</sub>O yield almost the same neutron density.

At lower proton energies of 200 MeV, the turn-over between Be and CD<sub>2</sub> occurs already at a moderator radius of 1 m (FIG. 7). The reduction of the total scale is important to recognize. The maximum time spent by neutrons

in the ion beam pipe is about 35 μs / proton in the case of a 200 MeV beam and close to 3500 μs / proton in the case of a 20 GeV beam. However, it is interesting to note that the maximum number of spallation neutrons per proton energy is reached around 1 GeV.

We also investigated the idea of combining different moderator materials in shells. But, it turned out that pure moderators always perform better, see for example FIG. 8.

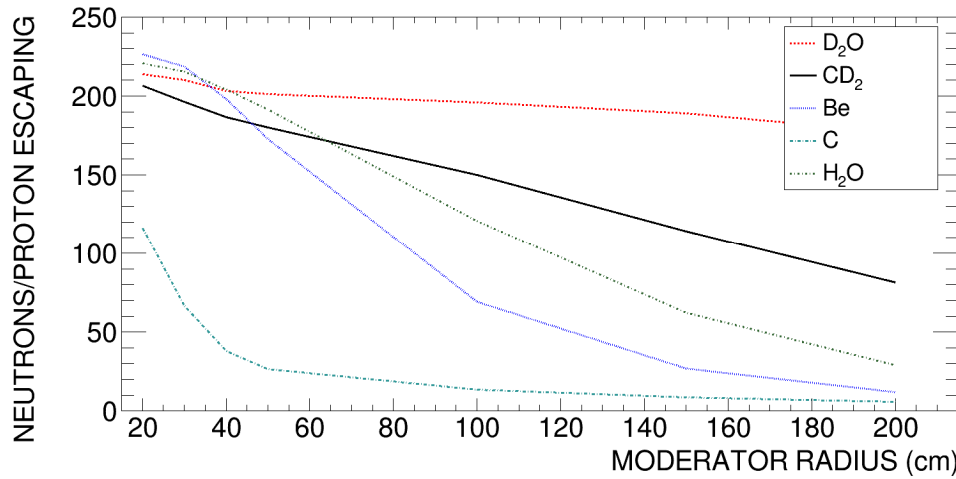


FIG. 6. Number of neutrons escaping the moderator. The simulations were performed with a proton beam of 20 GeV hitting a tungsten cylinder of 50 cm length and 4.8 cm diameter.

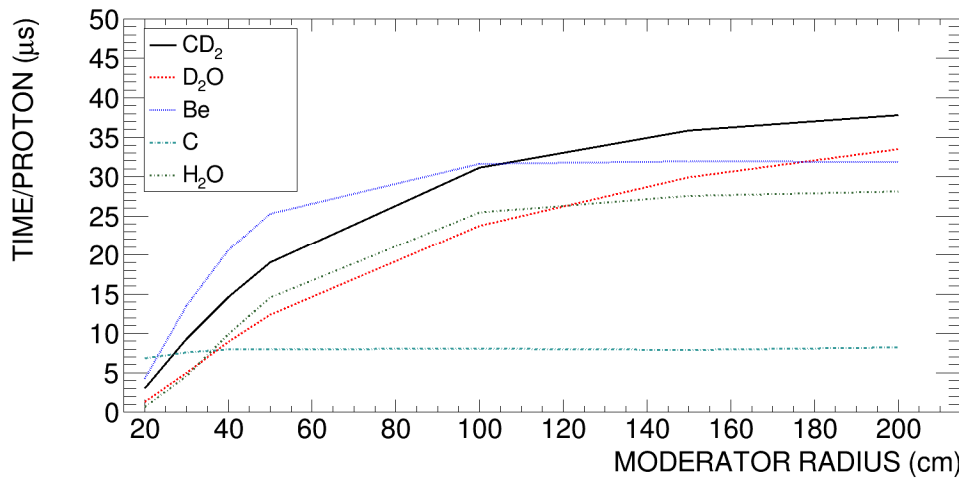


FIG. 7. Total time per impinging proton spent by neutrons inside the beam pipe. The total time is directly proportional to the density of the neutron target. The simulations were performed with a proton beam of 200 MeV hitting a tungsten cylinder of 3 cm length and 3 cm diameter.

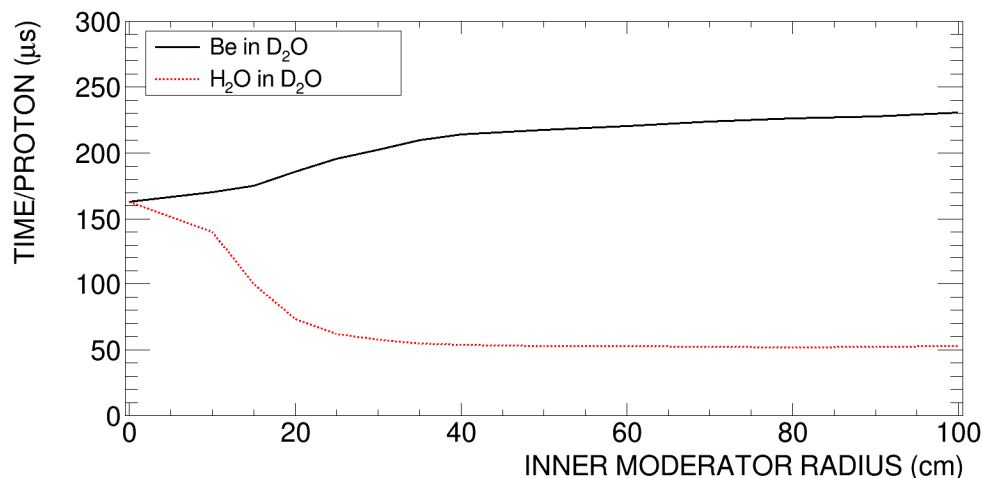


FIG. 8. Investigation of a layered moderator. The outer radius was fixed at 1 m and the outer shell was heavy water. The radius of the inner shell varied between 0 and 1 m. Hence, the point at 0.0 corresponds to a pure heavy water moderator of 1 m. The points at 1 m correspond to pure moderators of Be and light water.

### Spallation Target

The material as well as the geometry of the spallation target itself have an impact on the number of neutrons inside the ion beam pipe. FIG. 9 shows a set of simulations, where the length of the spallation target was varied for two high-Z materials; tungsten and bismuth. The

beam energies were 4 and 20 GeV. The overall performance of the two materials is very similar, but because of the lower density, the optimal target length for bismuth is larger than for tungsten. FIG. 10 and FIG. 11 show the results of similar investigations, but for beam energies of 800 MeV and 200 MeV.

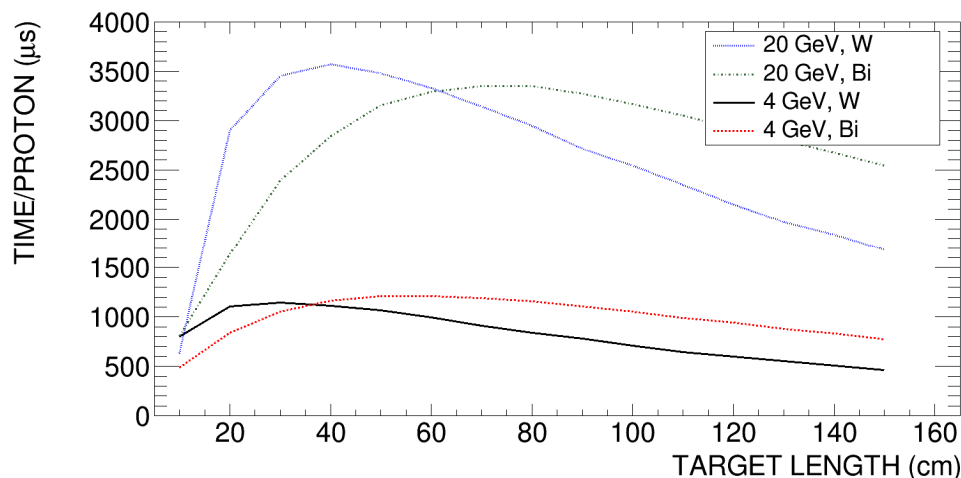


FIG. 9. Total time per impinging proton spent by neutrons inside the beam pipe. The total time is directly proportional to the density of the neutron target. The simulations were performed with proton beams of 4 GeV and 20 GeV hitting a tungsten or bismuth cylinder of 4.8 cm diameter and different lengths. The moderator for this set of simulations was always  $D_2O$  with a radius of 2 m.

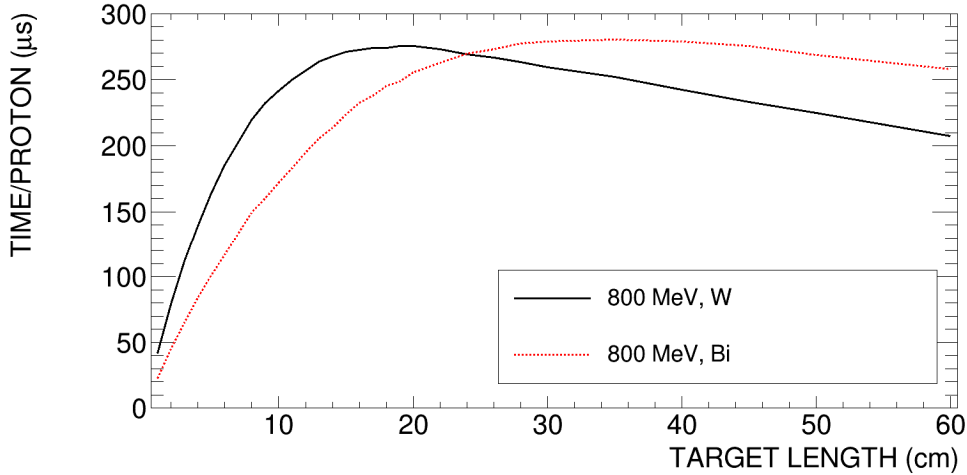


FIG. 10. Total time per impinging proton spent by neutrons inside the beam pipe. The total time is directly proportional to the density of the neutron target. The simulations were performed with a proton beam of 800 MeV hitting a tungsten or bismuth cylinder of 3 cm diameter and different lengths. The moderator for this set of simulations was always  $D_2O$  with a radius of 2 m.

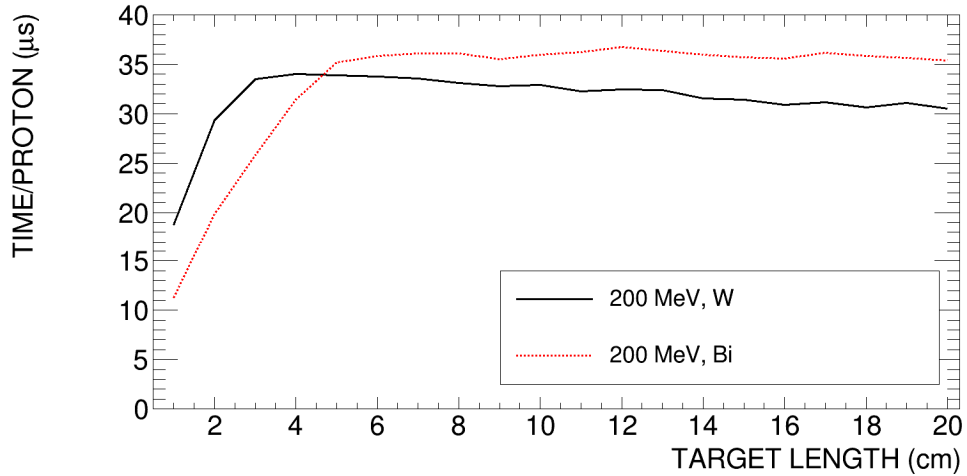


FIG. 11. Total time per impinging proton spent by neutrons inside the beam pipe. The total time is directly proportional to the density of the neutron target. The simulations were performed with a proton beam of 200 MeV hitting a tungsten or bismuth cylinder of 3 cm diameter and different lengths. The moderator for this set of simulations was always  $D_2O$  with a radius of 2 m.

## Conclusions

In order to estimate the actual density of the neutron target as seen by the revolving ions, one needs to multiply the times spent by neutrons as given in the figures above by the number of protons per time and divide by the cross-section of the beam pipe. The simulated beam pipe has a diameter of 5 cm corresponding to a cross-section of about  $20 \text{ cm}^2$ .

Table 1 shows the maximum values of the times/proton spent by neutrons inside the ion beam pipe for different beam energies, tungsten target and a 2 m moderator. In addition, the corresponding neutron densities per  $\mu\text{A}$  beam

current are listed. Since the maximum of the neutron production per beam energy is around 1 GeV, the recommended setup would consist of an accelerator of about 1 GeV and a tungsten target of about 20 cm length.

The achievable vacuum conditions in the ring, the charge number and the charge state of the investigated ions determine the life time of the stored ions. Interactions with the rest gas will determine the lowest energies in the center of mass. A highly-optimized ring with reasonably low charge states should be able to store heavy ions down to 100 AkeV. This would cover the energy regime of hot, explosive stellar environments, like the  $\gamma$  process or the r process.

Even though the second phase of the weak s process in massive stars occurs during the carbon shell burning, temperatures around 90 keV are reached [15]. The restrictions on half-life of the isotopes are given by the requirement of a reasonably high duty cycle. The radioactive ions need to be produced, the beam stored, cooled and slowed down and the measurement performed. The beam preparations require currently several minutes [14], hence the half-life limit would be in this range. The reactions,

which are possible to investigate, depend on the detection method. Using particle detectors and Schottky spectroscopy, most of the important neutron-induced reactions, such as  $(n,\gamma)$ ,  $(n,p)$ ,  $(n,\alpha)$ ,  $(n,2n)$  or at higher energies even  $(n,f)$ , can be investigated [11].

The proposed setup would therefore significantly contribute to our understanding of the origin of the elements heavier than iron.

TABLE 1. Number of neutrons/proton entering the moderator, maximum neutron time and density inside the ion beam pipe, assuming a tungsten target, a D<sub>2</sub>O moderator of 2 m radius and 1  $\mu$ A beam current.

Proton energy (GeV)	Neutrons/Proton (produced)	Time per proton ( $\mu$ s)	Neutron density ( $\text{cm}^{-2} \mu\text{A}^{-1}$ )
0.2	1.2	34	$1.1 \cdot 10^7$
0.8	12	275	$8.8 \cdot 10^7$
4	54	1140	$3.6 \cdot 10^8$
20	176	3570	$1.1 \cdot 10^9$

## Acknowledgements

This research has received funding from the European Research Council under the European Union's Seventh Framework Programme

(FP/2007-2013)/ERC Grant Agreement No. 615126.

## References

- [1] Burbidge, E.M. et al., *Rev. Mod. Phys.*, 29 (1957) 547.
- [2] Wallerstein, G. et al., *Rev. Mod. Phys.*, 69 (1997) 995.
- [3] Reifarth, R., Lederer, C. and Käppeler, F., *J. Phys. G: Nucl. Part. Phys.*, 41 (2014) 053101.
- [4] Koloczek, A. et al., *Atomic Data and Nuclear Data Tables*, 108 (2016) 1.
- [5] Arcones, A. and Thielemann, F.-K., *Journal of Physics G: Nuclear Particle Physics*, 40 (2013) 3201.
- [6] Surman, R. and Engel, J., *Physical Review C*, 64 (2001).
- [7] Mumpower, M.R. et al., *Progress in Particle and Nuclear Physics*, 86 (2016) 86.
- [8] Pignatari, M. et al., *International Journal of Modern Physics E*, (2016) 25.
- [9] Göbel, K. et al., in: *European Physical Journal Web of Conferences*, (2015).
- [10] Couture, A. and Reifarth, R., *Atomic Data and Nuclear Data Tables*, 93(5) (2007) 807.
- [11] Reifarth, R. and Litvinov, Y.A., *Physical Review, Special Topics: Accelerators and Beams*, 17 (2014) 14701.
- [12] Reifarth, R. et al., *Physical Review, Special Topics: Accelerators and Beams*, 20 (2017).
- [13] Palme, H., Lodders, K. and Jones, A., in: *Planets, Asteroids, Comets and the Solar System*, A.M. Davis, Editor, (2014) 15.
- [14] Mei, B. et al., *Physical Review C*, 92 (2015) 35803.
- [15] Pignatari, M. et al., *The Astrophysical Journal*, 710 (2010) 1557.

### Modeling the Electrical Impedance of Epoxy Polymer/Carbon Black Composite Materials

Z. Samir<sup>a</sup>, R. Belhimria<sup>a</sup>, S. Boukheir<sup>a,b</sup>, M. E. Achour<sup>a</sup> and L. C. Costa<sup>c</sup>

<sup>a</sup> LASTID Laboratory, Department of Physics, Faculty of Sciences, Ibn Tofail University, BP 133, 14000 Kenitra, Morocco.

<sup>b</sup> LNEE Laboratory, Department of Physics, Faculty of Sciences, Cadi Ayyad University, B.P. 2390, 40000 Marrakech Morocco.

<sup>c</sup> I3N and Physics Department, University of Aveiro, 3810-193 Aveiro, Portugal.

---

Received on: 24/7/2017;

Accepted on: 17/10/2017

---

**Abstract:** The effect of filler aspect ratio on the dielectric properties of epoxy resin reinforced with carbon black (CB) is here investigated. The composites change from an electrical insulator to a conductor as the CB content is increased from 1.5% to 4.5%, which is called the percolation region. Complex impedance spectra and Bode diagrams of these composites were carefully analyzed and the corresponding equivalent circuits (EC) under different concentrations of CB were also provided. Furthermore, the correlation between the shape of Bode diagrams and the equivalent circuits was discussed. Finally, the Cole–Cole representation was used to interpret the impedance spectra of all the samples.

**Keywords:** Carbon black, Percolation, Complex impedance, Bode diagram, Cole-Cole.

## Introduction

Dielectric properties of composites have been the focus point of extensive studies during the last decades [1]. This general interest in the dielectric properties of these composites is due to both interesting features of the electricity flow through these composites and wide range of applications in many fields, such as thermistors, electrical screening materials, self-limited electrical heaters and so forth in industry [2–4]. One of the most important studied composites of this type is carbon black (CB) polymer composite [5]. Electrical properties of CB polymer composites can be remarkably enhanced with small CB concentrations. Epoxy/carbon black (epoxy/CB) system is one of the widely used organic/reinforcing filler composites [6–8]. Epoxy resins have high strength, good stiffness, excellent heat, good thermal stability and chemical resistance; therefore, they are applied in the field of coatings, adhesives, casting,

composites, laminates and encapsulation of semiconductor devices [9–12]. However, the development of polymers with high electrical conductivity has opened up the possibility of new applications for polymers [13].

In this paper, we report on the dielectric properties of the dispersion of CB particles in epoxy polymer composites. In order to study the influence of the volume fraction of CB on the dielectric properties of these materials, the impedance spectra of the epoxy/CB composites for different CB concentrations, below and above the threshold concentration, are measured by plotting the complex impedance spectra, the corresponding equivalent circuits and Bode diagrams and also by drawing the Cole–Cole plots of the imaginary part and real part of the impedance of each sample.

## Experimental

The samples investigated in this study consist of small carbon black particles (produced by Cabot Co.) embedded in an insulating epoxy matrix DGEBF: Diglycidyl Ether of Bisphenol F (from Ciba Geigy Co.). The mixture of CB particles and DGEBF was processed with an amine curing agent (diaminodiphenyl-sulfone; DDS). The average size of carbon black particles is 11 nm, density 1.89 g.(cm)<sup>-3</sup>, dc conductivity 350 (Ω.m)<sup>-1</sup> and specific surface area 639 m<sup>-2</sup>.g<sup>-1</sup>. The neat DGEBF has a dc conductivity of 1.4 10<sup>-14</sup> (Ω.m)<sup>-1</sup> and a density of 1.19 g.(cm)<sup>-3</sup>. The ratio, by weight, of the mixture of the CB particles and DGEBF to the amine curing agent was adjusted to achieve stoichiometry [14-16]. The mechanical mixing operation that was used to fabricate samples with specific CB volume concentration  $\phi$  has been previously described in detail elsewhere [17-18]. The samples were cured at room temperature for 24 h. The CB loading was varied from 0 to 6.5 %. Impedance spectroscopy measurements were carried out in the frequency range from 180 Hz to 15 MHz, using an Agilent 4294A precision impedance analyzer, in the  $C_p - R_p$  configuration.

## Theoretical Models

Percolation theory defines an insulator-conductor transition and a corresponding threshold of the conductive filler concentration, *via* the percolation model [19-20]:

$$\sigma_{dc} \sim (\phi - \phi_c)^t \text{ for } \phi > \phi_c, \quad (1)$$

where  $\sigma_{dc}$  is the dc conductivity of the composite,  $\phi_c$  is the percolation threshold and  $t$  is the conductivity exponent.

The relaxation phenomenon in materials has been the subject of extensive study [19]. In most cases, the single relaxation time does not describe the dynamic response of the material [20] and several empirical models were used to fit that response. Between them, the Cole-Cole model [21] is frequently used:

$$Z^*(\omega) = (Z' + iZ'') = Z_\infty + \frac{Z_s - Z_\infty}{1 + (i\omega\tau)^\alpha}. \quad (2)$$

In this equation,  $Z'$  and  $Z''$  are the real and imaginary parts of the complex impedance ( $Z^*$ ), respectively.  $Z_s$  and  $Z_\infty$  are the high and low frequency resistance, respectively,  $\tau$  is the relaxation time,  $\alpha$  is empirical exponent and  $\omega$  is angular frequency ( $\omega = 2\pi f$ ,  $f$  is frequency).

CPE is the abbreviation of 'constant phase element' in electromagnetics. A constant phase element is an equivalent circuit component that describes the behaviour of a double layer, which is an imperfect capacitor. The impedance module of a CPE can be calculated by the following equation [22]:

$$|Z_{CPE}| = \sqrt{(Z')^2 + (Z'')^2} = \omega^{-N} / A \quad (3)$$

$$\varphi = \tan^{-1} (Z'' / Z'). \quad (4)$$

The constant phase  $\varphi$  is always  $-(90 \times N)^\circ$ , with  $N$  from 0 to 1 and  $A$  is a real parameter expressed in  $F.s^{(N-1)}$ . The case  $N = 1$  describes an ideal capacitor, while the case  $N = 0$  describes a pure resistor [23]. When the value of  $N$  is between 0 and 1, then it describes a constant phase element.

## Results and Discussion

### DC Electrical Conductivity

The evolution of conductivity as a function of CB concentration is shown in Fig. 1 for the epoxy/CB composites under study. At low filler concentrations, the gap between CB aggregates, where the electrons are transmitted, is very large and the conductivity of the composites is approximately that of the insulating matrix. As the concentration of conductive fillers rises, a critical concentration is reached, where the conductivity starts to increase abruptly from 1.5% to 4.5%, which is called the percolation region. By using a least-square fit (see the inset of Fig. 1), we found the value of the percolation threshold  $\phi_c = 2.75$  % and the critical conductivity exponent  $t = 1.89$  *via* Eq. (1). The value obtained of the exponent  $t$  is slightly smaller than the universal value of three-dimensional percolating systems that is equal to 2 [24].

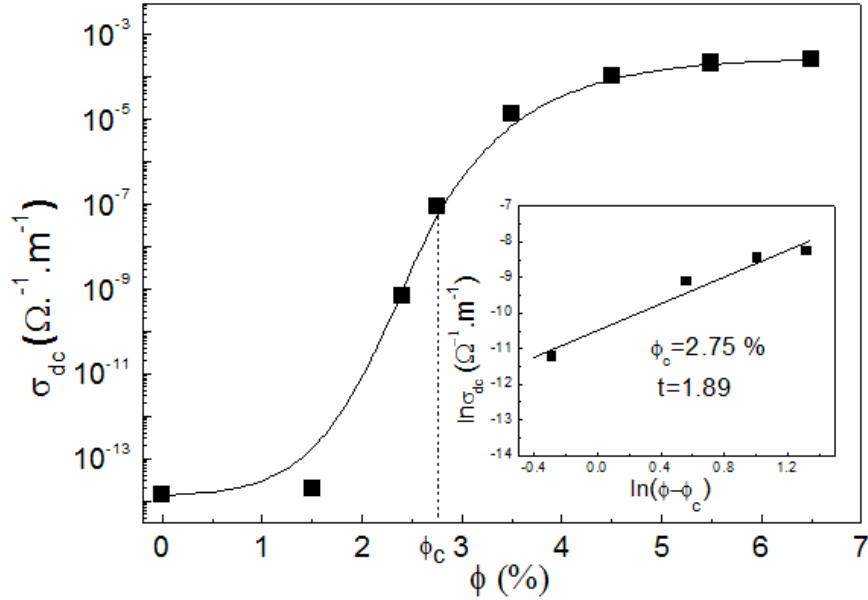


FIG. 1. Variation in dc conductivity ( $\sigma_{dc}$ ) with filler loading in CB.

### Impedance Spectroscopy Properties

The frequency dependence of the impedance modulus,  $|Z|$  and the impedance phase,  $\varphi$ , for different CB concentrations below and above  $\phi_c$  are presented in Figs. 2 and 3 with the frequency changing from 180 Hz to 15 MHz. Below  $\phi_c$ , as can be seen from Figs. 2 and 3,  $|Z|$  is a straight line with a negative slope coefficient and  $\varphi$  is nearly constant (near to, but less than  $-90^\circ$ ). Above  $\phi_c$ , the impedance modulus curves may be divided into two distinct regions (Fig. 2): at low frequencies,  $|Z|$  is frequency independent, which suggests that the ohmic resistance plays an important role, while the capacitive effects can be neglected [25]. With increasing frequency further, the impedance decreases, which defines the character of an R-C network. Similar behaviour has been reported in our previous work [26]. It is obvious from Fig. 3 that for  $\phi > \phi_c$ , the phase angle increases with frequency and approaches  $-90^\circ$  (capacitive dominated) at high frequency region.

Nyquist ( $Z''$  vs.  $Z'$ ) plot of 1.5 % of CB composites and corresponding  $|Z|$  and  $\varphi$  are shown in Fig. 4-a and Fig. 4-b. As can be seen from Fig. 4-a, the complex impedance

spectrum is a straight line, suggesting that at low CB concentration the response is purely capacitive and the dielectric properties of the polymer dominate the composite dielectrical characteristics. As shown in Fig. 4-b,  $\varphi$  is nearly constant (close to  $-90^\circ$ ) and  $|Z|$  is a straight line with a negative slope coefficient. So, the equivalent circuit can be described by a CPE (see Section: Theoretical Models) as shown in the inset of Fig. 4-a. Replacing  $\omega$  with  $2\pi f$  in Eq. (3) and then taking the logarithm on both sides of the equation, we obtain:  $\log|Z| = \log|Z_{CPE}| = -N \log f + \log \frac{1}{(2\pi)^N A}$ . Obviously, the plot should be a straight line with a slope coefficient of  $-N$ , which is in line with the experimental results illustrated in Fig. 4-b. We make the linear fit based on the experimental data at 1.5% CB. As can be seen, the experimental data strongly agreed with the fit result and the slope of this straight line equals  $-0.96$  (in the inset of Fig. 4-b). Table 1 summarizes the obtained fitting parameters  $N$  and  $A$  for all concentrations below  $\phi_c$ . One can clearly see that the values of  $N$  decrease with increasing concentrations of CB, in contrary to the parameter  $A$  which increases considerably with CB.

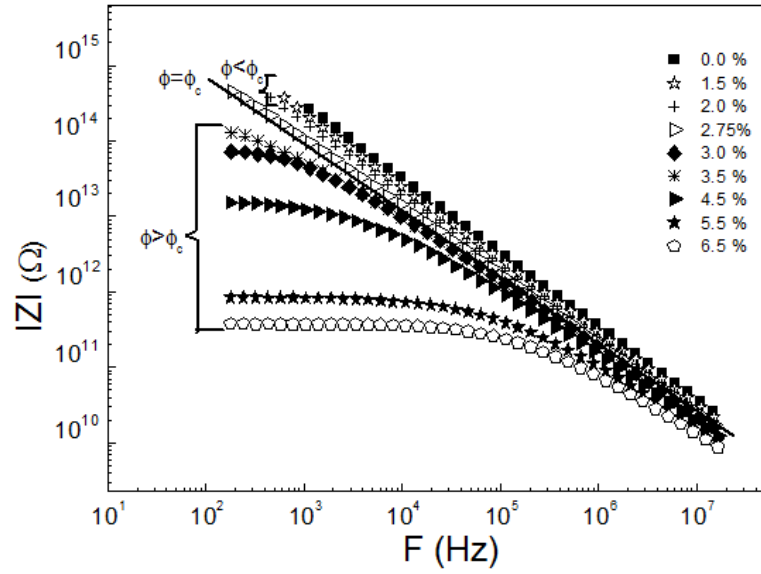


FIG. 2. Frequency dependence of the impedance modulus,  $|Z|$ , of epoxy/CB composites, for concentrations below and above  $\phi_c$ .

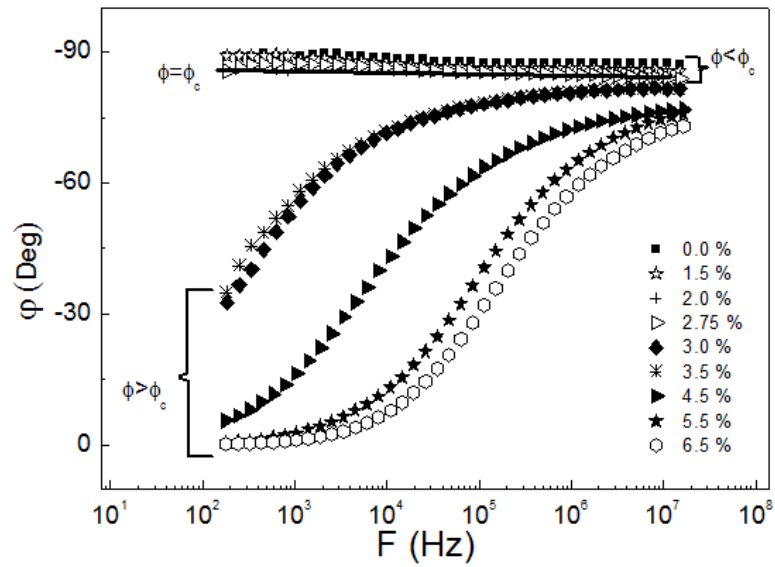


FIG. 3. Frequency dependence of the impedance phase ( $\phi$ ) of epoxy/CB composites, for concentrations below and above  $\phi_c$ .



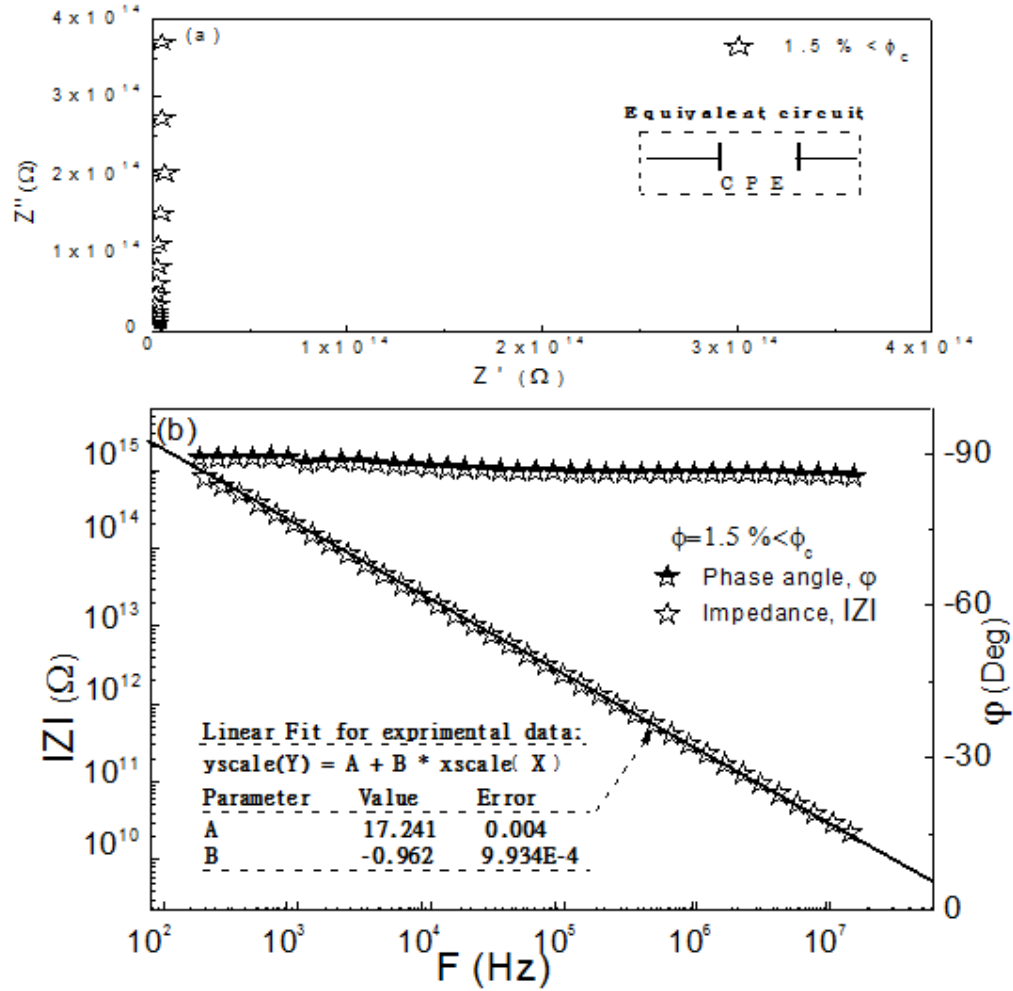

 Fig. 4. (a)  $Z''$  vs.  $Z'$  curve and (b) corresponding  $|Z|$  and  $\phi$  of epoxy/CB at 1.5 % of CB.

 TABLE 1. Fitting parameters  $A$  and  $N$  using the CPE circuit for different CB concentrations below  $\phi_c$ .

$\phi$ (%)	0.0	1.5	2.0	2.75
$N$	0.98	0.96	0.95	0.90
$A * (10^{-17})$ $F. S^{(N-1)}$	2.36	3.32	4.62	9.55

At high CB concentration of (5.5%), the shape of the complex impedance spectrum is a semicircle as shown in Fig. 5-a. The complex impedance spectrum at 5.5% CB can be characterized by an equivalent circuit including a resistor (R) and a capacitor (C) connected in parallel as shown in the inset of Fig. 5-a. Fig. 5-b displays  $|Z|$  and  $\phi$  at this high concentration. It is clear that  $\phi$  increases with frequency and approaches  $-90^\circ$  at high frequency region. This could simply be deduced from the following phase angle

equation for the above mentioned equivalent circuit:  $\phi = \tan^{-1}(\omega RC)$ . As can be seen in this equation,  $\phi$  increase with frequency and when the frequency tends to infinity, the phase angle must get closer to  $-90^\circ$ , which is fully consistent with the results of the experiment. The modulus can be divided into two parts by lines as shown in Fig. 5-b. We make tangents of the first and the second part of the curve, then the two tangents intersect at point  $f_c$ , where the corresponding frequency was near 63 kHz. This frequency is compatible with the

characteristic frequency in Nyquist plot shown in Fig. 5-a. The obtained fitting parameters are presented in Table 2. This table shows that the parameter  $N$  varies between 0.89 and 0.77 and  $A$  increases considerably with CB. On the other

hand, the last column of this table presents the estimated values of the critical frequency. We note that this critical frequency increases with increasing concentrations of CB.

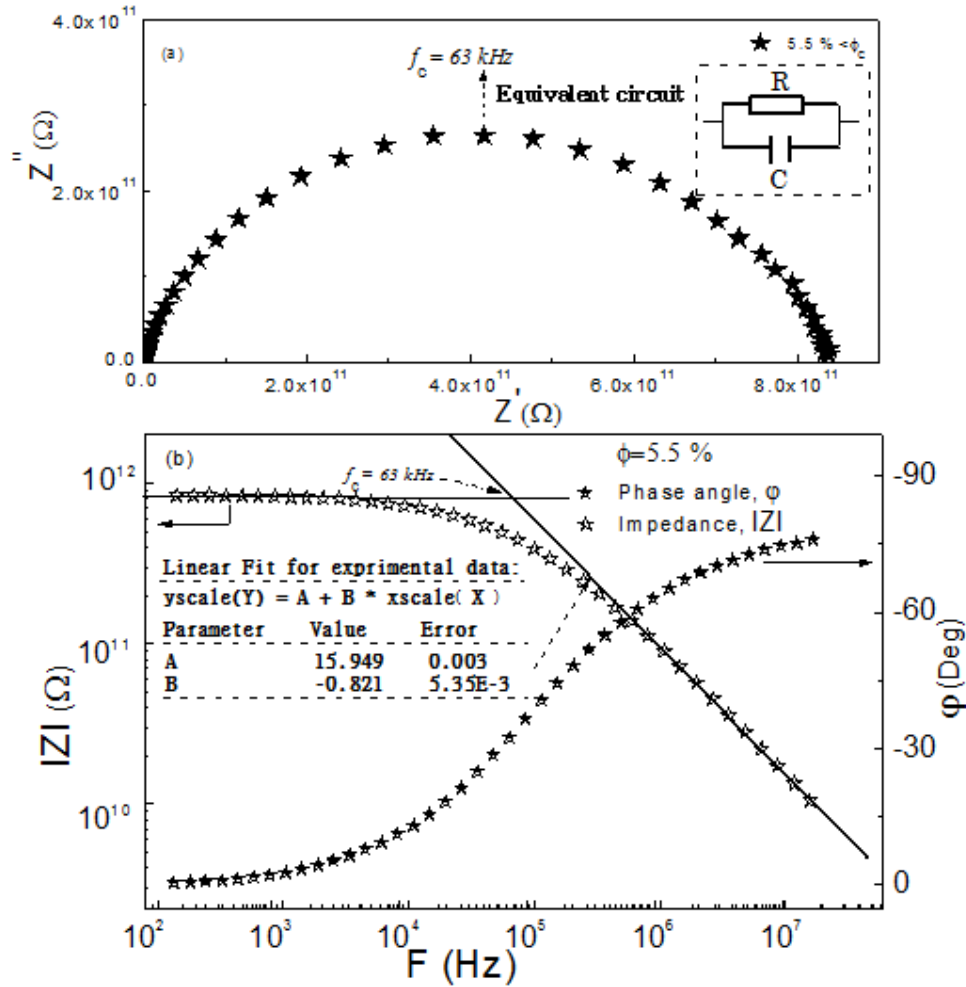


FIG. 5. (a)  $Z''$  vs.  $Z'$  curve and (b) corresponding  $|Z|$  and  $\phi$  of epoxy/CB at 5.5 % of CB.

TABLE 2. Fitting parameters  $A$ ,  $N$  and  $f_c$  using the CPE circuit for different CB concentrations above  $\phi_c$ .

$\phi$ (%)	3.0	3.5	4.5	5.5	6.5
$N$	0.89	0.88	0.87	0.82	0.77
$A \cdot (10^{-17})$ $F.S^{(N-1)}$	1.53	1.46	2.00	5.08	11.90
$f_c$ (kHz)	1.20	1.60	3.00	63.00	1140

In order to obtain more detailed information on these composites prepared herein, we used the Cole-Cole representation, as depicted in Fig. 6 for different concentrations of CB. We have analyzed the data with the Cole-Cole function [23], Eq. (2). For determining the parameters  $\tau$  and  $\alpha$ , we first calculated the approximate values from the asymptotic part of the data, then used them as starting values in a non-linear curve fitting algorithm [27]. When  $\alpha$  is close to 0, the material is more homogeneous, the dipole interaction is low and the semicircle is practically centered in the  $Z'$  axis. For pure epoxy and low CB concentrations, the response is purely capacitive and therefore no semicircle is observed (Fig. 6-a). From Figs. 6-b, c and d, it can be observed that as CB is added to the epoxy matrix, the introduction of the real component to the impedance leads to the

formation of a semi-circle [28]. This semicircle decreases in diameter as the CB concentration increases, which is indicative of the lowering in the electrical resistivity of the composite due to the presence of conduction paths [29]. Indeed, the material is characterized by the formation of an infinite cluster of CB, which allows the displacement of electrons through large distances of the sample. It can also be seen from Table 3 that the strength of resistance,  $Z_s - Z_\infty$ , decreases with CB concentration, indicating the increase in electrical conductivity. The calculated values of  $\alpha$  between 0.216 and 0.419 are responsible for the depressed semicircle in impedance plane, which indicates an increase in heterogeneity with the concentration of the conducting particles [30].

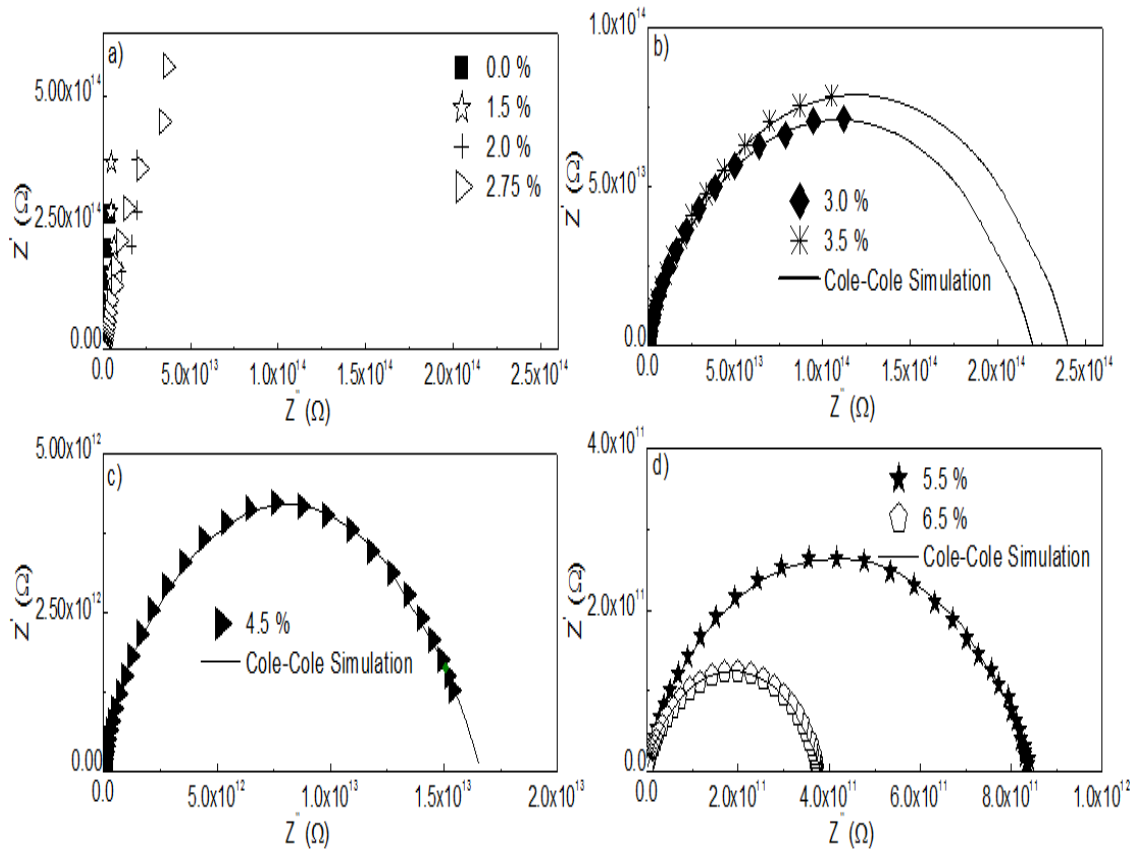


FIG. 6. Cole-Cole plot for different concentrations of CB below and above  $\phi_c$ .

TABLE 3. Dielectric relaxation parameters obtained by simulation of the Cole-Cole equation at different CB concentrations above  $\phi_c$ .

$\phi$ (%)	$(Z_s - Z_\infty) (\Omega)$	$\tau (s^{-1})$	$\alpha$
3.0	$2.20 \cdot 10^{14}$	$12.10 \cdot 10^{-4}$	0.27
3.5	$2.40 \cdot 10^{14}$	$9.90 \cdot 10^{-4}$	0.26
4.5	$16.64 \cdot 10^{12}$	$4.70 \cdot 10^{-5}$	0.42
5.5	$0.85 \cdot 10^{12}$	$2.28 \cdot 10^{-6}$	0.30
6.5	$0.38 \cdot 10^{12}$	$1.42 \cdot 10^{-6}$	0.26

## Conclusion

In summary, the influence of the volume fraction of CB on the dielectric properties of epoxy/CB composites was studied. It was found that these composites change from an electrical insulator to a conductor as the CB content is increased from 1.5% to 4.5%, which is linked to the percolation region. Complex impedance

spectra and Bode diagrams of these composites were carefully analyzed and the corresponding equivalent circuits were also provided. At the end, the Cole–Cole representation was used to interpret the impedance spectra of all the samples.

## References

- [1] Sichenko, M.B., *Rev. Mod. Phys.*, 64 (1992) 961.
- [2] Klason, K. and Kubat, J., *Int. J. Polym. Mater.*, 10 (1984) 259.
- [3] Miyasaka, K., Watanabe, K., Yogima, E., Aida, H., Sumita, M. and Ishikawa, K., *J. Mater. Sci.*, 17 (1982) 1610.
- [4] Gardiner, K., Calvert, I.A., van Tongeren, M.J.A. and Harrington, J.M., *Ann. Occup. Hyg.*, 40 (1996) 65.
- [5] Sichel, E.K., Gittleman, J.I. and Sheng, P., *Journal of Electronic Materials*, 11(4) (1982) 699.
- [6] Hosaka, H., Ohnabe, H. and Saikawa, T., *Proc. Yonezawa Conference, Tohoku Branch, (JSME), Japan, (1999) 13.*
- [7] El- Tantawy, F. and Deghaidy, F.S., *Polym. Int.*, 49 (2000) 1371.
- [8] Park, D.M., Hong, W.H., Kim, S.G. and Kim, H.J., *Eur. Polym. J.*, 36 (2000) 2429.
- [9] El-Tantawy, F. and Deghaidy, F.S., *Polym. Int.*, 49 (2000) 1371.
- [10] Park, D.M. and Hi, H.W., *Eur. Polym. J.*, 36 (2000) 2429.
- [11] Kang, S., Hong, S., Choe, C.R., Park, M., Rim, S. and Kim, J., *Polymer*, 42 (2001) 879.
- [12] Punchaipetch, P., Ambrogi, V., Giamberini, M., Brostow, W., Carfagna, C. and D'Souza, N.A., *Polymer*, 42(5) (2001) 2067.
- [13] Wilson, A. and De Paoli, M., *Eur. Polym. J.*, 35 (1999) 35.
- [14] Essone Mezeme, M., El-Bouazzaoui, S., Achour, M.E. and Brosseau, C., *J. Appl. Phys.*, 074107 (2011) 109.
- [15] Brosseau, C. and Achour, M.E., *J. Appl. Phys.*, 124102 (2009) 105.
- [16] El-Bouazzaoui, S., Droussi A., Achour, M.E. and Brosseau, C., *J. Appl. Phys.*, 104107 (2009) 106.
- [17] Achour, M.E., El-Malhi, M. and Carmona, F., *J. Appl. Polym. Sci.*, 61 (1996) 2009.
- [18] Achour, M.E., El-Malhi, M., Miane, J.L., Carmona, F. and Lahjomri, F., *J. Appl. Polym. Sci.*, 73 (1999) 969 3.
- [19] Feldman, Y, Gusev, Y.A. and Vasilyeva, M.A., *Tutorial, Kazan Federal University, Institute of Physics (2012) 134.*
- [20] Frohlich, H., "Theory of dielectrics: Dielectric constant and dielectric loss (Monographs on the physics and chemistry of materials)", (Clarendon Press Oxford, 1958) 192.

- [21] Samir, Z., El-Merabet, Y., Graça, M.P.F., Teixeira, S.S., Achour, M.E. and Costa, L.C., *Compos. Mater.*, 51(13) (2016) 1831.
- [22] Macdonald, J.R. and Johanson, W.B., "Theory in Impedance Spectroscopy", (John Wiley & Sons, New York, 1987).
- [23] Diard, J.P., Gorrec, B.L. and Montella, C., *J. Electroanal. Chem.*, 471 (1999) 126.
- [24] Zen, J.M., Ilangoan, G. and Jou, J.J., *Anal. Chem.*, 71 (1999) 2797.
- [25] Grimaldi, C. and Balberg, I., *Phys. Rev. Lett.*, 96(14) (2006) 066602.
- [26] Vivo, B.D., Lamberti, P., Spinelli, G., Tucci, V., Guadagno, L. and Raimondo, M., *J. Appl. Phys.*, 118 (2015) 064302.
- [27] Costa, L.C. and Mendiratta, S.J., *Non-Cryst. Sol.*, 172–174 (1994) 1324.
- [28] Bowen, C.R., Buschhorn, S. and Adamaki, V., *Pure Appl. Chem.*, 86 (2014) 765.
- [29] Shrivastava, N.K., Maiti, S., Suin, S. and Khatua, B.B., *Express Polym. Lett.*, 8 (2014) 15.
- [30] Costa, L.C., Achour, M.E., Graça, M.P.F., El-Hasnaoui, M., Outzourhit, A. and Oueriagli, A., *Non-Cryst. Solids*, 356 (2010) 270.



### Advancing Nuclear Astrophysics Using Next-Generation Facilities and Devices

C. Langer<sup>a</sup>, N. Klapper<sup>a</sup>, C. Köppchen<sup>a</sup>, S. Dababneh<sup>b</sup> and R. Reifarth<sup>a</sup>

<sup>a</sup> Goethe University Frankfurt, Frankfurt, Germany.

<sup>b</sup> Department of Physics, Faculty of Science, Al-Balqa Applied University, Salt, Jordan.

---

Received on: 23/8/2017;

Accepted on: 18/12/2017

---

**Abstract:** Where are all the heavy elements formed? How are they formed? What is the role played by stars and stellar explosions?

Nuclear astrophysics aims at answering these fundamental scientific questions by linking nuclear physics with astrophysical modelling and observations. Large progress has been achieved in past decades. However, new nuclear physics facilities and devices are urgently required to advance research into regions of the nuclear chart so far not reachable. This will enable unprecedented studies of nuclear reactions in the laboratories, which are key for heavy element synthesis and the fate of a star. Some highlights of upgrade-in-process will be described.

Experimental effort needs to be guided by astrophysical modelling to find significant uncertainties and pinpoint important measurements to be carried out. For two astrophysical scenarios, sensitivity studies using detailed nuclear network calculations will be presented. These calculations involve charge-particle induced reactions like  $(p,\gamma)$  or  $(\alpha,\gamma)$  during the rapid proton capture process (rp process). On the other hand, core-collapse supernovae can be studied using rare presolar type C SiC grains. Observed peculiar abundance distributions in these grains can be explained with the conditions during the nucleosynthesis. We therefore study the light mass Si-S region by variations of  $(n,\gamma)$  reaction rates. Also, the influence of different neutron pulses and the effect on the final abundances of the production of the important radioisotope  $^{32}\text{Si}$  are examined.

Both investigations stress the need for enhanced experimental approaches to measure reaction rates to better constrain the astrophysical sites.

**Keywords:** Nuclear astrophysics, Presolar grains, Nuclear physics, Facilities, Network calculations.

## Introduction

Nuclear reactions play a dominant role for the energy generation of stars. Fusion reactions during the hydrostatic evolutionary phases of a star lead to a partial creation of heavy chemical elements up to iron-like elements [1,2].

Elements beyond iron must be produced in other processes. In a ground-breaking publication [3], the authors describe several processes involving particle captures on existing seed nuclei for creating the heaviest observed

elements. Up to now, our understanding is still based on the same idea: all heavy elements must be created in stars and stellar explosions. However, the fine details of the different production mechanisms have been shaped and changed over the past 50 years and it seems that the grand picture is settled, see e.g. [4–8].

To create heavy elements, several distinct processes act in our surrounding universe, like the slow and rapid neutron capture processes (s-

and r-process) at different stellar sites. Input from nuclear physics, like cross-sections, reaction rates, masses, binding energies, half-lives and others, are key for understanding the details of these production mechanisms. For stable or close-to-stable isotopes, many of the required properties have been determined and can be used in astrophysical modelling and galactical chemical evolution calculations [9].

However, several heavy element production processes involve highly radioactive isotopes far off the valley of stability. To study them experimentally, special radioactive science facilities are required for production of short-lived isotopes as a beam. It is then possible to examine relevant astrophysical reactions; however, many measurements still need to be carried out and are urgently required for advancing astrophysical calculation. Currently, the limitation of existing facilities is reached and further progress is hampered. Therefore, major upgrades are foreseen at several facilities all over the world.

To guide upcoming experiments towards the important, so far inaccessible, reactions, detailed astrophysical and nuclear calculations are required. Nuclear network calculations can be used to better understand abundance flows and uncertainties in input parameters, like reaction rates and masses, and disentangle them from thermodynamic effects imposed by the specific astrophysical environment.

The next section of this article will shortly motivate the need for new and upgraded facilities and devices. All the experimental effort should be guided by comprehensive astrophysical calculations. Therefore, detailed network calculations for the rapid proton capture process on neutron stars are shown. Also, the influence of uncertain reaction rates on a recently discovered peculiarity in the expected abundance distribution extracted from presolar SiC grains will be discussed and first preliminary results will be shown. This potentially leads to a better understanding of core-collapse supernovae and their contribution to the formation of SiC grains.

## Future Facilities and Devices

Major upgrades are foreseen at current facilities. The focus is on producing more exotic isotopes at higher intensities and better quality. This will finally enable experimental studies

involving the very short-lived isotopes relevant for stellar modelling, which, in turn, will also lead to a highly-increased understanding of the details of how a nucleus arranges and what the underlying forces are. This is complemented by very active research in nuclear theory and a constant increase in computer power, which in turn enables calculations from first principles even for heavier isotopes, see e.g. [10].

A good overview of ongoing upgrades and future facilities can be found e.g. here [11–23].

Besides establishing upgraded beam facilities, major effort is also put into the development of new equipment and devices relevant for nuclear astrophysics. Next-generation setups, like e.g. the  $R^3B$  setup [24,25] and CRYRING at FAIR [26], as well as SECAR [27] and the high-rigidity spectrometer at FRIB [28], are extremely important tools for studying processes significant in nuclear astrophysics. They will allow for a multitude of different reaction studies with which key properties, like reaction rates and masses, can be extracted, even with lowest intensity beams.

Also, new devices will unfold their full potential once the desired upgrades are successfully completed. As an example, it has been shown recently that  $\gamma$ -ray detection devices, like GRETA [29,30] (similar to AGATA [31]) are very powerful instruments for studies related to nuclear astrophysics [32–36]. Using them in conjunction with a magnetic spectrometer and a radioactive beam facility, nuclear structure properties can be extracted, that are in turn sensitively entering the reaction rates.

## Network Calculations

Performing nuclear reaction experiments is typically a very tedious task and employs a lot of effort and manpower. Therefore, ideally, (future) experiments performed for nuclear astrophysics should be guided by detailed astrophysical calculations estimating the impact of a certain reaction in a specific astrophysical environment.

In this sense, nuclear reaction network calculations represent a powerful tool. Here, the interaction of several isotopes connected through corresponding reactions, like  $(p,\gamma)$  or  $(n,\gamma)$ , as well as weak decays, like  $\beta$ -decays, can be studied in terms of energy generation, abundance formation and other interesting properties. This typically includes solving coupled differential



equations and requires special tools to handle the (huge) amount of processing time. To study the effect induced by nuclear physics, like uncertainties in the reaction rate, these network calculations can be performed using different input parameters. This can then be, in turn, compared to base runs, in which no variations are included. Eventually, the effect of single or multiple uncertainties in a specific network calculation can be assessed.

In the following sections, two examples of preliminary detailed network calculations will be presented related to different astrophysical scenarios. Both estimate the impact of uncertain reaction rates on observables, like X-ray burst light curves and abundance distributions, on presolar SiC grains.

### a. Type I X-ray Bursts

Type I X-ray bursts are thermonuclear explosions ignited in the outer envelope of an accreting neutron star. Because of the constantly rising temperatures and densities during the accretion process, eventually, a thermonuclear runaway might be triggered.

This, in turn, leads to high temperatures up to 2 GK and typical densities of  $10^6$  g/ccm. Depending on the composition of the accreted material, which is typically hydrogen- and helium-rich, fast proton- and alpha-capture reactions are driving the initial light material towards heavier elements, and up to  $A = 100$  can be created in this so-called rapid proton capture process (rp process); i.e., adding more than 50 protons to the initial H/He material [37, 38]. In total, this takes only a few seconds and is typically repeated while the neutron star accretes again material from the companion star.

These explosions can be observed using space-based telescopes as an outburst of the X-ray luminosity with a specific shape of a fast rise and a slow exponential-like decay.

It is still an open question whether the produced ashes of the explosion enrich the surrounding interstellar medium through mass loss or other mechanisms. It still seems that type I X-ray bursts do not contribute to the observed solar abundance distribution.

Nonetheless, observation of type I X-ray bursts offers unique and exciting insights into nuclear physics under extreme conditions on a neutron star, as well as the behavior of dense

neutron matter; as such, this type of X-ray bursts is deemed to represent a very rich stellar nuclear laboratory, e.g. [39,40].

Extracting astrophysical information from X-ray burst light curves, like accretion rate, composition, millisecond oscillations and others, requires a detailed understanding of the underlying nuclear physics and the reactions among different nuclei. Therefore, the existing uncertainties in key nuclear reactions must be eliminated or at least significantly constrained. In recent sensitivity studies [41–44], the influence of these nuclear physics uncertainties on the light curves and abundance distributions has been studied and evaluated.

### Sensitivity Study

In this study, we focus on the major rp process waiting point  $^{56}\text{Ni}$ . Because of its peculiar properties, it serves as a dominant bottleneck in the rp process. The  $^{56}\text{Ni}$  isotope decays almost exclusively *via* electron capture (EC) decay to  $^{56}\text{Co}$ , since the  $\beta^+$ -decay is blocked. This, however, takes more than  $10^4$  seconds and is as such not possible in typical X-ray burst scenarios. The breakout reaction  $^{56}\text{Ni}(p,\gamma)^{57}\text{Cu}$ , on the other hand, has a relatively low Q value of only 690 keV, which leads to a fast buildup of flow equilibrium between the forward (p, $\gamma$ ) and the reverse ( $\gamma$ ,p) reaction under hot conditions (similar to the r process waiting point picture). Heavier, charged particle-induced reactions are typically hampered by the already high Coulomb barrier.

In a recent study, the influence of the breakout reaction on  $^{57}\text{Cu}$ ; i.e.,  $^{57}\text{Cu}(p,\gamma)^{58}\text{Zn}$ , was studied to understand the reaction flow  $^{56}\text{Ni}(p,\gamma)^{57}\text{Cu}(p,\gamma)^{58}\text{Zn}$  [32]. A second study determined a new  $^{55}\text{Ni}(p,\gamma)^{56}\text{Cu}$  rate, which could lead to a significant bypass of  $^{56}\text{Ni}$ , when enough material is being processed towards  $^{57}\text{Zn}$  [34]. The  $^{56}\text{Ni}(p,\gamma)^{57}\text{Cu}$  rate was already experimentally constrained by Rehm et al. [45].

Here, we study in detail the flow behavior around  $^{56}\text{Ni}$  including several isotopes in the direct vicinity, see FIG. 1(a). This leads to a much better understanding of important and still uncertain reactions, which urgently need to be studied experimentally.

For solving the network equations, the code “xnet” has been used [46] with its input from the current JINA reaclib library [47]. The network is

then solved under fixed temperature and density conditions in the range of typical X-ray bursts. In FIG. 1(b), the  $\beta^+$  decay ratio of  $^{57}\text{Zn}$  for the  $N = 27$  isotonic chain is calculated according to:

$$\beta^+ (^{57}\text{Zn}) = \frac{\beta_{57\text{Zn}}}{\beta_{56\text{Cu}} + \beta_{57\text{Zn}}},$$

with  $\beta_x$  being the partial integrated  $\beta^+$  flows.

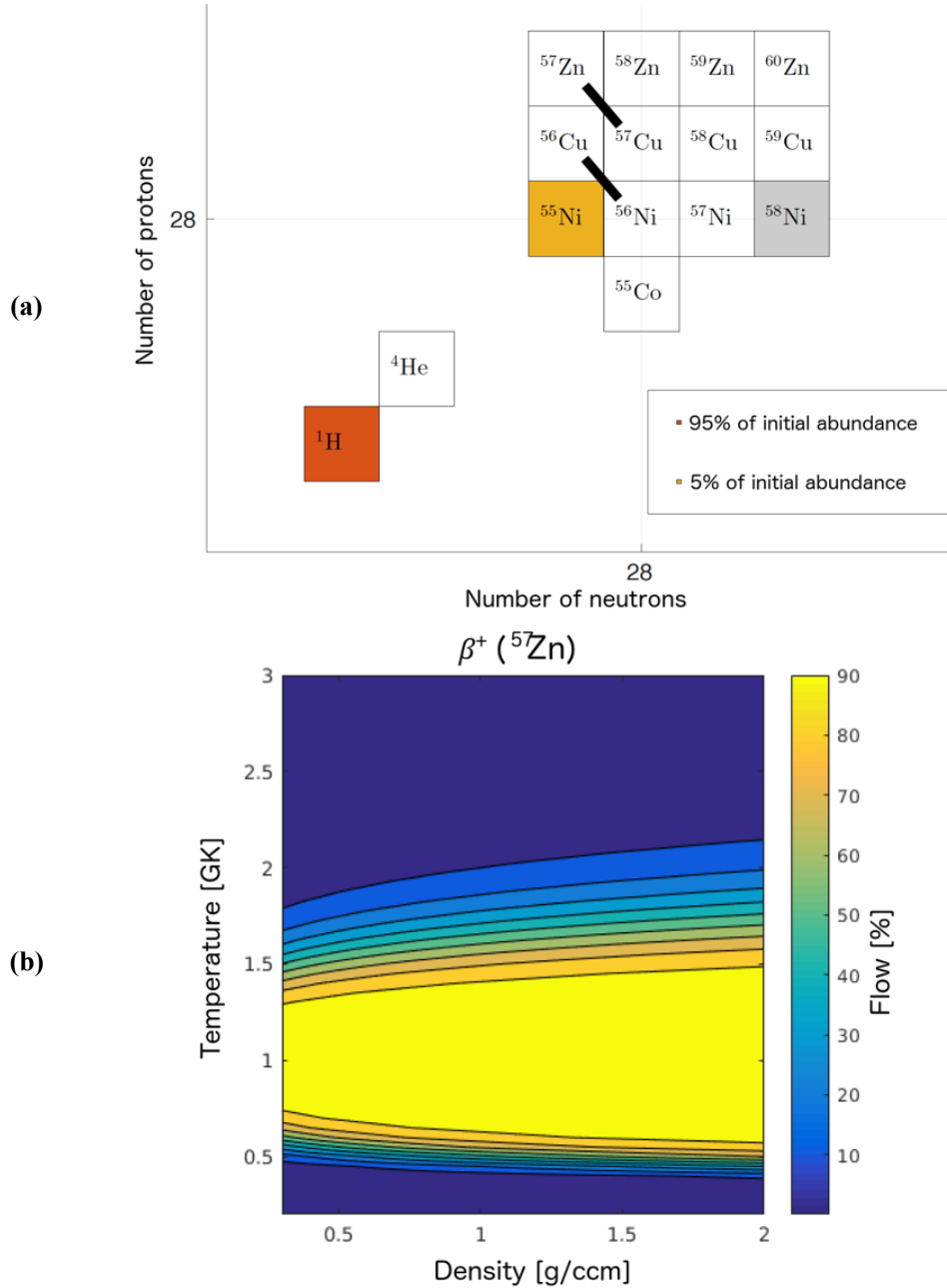


FIG. 1. (a) Small part of the rp process reaction network studied here. It includes nuclides near the major waiting point  $^{56}\text{Ni}$  to the next waiting point  $^{60}\text{Zn}$ . Within this small network, reaction rates, initial abundances, temperatures and densities can be varied and the effect on the flow can be studied. Two example  $\beta^+$  flows are shown. (b) A typical result extracting the amount of leakage out of a certain isotonic chain to the next chain *via*  $\beta^+$  decay. In this case, the decay out of the  $N = 27$  isotonic chain ( $^{56}\text{Cu}$ ,  $^{57}\text{Zn}$ ) into  $N = 28$  is studied. Shown is the amount of flow given by  $\beta^+$  decay of  $^{57}\text{Zn}$  normalized to the total  $\beta^+$  decay flow out of  $N = 27$  in this network. This ratio is calculated for different temperature and density conditions, which are kept constant.

It is obvious that in a certain temperature and density region, more than 50% of the  $\beta$ -decay flow out of  $N = 27$  is determined by the decay of  $^{57}\text{Zn}$ . This can also be clearly seen in the flow pattern in FIG. 2. At a temperature of  $T = 1$  GK

at  $\rho = 10^6$  g/ccm, almost all the flow proceeds through  $^{57}\text{Zn}$ , whereas, according to FIG. 1 and FIG. 2, at 2 GK, less than a few percent proceeds through the  $\beta$ -decay of  $^{57}\text{Zn}$ .

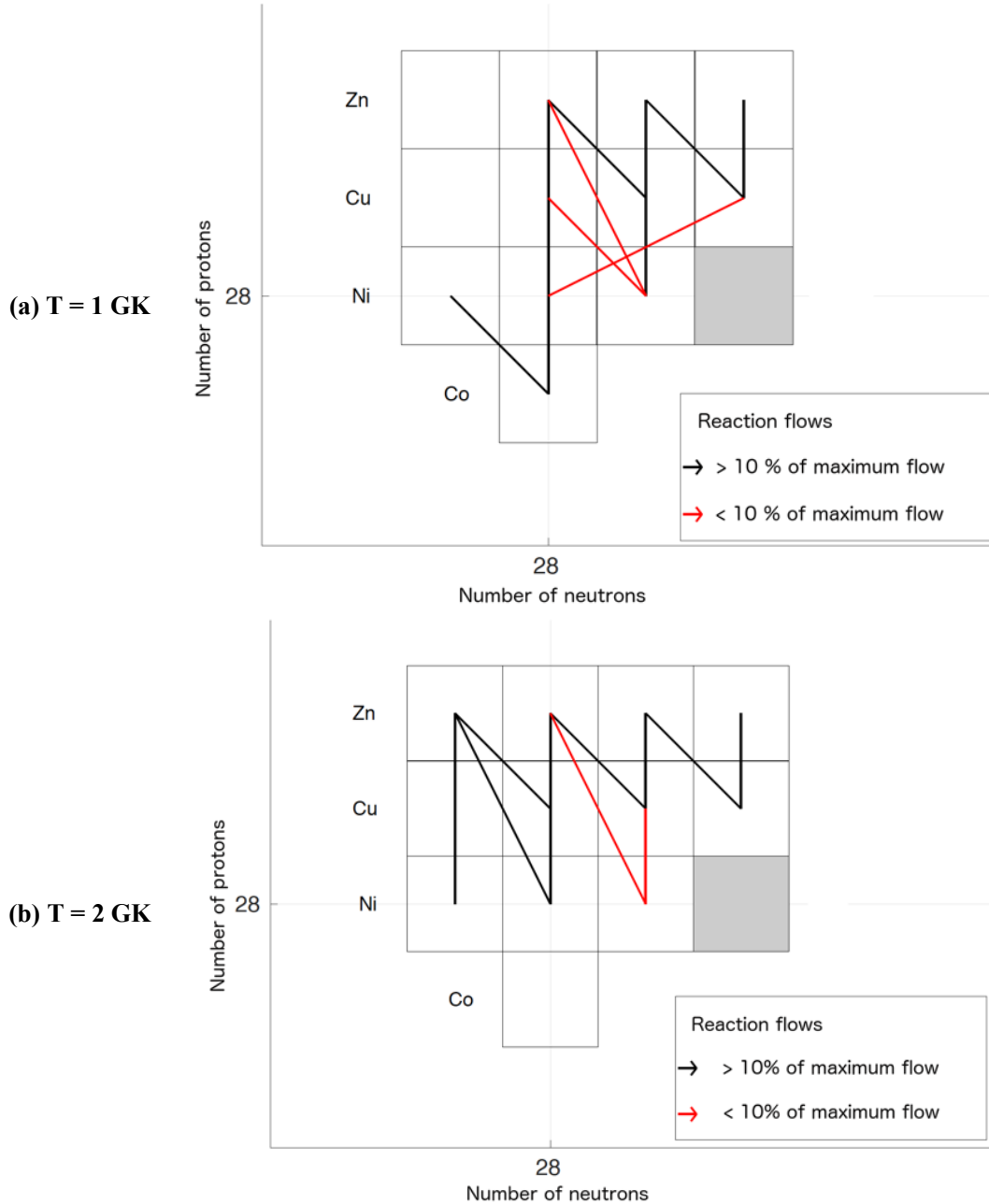


FIG. 2. Detailed calculations to examine the flow of the rp process under different temperatures in the  $^{56}\text{Ni}$  region. For both figures, the density is set to  $10^6$  g/ccm. Black lines show dominant flow (i.e., more than 10% of the total flow) compared to the red lines, which show minor flows (less than 10% of the total flow). Clearly, in (b) at 2 GK, the  $^{56}\text{Ni}(\alpha, p)$  and its reverse reaction  $^{59}\text{Cu}(p, \alpha)$  start to contribute to the reaction flow. Also, the  $\beta$ -delayed proton emission decay is clearly visible under both temperature conditions.

As can also be seen in FIG. 2(b), the  $^{59}\text{Cu}(p, \alpha)^{56}\text{Ni}$  starts to play a role when increasing the temperature. In fact, this reaction

feeds back into  $^{56}\text{Ni}$ , whereas the reverse reaction  $^{56}\text{Ni}(\alpha, p)^{59}\text{Cu}$  is much slower, thus contributing only little to the overall flow, see

FIG. 3(a). This leads to a sensitive temperature-dependence of the flow beyond  $^{56}\text{Ni}$ , eventually trapping all material in  $^{56}\text{Ni}$  at temperatures exceeding 2 GK. As this is barely in accordance

with astronomical observations, temperatures above 2 GK are very unlikely for standard type I X-ray bursts. This again shows the power of these detailed sensitivity studies.

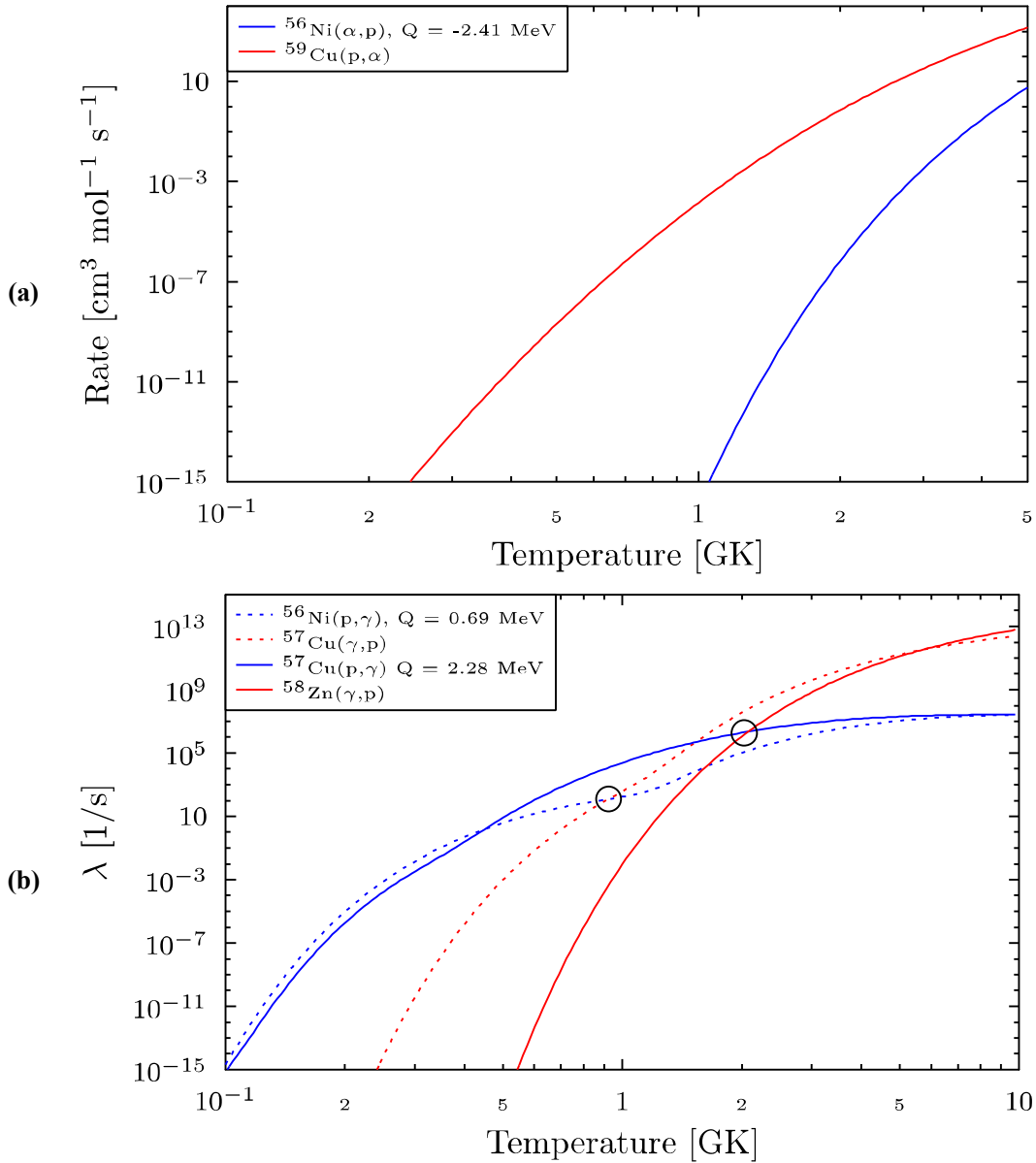


FIG. 3. (a) The  $^{56}\text{Ni}(\alpha, p)$  rate with its reverse rate. As can be seen, the red line; i.e., the  $(p, \alpha)$  reaction, is much faster than the forward  $(\alpha, p)$  reaction (blue line) at typical X-ray burst temperatures. (b) Two different fast  $(p, \gamma)$  reactions (with a density of  $10^6$  g/ccm and a hydrogen mass fraction of 0.7) with the corresponding photodissociation rates. At a certain temperature  $T_{\text{equal}}$ , the photodissociation  $(\gamma, p)$  is getting faster than the forward reaction. This is a function of the  $Q$  value of the reaction (see black circles for different  $Q$  values).

FIG. 3(b) demonstrates thereby an important effect caused by the calculation of the reverse reaction using the detailed balance theorem in the case of a photodissociation reaction involved:

$$\frac{\lambda_{\gamma}}{N_A \langle \sigma v \rangle_{aA \rightarrow \gamma B}} \propto (k_B T)^{3/2} e^{-\frac{Q_{aA \rightarrow \gamma B}}{k_B T}},$$

with  $N_A$  being the Avogadro constant,  $\langle \sigma v \rangle$  being the reaction rate with Maxwellian velocity

distribution,  $k_B$  the Boltzmann constant,  $T$  the temperature and  $Q$  the specific reaction  $Q$  value.

At a certain temperature  $T_{\text{equal}}$ , the reverse and the forward reaction are equally fast, as

shown with circles in FIG. 3(b). This temperature  $T_{\text{equal}}$  depends on the reaction  $Q$  value under same stellar environments.

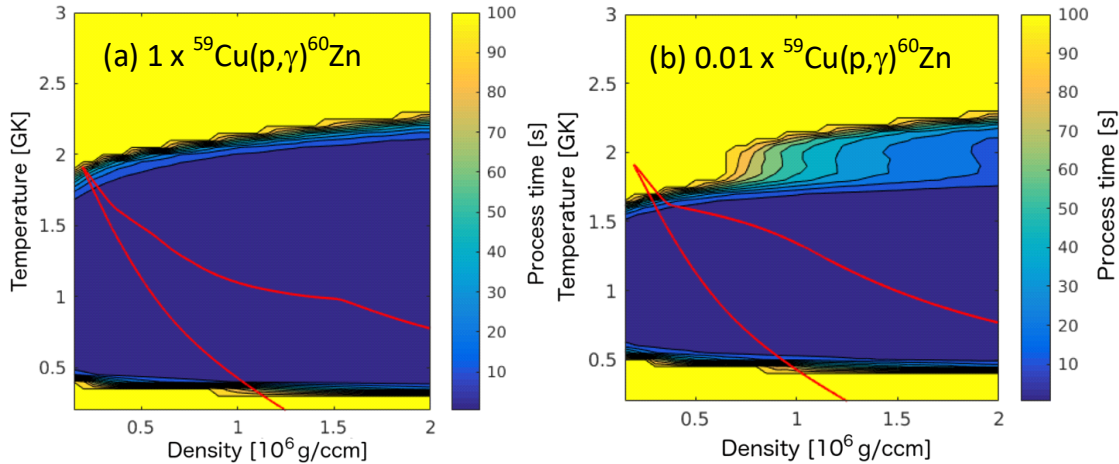


FIG. 4. Sensitivity study when varying one single reaction rate in (b). In this case, the important  $^{59}\text{Cu}(p,\gamma)^{60}\text{Zn}$  reaction rate is varied by a factor of 0.01 from (a) to (b). To define a reasonable figure-of-merit, the processing time; i.e., how long it takes to move a certain fraction of the initial abundance through  $^{56}\text{Ni}$  to  $^{60}\text{Zn}$ , is studied here. This processing time is directly reflected in the main observable; the X-ray luminosity.

Recent sensitivity studies on X-ray bursts are based on a certain thermodynamic profile of the system, calculated in hydrodynamical stellar evolution codes, like KEPLER or others [41–43]. In [41], these self-consistent multizone models are used to calibrate a single zone model, which sensitively depends on the initial thermodynamic conditions (temperature and pressure). As such, the results are biased by the choice of a special code and a unique burst behaviour.

The approach taken here is to keep the sensitivity study as independent as possible from an underlying stellar model. Eventually, different thermodynamic trajectories can be inserted into the results presented here and the effect on different variables can be at least estimated.

An example is shown in FIG. 4. It shows the processing time depending on the density and temperature of the system. The processing time is defined as the time it takes to build up half of the initial abundance at the next waiting point, which is in this case  $^{60}\text{Zn}$ . This processing time is directly influencing the observable light curve.

The  $^{59}\text{Cu}(p,\gamma)$  rate is varied by a factor of 0.01 in FIG. 4(b) and then compared to the base run with no variation shown in FIG. 4(a). Different thermodynamic trajectories can also be seen. Especially at low density and high temperature, a

significant difference between the two cases can be seen. This difference in the processing time is reflected in a significant discrepancy between the predicted light curves with and without variation of  $^{59}\text{Cu}(p,\gamma)$ , as shown in [41]. The study performed here has a clear advantage; once a thermodynamic trajectory is known, (a) the effects on observables can be estimated by overlaying the trajectory with the results shown in FIG. 4, and (b), a detailed explanation of the effect can be provided (e.g. when and at which densities and temperatures this effect would be observed too, or could be neglected).

For the future, this approach needs to be expanded to study the entire rp process and cover more density and temperature ranges. Also, a Monte Carlo variation of single reaction rates can be used to complement the evaluation shown here. This would give more and clearer hints towards important reactions and will anticipate different reaction studies. More preliminary results and details about the technique can be found in [48].

### b. The $^{32}\text{Si}$ Puzzle

Core-collapse supernovae mark the end of the evolution of massive stars and are extremely powerful explosions. They provide conditions, in which heavy element synthesis could take place. Still, our understanding of type II (core-collapse)

supernovae is very limited, although decades of research have been invested, see e.g. [49–51].

The grand picture is settled; however, details on the exact explosion mechanism, the formation of a neutron star from the proto-neutron star, the energy transport and other mechanisms, are still under active debate. Connected to these processes is the question of element synthesis, which severely depends on the formation of a neutron- or proton-rich environment inside the star shortly after the explosion was triggered [52]. However, information from inside the explosion region is very scarce, but provides important imprints of the actual conditions.

Tiny presolar grains offer an extremely interesting, unique and promising way to gain insight into the abundance distribution in certain regions of the star shortly after the explosion was triggered, see e.g. [53–57]. Once the temperatures are sufficiently low, these grains are condensed quite some time after the material was created inside the star. These distinct conditions, under which the material was produced, can be extracted by tracing certain isotope abundances (like e.g.  $^{44}\text{Ti}$ ) and then be connected to a particular stellar site.

A large amount of collected presolar grains is made of the SiC mineral. By far, most of the SiC grains are produced in AGB stars with different metallicities, see e.g. [58–60]. A tiny fraction of SiC grains is formed from core-collapse supernova material. Consequently, these so-called type X and C grains are particularly interesting, since a detailed picture of the interior structure of the progenitor from their abundance distributions can be derived [61,62].

Recently, peculiar isotopic signatures were found in several type C SiC grains in striking disagreement with any existing model [63–65]. They are formed during a core-collapse supernova and are most probably produced at the bottom of the so-called C/Si zone. Some grains show high enrichments in heavy silicon together with light sulfur ( $^{32}\text{S}$ ). These isotopic ratios can not be explained by means of any stellar process, like *ad-hoc* mixing or molecule chemistry. As such, the occurrence of highly enriched  $^{32}\text{S}$  constitutes an open question and is so far not resolved.

A possible solution for this problem might come from nuclear physics; neutron captures onto abundant  $^{28}\text{Si}$  lead to  $^{32}\text{Si}$ , which is a long-

lived radioisotope. With a half-life of roughly 150 years,  $^{32}\text{Si}$  is transformed *via* two  $\beta^-$ -decays to stable  $^{32}\text{S}$ . To achieve sufficient neutron captures along the Si isotopic chain, enough neutrons need to be produced *in situ*. Calculations have shown that the required neutron densities are in the typical range of the so-called n-process in the core-collapse supernova [66–68]. Combined with the overabundant  $^{28}\text{Si}$  at the bottom of the C/Si zone, this explanation of neutron captures leading to  $^{32}\text{Si}$  and then decaying into  $^{32}\text{S}$  appears to be quite robust. Once the details are well understood, this observation will help constrain stellar parameters during the type II supernovae, like neutron density and wind velocity, among others. This makes this case extremely interesting and valuable for supernova research.

However, some of the required neutron capture cross-sections are not well studied and need experimental validation. Especially, as have been shown in [67], the  $^{32}\text{Si}(n,\gamma)$  reaction is uncertain by a factor of 100. This constitutes a serious problem: a  $^{28}\text{Si}/^{32}\text{Si}$  ratio is observed in type C SiC grains, but, however, some of the  $^{32}\text{Si}$  could be pollution picked up before the grain was implanted into the primitive meteorite roughly a year after the production.

### Sensitivity Study

In the sensitivity study presented here, the influence of uncertainties in  $^{31}\text{Si}(n,\gamma)^{32}\text{Si}$ ,  $^{32}\text{Si}(n,\gamma)^{33}\text{Si}$  as well as the impact of different neutron densities on the final  $^{32}\text{Si}/^{28}\text{Si}$  ratio was studied. This resembles the situation *at situ*; i.e., no transport of the grain through different layers is simulated.

In FIG. 5(top), a part of the nuclear reaction network used is shown. The full nuclear network extends up to  $^{56}\text{Mn}$  and consists of neutron capture reactions (n, $\gamma$ ) and corresponding  $\beta^-$ -decays. The network equations are solved using the program NETZ [69].

FIG. 5(bottom) shows the Maxwellian-averaged cross-sections used for  $^{31}\text{Si}(n,\gamma)$  and  $^{32}\text{Si}(n,\gamma)$  [70,71]. Obviously, the neutron capture rate of  $^{31}\text{Si}(n,\gamma)$  is much faster than the subsequent one on  $^{32}\text{Si}$ . This is combined with the much shorter half-life of  $^{31}\text{Si}$  ( $t_{1/2} = 157$  minutes) compared to  $^{32}\text{Si}$  ( $t_{1/2} = 150$  years). In total, this will lead to a much higher sensitivity of the  $^{32}\text{Si}/^{28}\text{Si}$  ratio to uncertainties in the

$^{31}\text{Si}(n,\gamma)$  reaction rate than that induced by the  $^{32}\text{Si}(n,\gamma)$  rate.

In a first step, an adequate integrated neutron flux needs to be defined. In FIG. 6, the effect of several integrated neutron fluxes (measured in 1/mb) on the final amount of  $^{32}\text{Si}$  is studied. Observationally, a ratio of  $^{32}\text{Si}/^{28}\text{Si} \sim 10^{-3}$  has been extracted from the type C SiC grains. To adapt to realistic conditions throughout this study, integrated neutron fluxes should not

exceed 1/mb. In the next step, several different neutron pulse profiles are tested within this approach covering different integrated neutron fluxes in the range given by the vertical lines in FIG. 6. Three typical pulses are shown in FIG. 7. They cover a time-integrated neutron flux from  $(10^{-3}$  to  $10^{-1})$  1/mb, which is expected in these scenarios by triggering the efficient  $^{22}\text{Ne}(\alpha,n)$  neutron source [67].

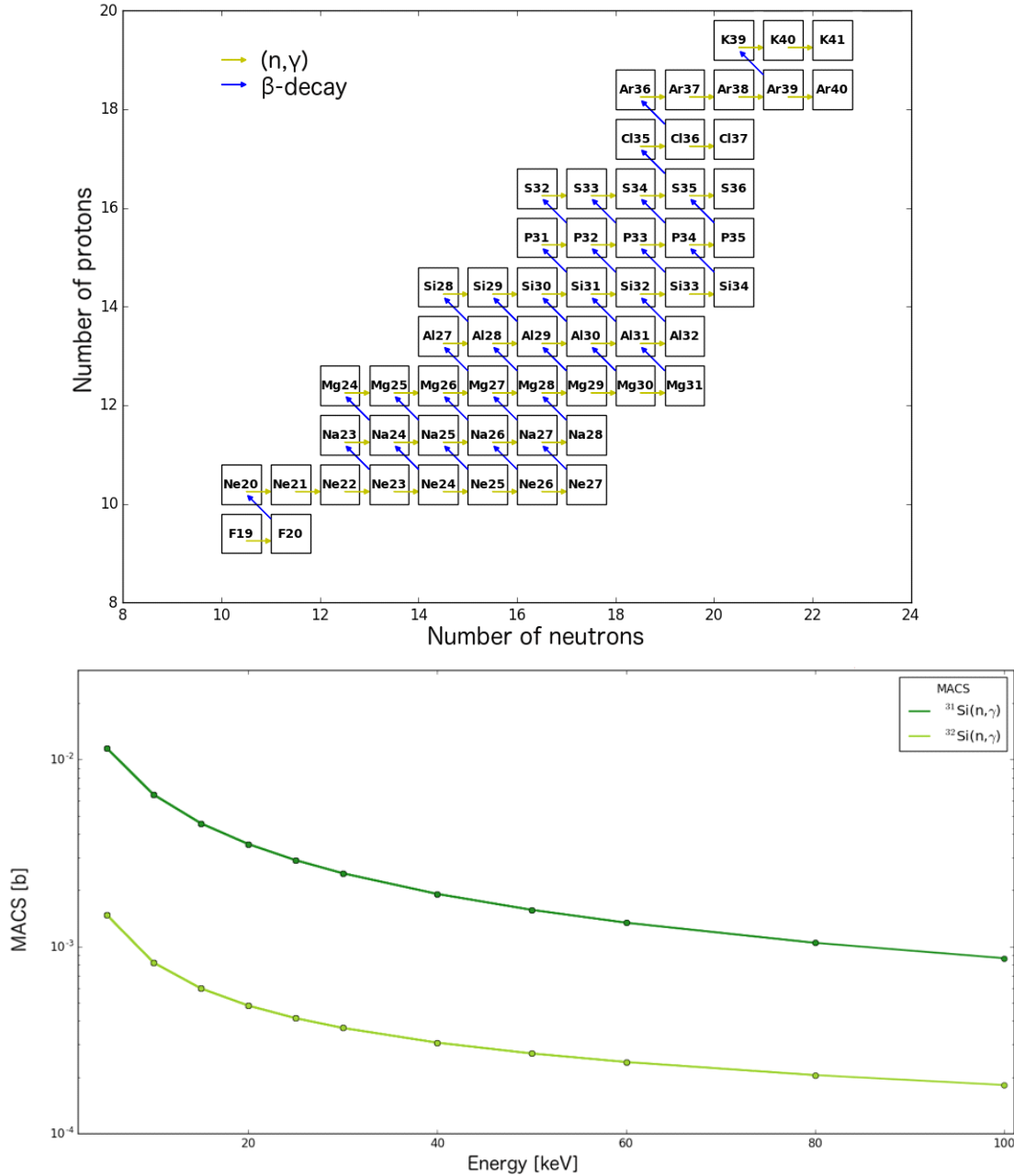


FIG. 5. Part of the network used in this study (top panel). It consists of stable isotopes among a few unstable isotopes. This allows to reconstruct the exact flow path under certain neutron fluxes. The lower panel shows the Maxwellian-averaged cross-sections for  $^{31}\text{Si}(n,\gamma)$  and  $^{32}\text{Si}(n,\gamma)$  used in this study.

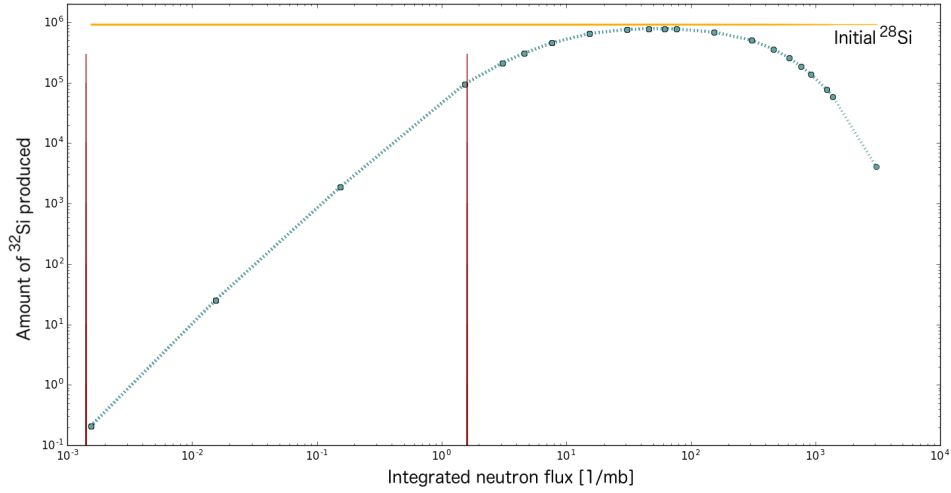


FIG. 6. The effect of different integrated neutron fluxes on the final amount of produced  $^{32}\text{Si}$ . The initial amount of  $^{28}\text{Si}$  used in this network is shown as a horizontal line. As can clearly be seen, at total neutron fluxes exceeding 1/mb, almost all initial  $^{28}\text{Si}$  is transformed into  $^{32}\text{Si}$ , which is unrealistic and can be excluded. At integrated neutron fluxes larger than 100/mb, even heavier Si isotopes are produced ( $^{33}\text{Si}$  and  $^{34}\text{Si}$ ).

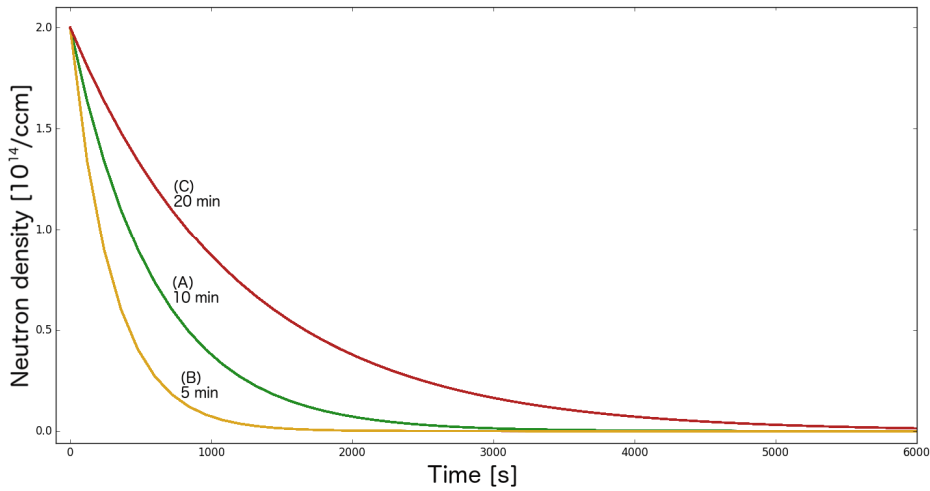


FIG. 7. Three neutron density pulses with a certain characteristic decay time shown next to the lines. Each of the pulses shown here covers a different range of reasonable integrated neutron fluxes.

To assess the effects imposed by uncertainties in the  $^{31}\text{Si}(n,\gamma)$  and  $^{32}\text{Si}(n,\gamma)$  reaction rate on the final  $^{32}\text{Si}/^{28}\text{Si}$  ratio, the rates were varied by a factor of 100 up and down. Moreover, all three neutron pulses A, B and C were used and studied independently.

Here, only the results from pulse A with a decay time of 10 minutes will be presented. However, all other pulses deliver similar results [72]. As can be seen in FIG. 8, the effect of variations in the  $^{31}\text{Si}(n,\gamma)$  rate on the  $^{32}\text{Si}/^{28}\text{Si}$  ratio is huge. It is obvious that the current uncertainty in the  $^{31}\text{Si}(n,\gamma)$  rate is too large to constrain the integrated neutron flux during the type II supernovae explosion.

The situation seems different in the case of variations of  $^{32}\text{Si}(n,\gamma)$ , as shown in FIG. 9. Here, the observed effect on the  $^{32}\text{Si}/^{28}\text{Si}$  ratio appears to be rather small, even negligible at small integrated neutron fluxes. As such,  $^{32}\text{Si}(n,\gamma)$  acts as a bottleneck reaction. It is already slow at the relevant temperatures; an even slower rate does not have any impact on the  $^{32}\text{Si}/^{28}\text{Si}$  ratio, as shown in FIG. 9. The situation is different when increasing the  $^{32}\text{Si}(n,\gamma)$  rate by a certain factor. In FIG. 9, it is obvious that variations of a factor of 100 lead to a small change in the  $^{32}\text{Si}/^{28}\text{Si}$  ratio at certain higher integrated neutron fluxes, which is by far not comparable to the changes induced by variations of  $^{31}\text{Si}(n,\gamma)$ .



This study clearly shows the importance of detailed network calculations. It is evident that the dependence on the  $^{31}\text{Si}(n,\gamma)$  reaction rate is much more severe than the sensitivity to changes in the  $^{32}\text{Si}(n,\gamma)$  rate. However, constraining the  $^{31}\text{Si}(n,\gamma)$  reaction rate is currently only possible using indirect measurements, since the half-life is too short to perform direct  $(n,\gamma)$  experiments. To gain access to this reaction, only indirect techniques, like transfer reactions, Coulomb dissociation [73,74] or others, are applicable.

A typical approach for this problem is to constrain the neighboring reaction rates, like

$^{30}\text{Si}(n,\gamma)$  and  $^{32}\text{Si}(n,\gamma)$ . Since  $^{30}\text{Si}$  is stable, it is possible to produce a target and perform a direct  $(n,\gamma)$  measurement.  $^{32}\text{Si}$  is a radioisotope with a long half-life of roughly 150 years. Since the  $^{32}\text{Si}(n,\gamma)$  cross-section is rather small at stellar energies, a relatively strong experimental neutron source is required. So far, the existing neutron sources are too weak to perform a direct measurement.

Once the neighboring reactions are constrained experimentally, it is possible to calibrate the reaction theory accordingly and to predict the  $^{31}\text{Si}(n,\gamma)$  rate with higher accuracy.

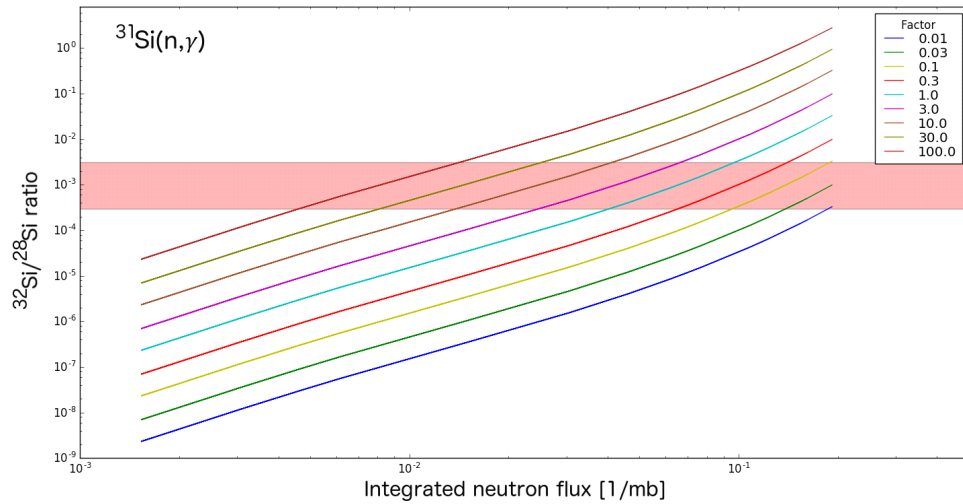


FIG. 8. The  $^{31}\text{Si}(n,\gamma)$  reaction rate varied by different factors. All other reaction rates are kept at their nominal value. A dramatic effect on the produced  $^{32}\text{Si}/^{28}\text{Si}$  can be observed depending on the integrated neutron flux and the variation of the  $^{31}\text{Si}(n,\gamma)$  reaction rate. The horizontal band shows the measured range in SiC grains.

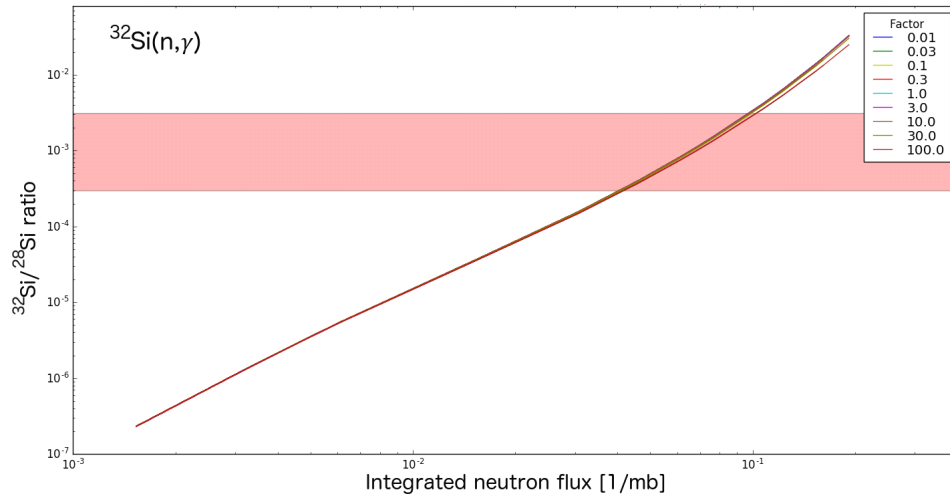


FIG. 9. The effect of variations of  $^{32}\text{Si}(n,\gamma)$  on the  $^{32}\text{Si}/^{28}\text{Si}$  ratio. It is evident that uncertainties in the rate lead to only minor changes in the produced  $^{32}\text{Si}$  abundance over a large range of integrated neutron fluxes. Compared to the changes induced by uncertainties in  $^{31}\text{Si}(n,\gamma)$ , the effects here are negligible. The horizontal band shows the measured range in the SiC grains.

## Conclusion

In this paper, the impact of uncertainties in nuclear reaction rates on two astrophysical processes is examined. In the first case, the rapid proton capture process (rp process) is studied, which powers X-ray bursts on accreting neutron stars. Special emphasis is put on the important  $^{56}\text{Ni}$  waiting point nucleus and reaction rate uncertainties of reactions in the vicinity are studied. Already simple network calculations using constant density and temperature can be used to estimate the impact of existing uncertainties and their effect on the observable of these events; X-ray burst light curves. Furthermore, a method is developed for impact studies independent of the detailed temperature and density evolution of single bursts. As shown,  $^{59}\text{Cu}(p,\gamma)$  appears to be a very important reaction to be studied in the future.

In the second case, the impact of variations of  $^{31}\text{Si}(n,\gamma)$  and  $^{32}\text{Si}(n,\gamma)$  is studied regarding the formation of rare SiC type C presolar grains during core-collapse supernovae explosions. It has been shown that variations in  $^{31}\text{Si}(n,\gamma)$  have a big effect on the final  $^{28}\text{Si}/^{32}\text{Si}$  ratio, which is measured on the SiC grains. Using different example pulses, the detailed effects are investigated and show similar results. The neutron flux, which is created by triggering the  $^{22}\text{Ne}(\alpha,n)$  source during the explosion, leads to efficient neutron captures on abundant  $^{28}\text{Si}$  towards  $^{32}\text{Si}$ , which has a rather long half-life of  $\sim 150$  years and decays after condensation into the SiC grains.

With the advent of upgraded nuclear physics facilities all over the world, these so far inaccessible reaction rates, important for stellar modelling in nuclear astrophysics, can finally be addressed experimentally.

Thereby, it is of utmost importance that these detailed astrophysical and nuclear calculations are used to guide experimental effort. The presented network calculations can be used to reveal important specifics of a certain isotopic region under different temperature and density conditions. Detailed flow extractions and different reasonable thermodynamic trajectories as input parameters are relevant for estimating the impact on the underlying astrophysics in different scenarios and planing future experiments.

At the end, this will lead to efficient usage of already rare and expensive beam time and will help investigate the important open nuclear physics input parameters.

## Acknowledgments

The authors thank Hendrik Schatz and Marco Pignatari for valuable discussions. Saed Dababneh acknowledges support from the Alexander von Humboldt Foundation within the Alexander von Humboldt Professorship award. The authors also thank the organizers of the "Jordanian Life Sciences for Sustainable Development" conference for a pleasant experience and fruitful meeting in Jordan.

## References

- [1] Rolfs, C.E. and Rodney, W.S., "Cauldrons in the Cosmos: Nuclear Astrophysics", (1988).
- [2] Iliadis, C., "Nuclear Physics of Stars", (2015).
- [3] Burbidge, E.M., Burbidge, G.R., Fowler, W.A. and Hoyle, F., *Rev. Mod. Phys.*, 29 (1957) 547.
- [4] Wallerstein, G., Iben, I., Parker, P., Boesgaard, A. et al., *Rev. Mod. Phys.*, 69 (1997) 995.
- [5] José, J. and Iliadis, C., *Reports Prog. Phys.* 74 (2011) 96901.
- [6] Langer, C., *J. Phys. Conf. Ser.*, 503 (2014) 12022.
- [7] Meisel, Z., *J. Phys. Conf. Ser.*, 742 (2016) 12019.
- [8] Reifarth, R., Lederer, C. and Käppeler, F., *J. Phys. G. Nucl. Part. Physics*, 41(5) (2014) 053101.
- [9] Käppeler, F., Gallino, R., Bisterzo, S. and Aoki, W., *Rev. Mod. Phys.*, 83 (2011) 157.
- [10] Hagen, G., Ekstrom, A., Forssen, C., Jansen, G.R. et al., *Nat. Phys.*, 12 (2016) 186.
- [11] Sherrill, B.M. and Gade, A., *Phys. Scr.*, 91 (2016) 53003.
- [12] Gade, A., Gelbke, C.K. and Glasmacher, T., *Nucl. Phys. News*, 24 (2014) 28.
- [13] Wrede, C., *EPJ Web Conf.*, 93 (2015).

- [14] Spiller, P. and Franchetti, G., Nucl. Instruments Methods Phys. Res. Sect. A, Accel. Spectrometers, Detect. Assoc. Equip. 561 (2006) 305.
- [15] Henning, W., AIP Conf. Proc., 773 (2005) 3.
- [16] Reifarh, R., Altstadt, S., Göbel, K., Heftrich, T. et al., J. Phys. Conf. Ser., 665 (2016) 12044.
- [17] Lewitowicz, M., AIP Conf. Proc., 891 (2007) 91.
- [18] Gales, S., Nucl. Phys. A, 834 (2010) 717c.
- [19] Herlert, A. and Kadi, Y., J. Phys. Conf. Ser., 312 (2011) 52010.
- [20] Lindroos, M., Butler, P.A., Huysse, M. and Riisager, K., Nucl. Instruments Methods Phys. Res. Sect. B Beam Interact. with Mater. Atoms, 266 (2008) 4687.
- [21] Ball, G.C., Buchmann, L., Davids, B., Kanungo, R., Ruiz, C. and Svensson, C.E., J. Phys. G. Nucl. Part. Phys., 38 (2011) 24003.
- [22] [https://science.energy.gov/~media/np/nsac/pdf/2015LRP/2015\\_LRPNS\\_091815.pdf](https://science.energy.gov/~media/np/nsac/pdf/2015LRP/2015_LRPNS_091815.pdf), Reaching for the Horizon (2015).
- [23] <http://www.nupec.org/lrp2016/Documents/lrp2017.pdf>, Perspectives for Nuclear Physics (2017).
- [24] Aumann, T., Prog. Part. Nucl. Phys., 59 (2007) 3.
- [25] Herlert, A., EPJ Web Conf., 71 (2014).
- [26] Lestinsky, M., Andrianov, V., Aurand, B., Bagnoud, V. et al., Eur. Phys. J. Spec. Top., 225 (2016) 797.
- [27] Berg, G.P.A., Bardayan, D.W., Blackmon, J.C., Chipps, K.A. et al., Nucl. Instruments Methods Phys. Res. Sect. B, Beam Interact. with Mater. Atoms, 376 (2015) 165.
- [28] Baumann, T., Nucl. Instruments Methods Phys. Res. Sect. B, Beam Interact. with Mater. Atoms, 376 (2016) 162.
- [29] Weisshaar, D., Bazin, D., Bender, P.C., Campbell, C.M. et al., Nucl. Instruments Methods Phys. Res. Sect. A, Accel. Spectrometers, Detect. Assoc. Equip., 847 (2017) 187.
- [30] Paschalis, S., Lee, I.Y., MacChiavelli, A.O., Campbell, C.M. et al., Nucl. Instruments Methods Phys. Res. Sect. A, Accel. Spectrometers, Detect. Assoc. Equip., 709 (2013) 44.
- [31] Akkoyun, S., Algora, A., Alikhani, B., Ameil, F. et al., Nucl. Instruments Methods Phys. Res. Sect. A, Accel. Spectrometers, Detect. Assoc. Equip., 668 (2012) 26.
- [32] Langer, C., Montes, F., Aprahamian, A., Bardayan, D.W. et al., Phys. Rev. Lett., 113 (2014) 32502.
- [33] Langer, C., Montes, F., Aprahamian, A., Bardayan, D.W. et al., Inpc 2013, 66 (2013) 1000.
- [34] Ong, W.-J., Langer, C., Montes, F., Aprahamian, A. et al., Phys. Rev. C, 95 (2017) 55806.
- [35] Kankainen, A., Woods, P.J., Nunes, F., Langer, C. et al., Eur. Phys. J. A, 52 (2016) 6.
- [36] Kankainen, A., Woods, P.J., Schatz, H., Poxon-Pearson, T. et al., Phys. Lett. Sect. B, Nucl. Elem. Part. High-Energy Phys., 769 (2016) 549.
- [37] Schatz, H., Aprahamian, A., Barnard, V., Bildsten, L. et al., Phys. Rev. Lett., 86 (2001) 3471.
- [38] Schatz, H., Aprahamian, A., Görres, J., Wiescher, M. et al., Phys. Rep., 294 (1998) 167.
- [39] Fisker, J.L., Brown, E., Liebendoerfer, M., Schatz, H. et al., Astrophysics, 16783 (2004) 4.
- [40] Keek, L., Wolf, Z. and Ballantyne, D.R., Astrophys. J., 826 (2016) 79.
- [41] Cyburt, R.H., Amthor, A.M., Heger, A., Johnson, E. et al., Astrophys. J., 830 (2016) 55.
- [42] Smith, K., Amthor, A.M., Cyburt, R., Ferguson, R. et al., in: Proc. Sci. (2008).
- [43] Parikh, A., José, J., Moreno, F. and Iliadis, C., Astrophys. J. Suppl. Ser., 178 (2008) 110.
- [44] Schatz, H. and Ong, W.J., Astrophys. J., 844 (2017) 139.
- [45] Rehm, K.E. et al., Phys. Rev. Lett., 80 (1998) 676.
- [46] <http://eagle.phys.utk.edu/xnet/trac/> (2017).

- [47] Cyburt, R.H, Amthor, A.M., Ferguson, R., Meisel, Z. et al., *Astrophys. J. Suppl. Ser.*, 189 (2010) 240.
- [48] Köppchen, C., Bachelor thesis, University of Frankfurt, (2016).
- [49] Fryer, C.L., Belczynski, K., Wiktorowicz, G., Dominik, M. et al., *Astrophys. Journal*, 749(1) (2012) 14.
- [50] Fryer, C.L. and Warren, M.S., *Astrophys. Journal*, 574 (2002) L65.
- [51] Janka, H.-T., *Annu. Rev. Nucl. Part. Sci.*, 62 (2012) 407.
- [52] Hansen, C.J., Montes, F. and Arcones, A., *Astrophys. J.*, 797 (2014) 123.
- [53] Travaglio, C., Gallino, R., Amari, S., Zinner, E. et al., *Astrophys. J.*, 510 (1999) 325.
- [54] Hoppe, P. and Zinner, E., *J. Geophys. Res. Sp. Phys.*, 105 (2000) 10371.
- [55] Zinner, E., in: "Treatise Geochemistry" Second Ed. (2013), pp. 181–213.
- [56] Zinner, E., Nittler, L.R., Gallino, R., Karakas, A.I. et al., *Astrophys. J.*, 650 (2006) 350.
- [57] Lodders, K. and Amari, S., *Chemie Der Erde - Geochemistry*, 65 (2005) 93.
- [58] Nittler, L.R., Amari, S., Zinner, E., Woosley, S.E. et al., *Astrophys. J. Lett.*, 462 (1996) L31.
- [59] Hoppe, P., Strebelt, R., Eberhardt, P., Amari, S. et al., *Science*, 272 (1996) 1314.
- [60] Amari, S., Nittler, L.R., Zinner, E., Lodders, K. et al., *Astrophys. J.*, 559 (2001) 463.
- [61] Fujiya, W., Hoppe, P., Zinner, E., Pignatari, M. et al., *Astrophys. J.*, 776 (2013) L29.
- [62] Pignatari, M., Wiescher, M., Timmes, F.X., de Boer, R.J. et al., *Astrophys. J. Lett.*, 767 (2013) L22.
- [63] Amari, S., Zinner, E. and Lewis, R.S., *Astrophys. J. Lett.*, 517 (1999) L59.
- [64] Gyngard F., Nittler, L. and Zinner, E., *Meteorit. Planet.*, (2010).
- [65] Xu, Y.C., Amari, S., Gyngard, F., Zinner, E. et al., *Aust. Publ. Meteorit. Planet. Sci. Suppl.*, 75 (2012) 5104.
- [66] Hoppe, P., Fujiya, W. and Zinner, E., *Astrophys. J.*, 745 (2012) L26.
- [67] Pignatari, M., Zinner, E., Bertolli, M.G., Trappitsch, R. et al., *Astrophys. J.*, 771 (2013) L7.
- [68] Meyer, B.S. and Clayton, D.D., *Astrophys. J. Lett.*, 540 (2000) L49.
- [69] [Http://exp-Astro.physik.uni-Frankfurt.de/netz/](http://exp-Astro.physik.uni-Frankfurt.de/netz/) (2017).
- [70] Dillmann, I., Heil, M., Käppeler, F., Plag, R. et al., in: *AIP Conf. Proc.* (2006), p.123.
- [71] Dillmann, I., Plag, R., Käppeler, F., Mengoni, A. et al., in: *Proc. Sci.*, (2014).
- [72] Klapper, N., Bachelor thesis, University of Frankfurt, (2016).
- [73] Langer, C., Lepyoshkina, O., Aksyutina, Y., Aumann, T. et al., *Phys. Rev. C*, 89 (2014) 35806.
- [74] Marganiec, J., Novo, S.B., Typel, S., Langer, C. et al., *Phys. Rev. C*, 93 (2016) 45811.

### Characterization of Composite Electron Sources (Metal - Insulator - Vacuum)

A. M. Al-Qudah<sup>a</sup>, S. S. Alnawasreh<sup>a</sup>, M. A. Madanat<sup>a</sup>, O. Trzaska<sup>b</sup>, D. Matykiewicz<sup>c</sup>, S. S. Alrawshdeh<sup>d</sup>, M. J. Hagmann<sup>e</sup> and M. S. Mousa<sup>a</sup>

<sup>a</sup> Department of Physics, Mu'tah University, Al-Karak 61710, Jordan.

<sup>b</sup> Laboratory of Plastics, Wrocław University of Technology, Wrocław 5031, Poland.

<sup>c</sup> Institute of Materials Technology, Poznan University of Technology, Poznan 61138, Poland.

<sup>d</sup> Department of Mechanical Engineering, Mu'tah University, Al-Karak 61710, Jordan.

<sup>e</sup> University of Utah, Department of Electrical and Computer Engineering, Salt Lake City, UT 84112, USA.

---

Received on: 24/7/2017;

Accepted on: 18/2/2018

---

**Abstract:** Field electron emission measurements were performed on composite tips (Insulator- Tungsten) that were prepared by electrochemical etching in NaOH solution. The current-voltage (I-V) characteristics and field electron emission images were recorded under UHV conditions with a base pressure of  $<10^{-9}$  mbar. Next, the tips were coated with several different types of dielectric layers. Various techniques were employed to measure the characteristics of these types of emitters and to evaluate the effects of different types of dielectric coatings on the performance and reliability of such an electron source.

**Keywords:** Field electron emitter, Dielectric layers, Composite tip, Field electron microscope.

## Introduction

Electron sources employing field emitters have not been reported until 1954 [1, 2]. The first utilization of the field electron emission mechanism appeared lately in 1968, as part of a scanning electron microscope [1, 2]. Field electron emission (FEE) is the emission of electrons from the surface of a cathode under the influence of a high applied electrostatic field (typically about 3 V/nm) [3, 4]. Considerable experimental studies of field emission have been carried out on carbon fibers, tungsten (W) and lanthanum hexaboride [5]. The most widely used material for field emitters is tungsten [6, 7]. Tungsten brings several benefits due to its favorable properties, such as the high melting point of 3377 °C, a work function of 4.55eV, high hardness (strength) and appropriate heat

resistance at high temperatures [8]. Techniques for preparing field emission cathodes have been developed. Advances in vacuum technology have also been important, since a high-quality vacuum is essential for reliable operation of field-emission cathodes. These changes have enabled the widespread use of field-emission cathodes [9, 10]. Cathode-manufacturing technology based on electrolytic etching [11] has been studied and enhanced. This technology makes it possible to prepare a cathode tip with a diameter of several nanometers [12]. Composite micropoint cathodes have been prepared to avoid degradation of the electron emitter due to ion sputtering processes during emission for long lifetime and to improve the emission characteristics [5, 13-15, 16]. The research

reported here includes comparing the current-voltage (I-V) characteristics in Fowler-Nordheim (F-N) plots, in addition to determining the spatial emission current distributions and the emission stability (electron emission images) with various dielectrics.

## Materials and Methods

The procedures for coating Tungsten (W) tips have been described [12, 15]. In all cases, the microprint nano-apex metallic emitters used for such measurements were electrolytically etched from 0.1mm diameter tungsten wires with 99.95% purity (good fellow metals) using a 2M solution of NaOH. Then, the tip is ultrasonically cleaned. The coating procedure required slowly dipping the tip into the resin and then carefully removing it to ensure that only a thin film remained on the tip surface. Then, the tip is carefully transferred to an oven and subjected to a curing cycle of thirty minutes at 100 °C to drive off the solvents, followed by another thirty minutes at 185 °C to complete curing of the resin [12, 15]. The coated tips were studied in evacuated field emission microscopes with a diffusion pump system having an additional liquid nitrogen trap. Base pressures of  $5 \times 10^{-8}$  mbar have been reached after baking the system at a temperature of 180 °C for 12 hours with more liquid nitrogen added to the trap. The separation between the cathode and the anode was standardized at ~ 10 mm using a current-limiting resistor of 20 M $\Omega$ . The images presented were taken by a digital camera through the window of the vacuum system. To record the emission behavior in the vacuum, a high-tension (EHT) power supply is used to apply a negative voltage to the cathode. The emission current is

measured with a Keithley 485 auto-ranging picoammeter [17].

## Results

Tungsten microemitters have been analyzed with several coatings: (1) Clark Electromedical Instruments Epoxylite resin, (2) Epidian 6 (based on Bisphenol A), (3) A Radianox compound of graphite colloid and (4) Molyslip 2001 E compound (MoS<sub>2</sub> and MoS). The results presented include the I-V characteristics, F-N plots and emission images. We compared the results with those obtained with clean uncoated tungsten microemitters.

### Composite Tungsten - Clark Electromedical Instruments Epoxylite Resin Tip

First, we determined the emission characteristics of a clean uncoated tungsten tip as shown in I-V characteristics (left) and the Fowler-Nordheim (F-N) plot (right) in Fig. 1. In each case, the potential was slowly increased until the "switch-on voltage"  $V_{sw}$  was reached. At this point, the emission current switches on to a stable saturated value which is called the "switch-on current"  $I_{sat}$ . Here,  $V_{sw} = 2400$  V and  $I_{sat} = 1.5$   $\mu$ A. Fig. 2 (left) shows the I-V characteristics when decreasing the voltage and switch-on voltage with voltage range (2400 - 700) V and current range (1.5  $\mu$ A - 8.8 pA), with the F-N plot on the right side of the same figure. Fig. 3 (left) shows the voltage increasing range (700 - 1900) V and (6.7 pA - 1.1  $\mu$ A), with the F-N plot on the right side of the same figure. Fig. 4 shows a comparison between the field emission of the tungsten tip before and after coating by Clark Electromedical Instruments Epoxylite resin.

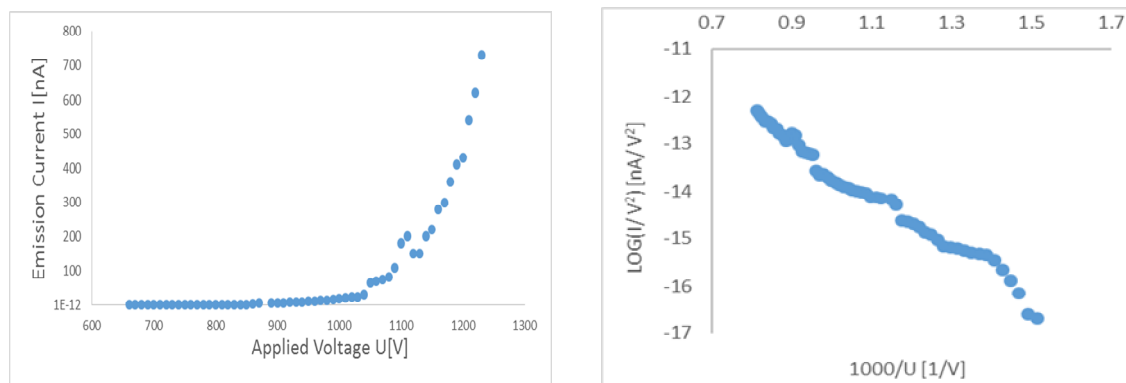


FIG. 1. The I-V characteristics (left) of clean tungsten tip before coating by Clark Electromedical Instruments Epoxylite resin whilst increasing the voltage; and the Fowler-Nordheim plot (right) with a slope of 5500 decades per inverse volt. The applied potential is in the range of (660 - 1230) V.

Characterization of Composite Electron Sources (Metal - Insulator - Vacuum)

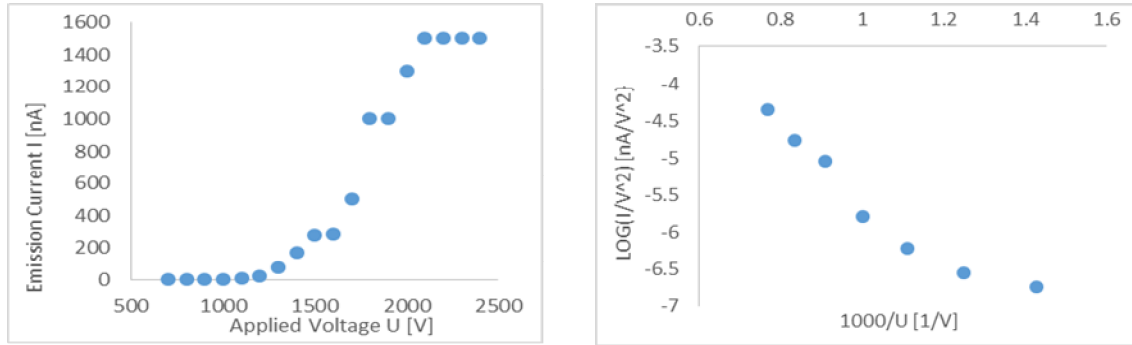


FIG. 2. The I-V characteristics (left) of composite Tungsten - Clark Electromedical Instruments Epoxylite resin during the first decreasing voltage with  $V_{sw}$  (2400 V, 1.5  $\mu$ A); and Fowler-Nordheim plot (right). The F-N plot slope is 3800 decades per inverse volt. The applied voltage is in the range of (2400 – 700) V.

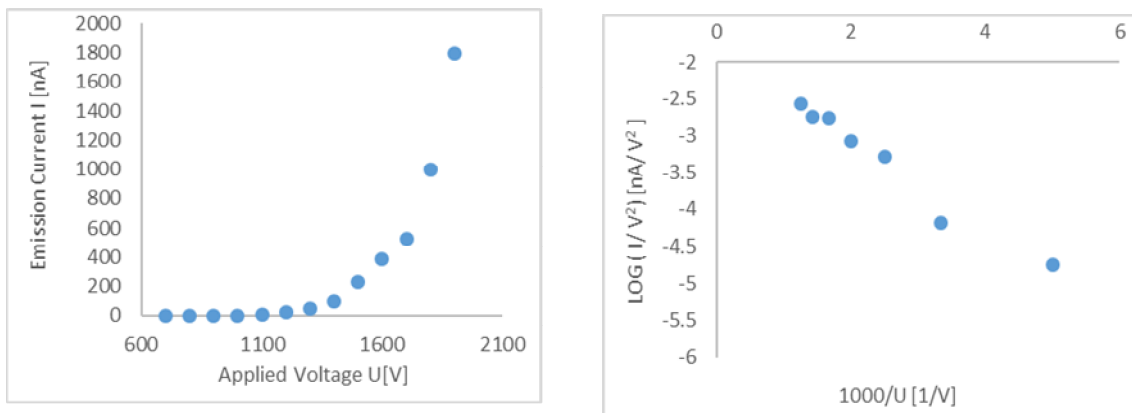


FIG. 3. The I-V characteristics (left) of composite Tungsten-Clark Electromedical Instruments Epoxylite resin during the second increasing voltage; and Fowler-Nordheim plot (right). The F-N plot slope is 260 decades per inverse volt. The applied voltage is in the range of (700 – 1900) V.

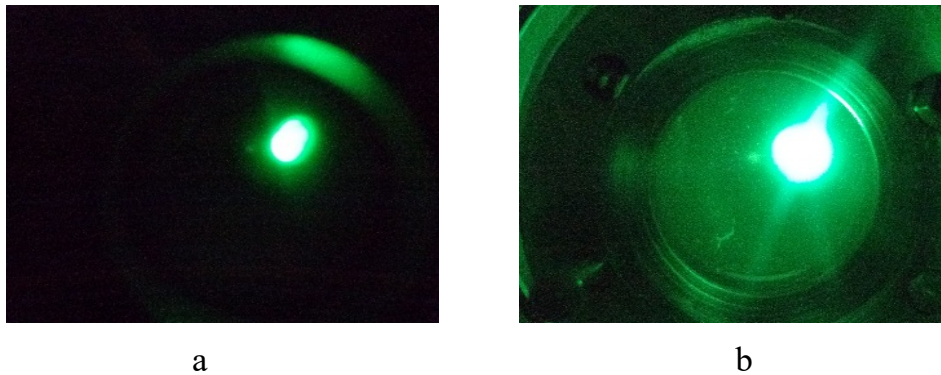


FIG. 4. Comparison between the emission of the tungsten tip before and after coating by Clark Electromedical Instruments Epoxylite resin, (a) Image of field emission of clean tungsten tip before coating. This image was taken at (1050V, 64 nA); and (b) Image of field emission for composite Tungsten-Clark Electromedical Instruments Epoxylite resin tip taken at (1700 V, 1  $\mu$ A).

### Composite Tungsten - Microemitter Epidian 6 (Based on Bisphenol A) Tip

Initially presenting the characteristics of clean tungsten emitter before coating by Microemitter Epidian 6 (based on Bisphenol A), the voltage applied was in the range (390 – 1000) V and the current in the range (8 pA - 1.1  $\mu$ A). Fig. 5 (left) shows I-V characteristics, with the F-N plot on the right side of the same figure. The voltage applied on the composite Tungsten - Coated Microemitter Epidian 6 (based on Bisphenol A) tip was slowly increased across a virgin emitter until a "switch-on voltage"  $V_{sw}$  was reached. At this point, " $V_{sw}$ ", the emission current switches

from an effective zero-value to a stable saturated value, the "switch-on current"  $I_{sat}$ . The  $V_{sw}$  is 6900V and  $I_{sat}$  is 1.2  $\mu$ A. Fig. 6 (left) shows the I-V characteristics for the first decreasing voltage and switch-on voltage with voltage range (6900 - 500) V and current range (1.2  $\mu$ A - 8.3 pA), with the F-N plot on the right side of the same figure. Fig. 7 (left) shows the voltage increasing range (1100- 2900) V and current range (11 pA - 1  $\mu$ A), with the F-N plot on the right side of the same figure. Fig. 8 shows a comparison between the field emission of the tungsten tip before and after coating by Microemitter Epidian 6 (based on Bisphenol A).

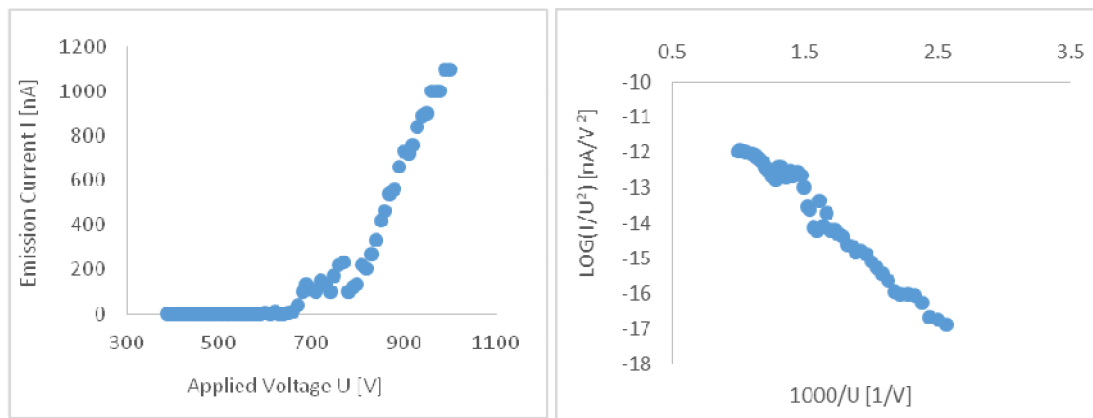


FIG. 5. The I-V characteristics (left) of clean tungsten tip whilst increasing the voltage before coating by Epidian 6 (based on Bisphenol A); and Fowler-Nordheim plot (right) with a slope of 3400 decades per inverse volt. The applied potential is in the range of (390 - 1000) V.

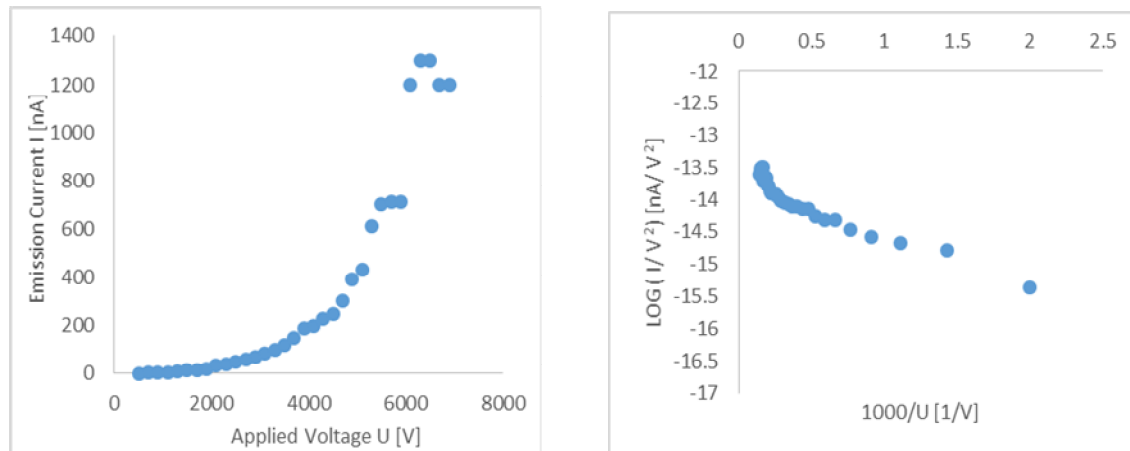


FIG. 6. The I-V characteristics (left) of composite Tungsten - Epidian 6 (based on Bisphenol A) during the first decreasing voltage with  $V_{sw}$  (6900 V, 1.2  $\mu$ A); and Fowler-Nordheim plot (right). The F-N plot slope is 950 decades per inverse volt. The applied voltage is in the range of (6900 – 500) V.



Characterization of Composite Electron Sources (Metal - Insulator - Vacuum)

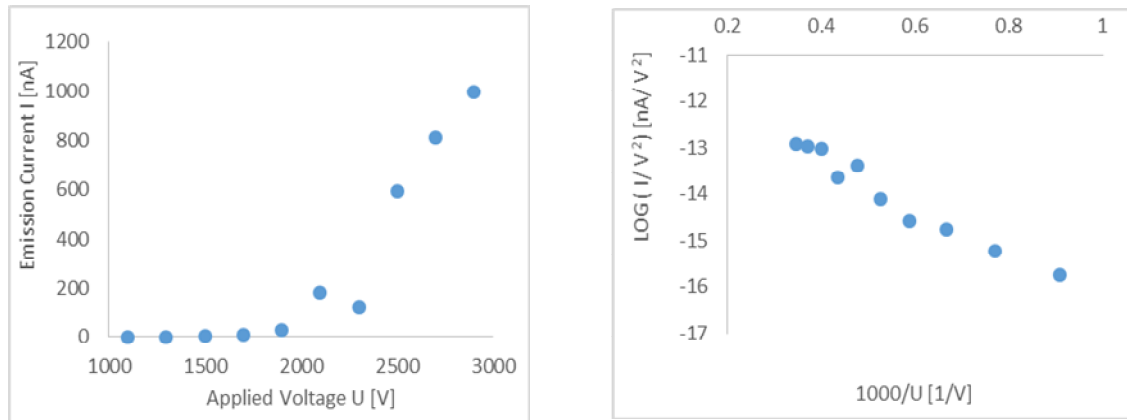


FIG. 7. The I-V characteristics (left) of composite Tungsten - Epidian 6 (based on Bisphenol A) during the second increasing voltage; and Fowler-Nordheim plot (right). The F-N plot slope is 5300 decades per inverse volt. The applied voltage is in the range of (1100 – 2900) V.



FIG. 8. Comparison between the emission of the tungsten tip before and after coating by Microemitter Epidian 6 (based on Bisphenol A), (a) Image of field emission of clean tungsten tip before coating. This image was taken at (1050V, 64 nA); and (b) Image of field emission for composite Tungsten - Microemitter Epidian 6 (based on Bisphenol A) tip taken at (1700 V, 1  $\mu$ A).

**Composite Tungsten - A Radianox Compound of Graphite Colloid Tip**

Presenting the characteristics of clean tungsten emitter before coating by A Radianox compound of graphite colloid, the voltage applied was in the range (800 – 1800) V and the current in the range (76 pA - 770 nA). Fig. 9 (left) shows I-V characteristics, with the F-N plot on the right side of the same figure. The voltage applied on the Composite Tungsten - A Radianox compound of graphite colloid tip was slowly increased across a virgin emitter until a "switch-on voltage"  $V_{sw}$  was reached. At this point, " $V_{sw}$ ", the emission current switches on

from an effective zero-value to a stable saturated value, the "switch-on current"  $I_{sat}$ . The  $V_{sw}$  is 2300 V and  $I_{sat}$  is 5.4  $\mu$ A. Fig. 10 (left) shows the I-V characteristics for the first decreasing voltage and switch-on voltage with voltage range (2300- 600) V and current range (5.4  $\mu$ A - 9.1 pA), with the F-N plot on the right side of the same figure. Fig. 11 (left) shows the voltage increasing range (400- 1300) V and current range (11 pA - 780 nA), with the F-N plot on the right side of the same figure. Fig. 12 shows a comparison between the field emission of the tungsten tip before and after coating by A Radianox compound of graphite colloid.

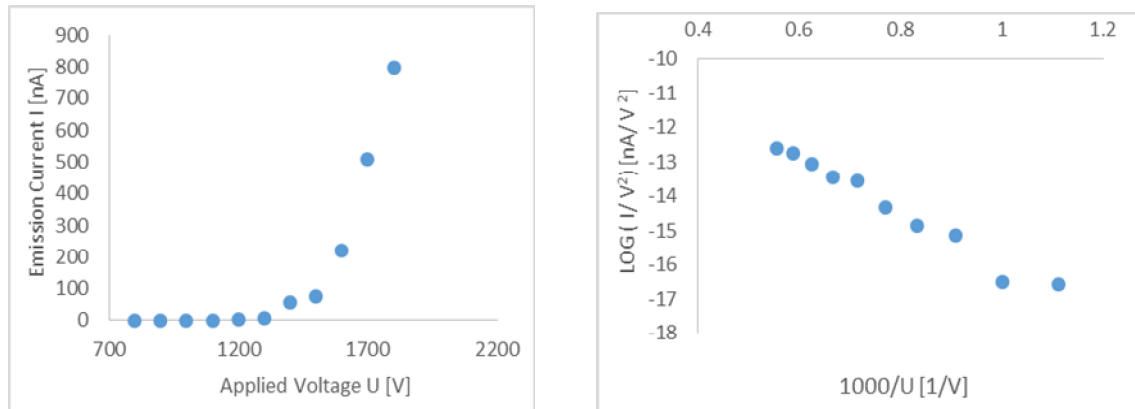


FIG. 9. The I-V characteristics (left) of clean tungsten tip whilst increasing the voltage before coating by A Radianox compound of graphite colloid; and Fowler-Nordheim plot (right) with a slope of 6800 decades per inverse volt. The applied voltage is in the range of (800 – 1800) V.

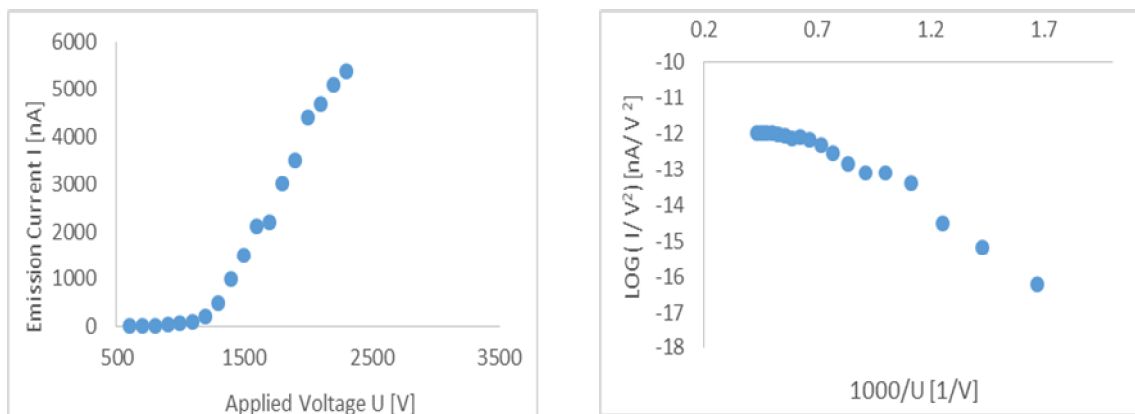


FIG. 10. The I-V characteristics (left) of composite Tungsten - A Radianox compound of graphite colloid during the first decreasing voltage with  $V_{sw}$  (2300 V, 5.4  $\mu$ A); and Fowler-Nordheim plot (right). The F-N plot slope is 3400 decades per inverse volt. The applied voltage is in the range of (2300 – 600) V.

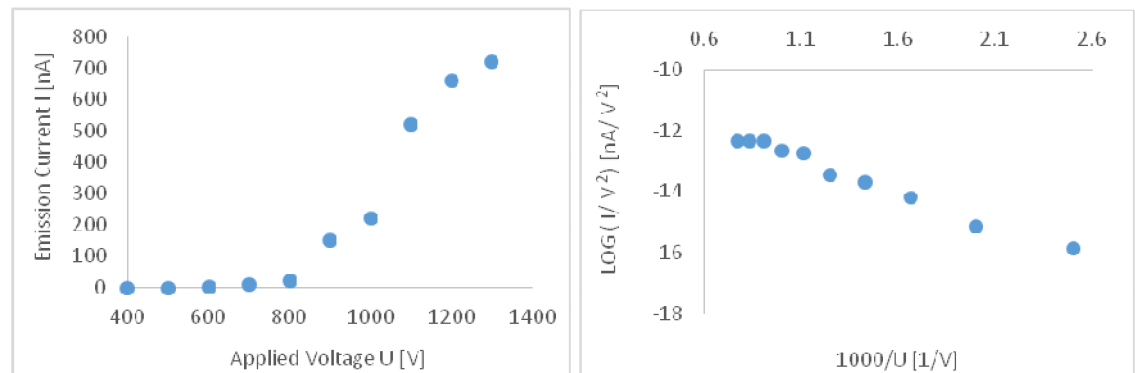


FIG. 11. The I-V characteristics (left) of composite Tungsten - A Radianox compound of graphite colloid during the second increasing voltage; and Fowler-Nordheim plot (right). The F-N plot slope is 2200 decades per inverse volt. The applied voltage is in the range of (400 – 1300) V.



FIG. 12. Comparison between the emission of the tungsten tip before and after coating by A Radianox compound of graphite colloid, (a) Image of field emission of clean tungsten tip before coating. This image was taken at (1800 V, 0.8  $\mu\text{A}$ ); and (b) Image of field emission for composite Tungsten - A Radianox compound of graphite colloid tip taken at (2100 V, 4.7  $\mu\text{A}$ ).

### Composite Tungsten - Molyslip 2001 E Compound ( $\text{MoS}_2$ and MoS) Tip

Presenting the characteristics of clean tungsten emitter before coating by Molyslip 2001 E compound ( $\text{MoS}_2$  and MoS), the voltage applied was in the range (1100 – 2100) V and the current in the range (66 pA - 520 nA). Fig. 13 (left) shows I-V characteristics, with the F-N plot on the right side of the same figure. The voltage applied on the Composite Tungsten - Molyslip 2001 E compound ( $\text{MoS}_2$  and MoS) tip was slowly increased across a virgin emitter until a "switch-on voltage"  $V_{\text{sw}}$  was reached. At this point, " $V_{\text{sw}}$ ", the emission current switches on

from an effective zero-value to a stable saturated value, the "switch-on current"  $I_{\text{sat}}$ . The  $V_{\text{sw}}$  is 2500 V and  $I_{\text{sat}}$  is 7.3  $\mu\text{A}$ . Fig. 14 (left) shows the I-V characteristics for the first decreasing voltage and switch-on voltage with voltage range (2500 - 600) V and current range (7.3  $\mu\text{A}$  - 88 pA), with the F-N plot on the right side of the same figure. Fig. 15 (left) shows the voltage increasing range (500 - 1300) V and current range (11 pA to 440 nA), with the F-N plot on the right side of the same figure. Fig. 16 shows a comparison between the field emission of the tungsten tip before and after coating by Molyslip 2001 E compound ( $\text{MoS}_2$  and MoS).

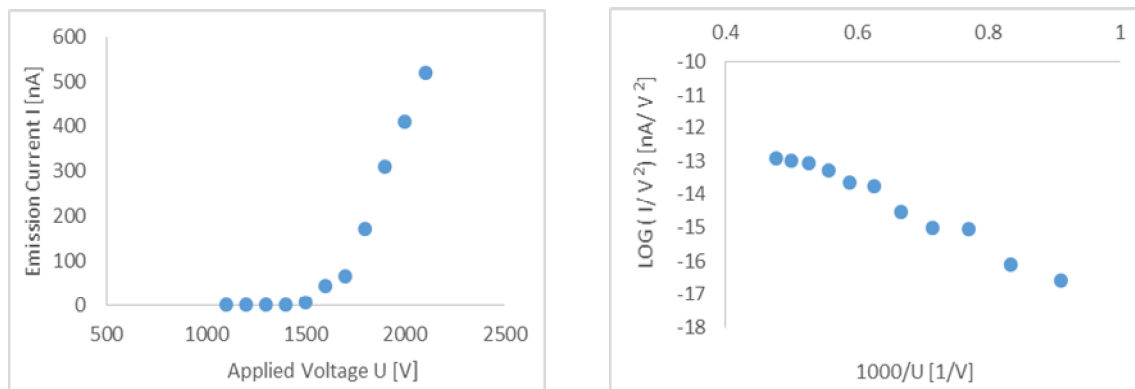


FIG. 13. The I-V characteristics (left) of clean tungsten tip before coating by Molyslip 2001 E compound ( $\text{MoS}_2$  and MoS) whilst increasing the voltage; and Fowler-Nordheim plot (right). The F-N plot slope is 9000 decades per inverse volt. The applied voltage is in the range of (1100 – 2100) V.

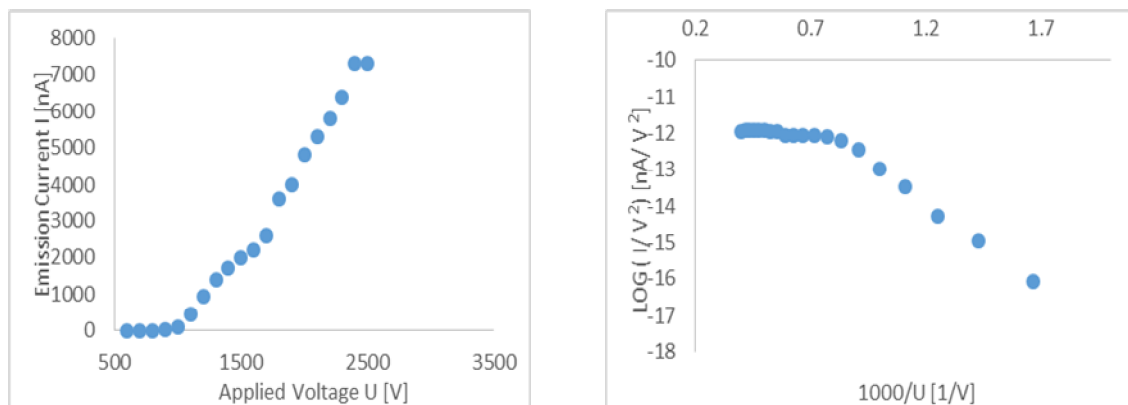


FIG. 14. The I-V characteristics (left) of composite Tungsten - Molyslip 2001 E compound ( $\text{MoS}_2$  and MoS) during the first decreasing voltage with  $V_{sw}$  (2500 V, 7.3  $\mu\text{A}$ ); and Fowler-Nordheim plot (right). The F-N plot slope is 3100 decades per inverse volt. The applied voltage is in the range of (2500 – 600) V.

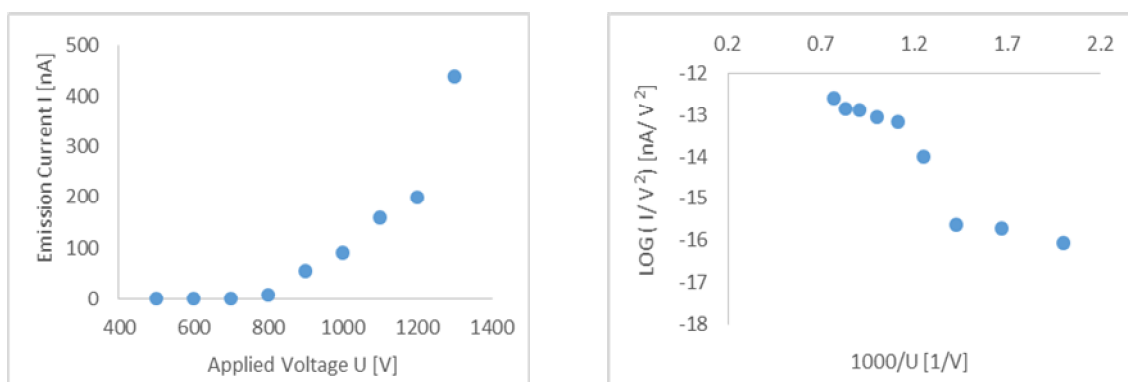


FIG. 15. The I-V characteristics (left) of composite Tungsten - Molyslip 2001 E compound ( $\text{MoS}_2$  and MoS) during the second increasing voltage; and Fowler-Nordheim plot (right). The F-N plot slope is 3300 decades per inverse volt. The applied voltage is in the range of (500 – 1300) V.

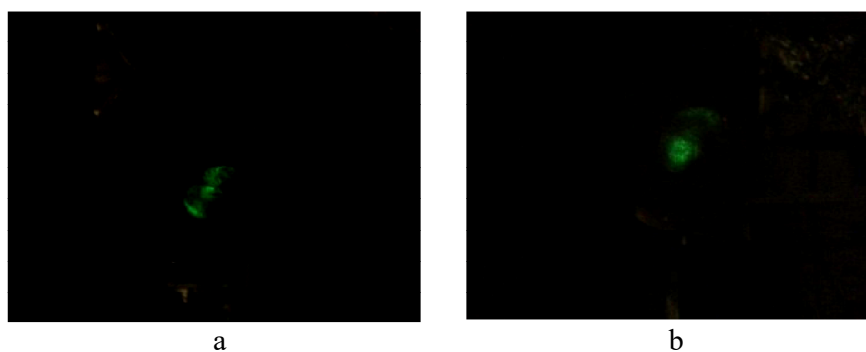


FIG. 16. comparison between the emission of the tungsten tip before and after coating by Molyslip 2001 E Compound ( $\text{MoS}_2$  and MoS), (a) Image of field emission of clean tungsten tip before coated. This images was taken at (2100 V, 0.5  $\mu\text{A}$ ); and (b) Image of field emission for composite Tungsten - A Molyslip 2001 E Compound ( $\text{MoS}_2$  and MoS) tip taken at (1300 V, 0.4  $\mu\text{A}$ ).

Characterization of Composite Electron Sources (Metal - Insulator - Vacuum)

TABLE 1. The extent of changes on the current-voltage (I-V) characteristics of the modified composite electron emitters after being coated with dielectric layer.

Emitter	Clean tip characteristics			Composite tip Characteristics					
	Applied Voltage Range (V)	Emission Current Range (nA)	F-N plot Slope (decades per inverse volt)	Switch-on Applied Voltage Range (V)	Switch-on Emission Current Range (nA)	F-N plot Slope (decades per inverse volt)	Applied Voltage Range (V)	Emission current range (nA)	F-N plot Slope (decades per inverse volt)
Composite Tungsten – Clark Electromedical Instruments EpoxyLite resin	660 - 1230	0.0011- 1500	5500	2400 - 700	1500 – 0.0088	3800	700 - 1900	0.0067 - 1100	260
Composite Tungsten – Microemitters Epidian 6 (based on Bisphenol A)	390 - 1000	0.008 - 1100	3400	6900 - 500	1200 – 0.0083	950	1100 - 2900	0.0011 - 1000	5300
Composite Tungsten – A Radianox Compound of Graphite Colloid	800 - 1800	0.0076 - 770	6800	2300 - 600	5400 – 0.0091	3400	400 - 1300	0.0011 - 780	2200
Composite Tungsten - Molyslip 2001 E Compound (MoS <sub>2</sub> and MoS)	1100 - 2100	0.0066 - 520	9000	2500 - 600	7300 – 0.0088	3100	500 - 1300	0.0011 - 440	3300

## Discussion and Conclusions

In composite emitters consisting of clean tungsten tips with known profile, coated with a variety of insulating materials, the field emission characteristics of a tungsten electron source are intrinsically changed by coating the tips with a micro-thin layer of insulating material. This is in line with the results obtained from similar studies [12-15]. This change in characteristics varies depending on the type of insulating material used in coating the tungsten tips; this is evident by comparing the effects of insulation materials used in this work (Clark Electromedical Instruments EpoxyLite resin, Epidian 6 (based on Bisphenol A), A Radianox

compound of graphite colloid and Molyslip 2001 E compound (MoS<sub>2</sub> and MoS)) on tungsten tip properties. According to the results, A Radianox compound of graphite colloid and Molyslip 2001 E compound (MoS<sub>2</sub> and MoS) have shown an improvement in I-V characteristics and were consequently getting on higher current at the same voltage. Moreover, the emission current during using the four isolators becomes more focused and brighter. Table 1 shows the extent of changes on the I-V characteristics of the modified composite electron emitters after being coated with dielectric layer.

## Acknowledgements

Ala'a M. Al-Qudah would like to express gratitude to the Scientific Research Support Fund (SRSF) in the Hashemite Kingdom of

Jordan for financial support that enabled completing this research work.

---

## References

- [1] Crewe, A.V., *Journal of Applied Physics*, 39(13) (1968) 5861.
- [2] Crewe, A.V. and Wall, J., *Journal of Molecular Biology*, 48(3) (1970) 375.
- [3] Mousa, M.S., *Appl. Surf. Sci.*, 94/95 (1996) 129.
- [4] Forbes, R.G., Deane, J.H., Hamid, N. and Sim, H.S., *Journal of Vacuum Science and Technology B*, 22 (2004) 1222.
- [5] Mousa, M.S., Haggmann, M.J., Brugat, M. and Sheshin, E.P., *Ultramicroscopy*, 95 (2003) 119.
- [6] Crewe, A.V., Isaacson, M. and Johnson, D., *Rev. Sci. Instrum.*, 40(2) (1969) 241.
- [7] Mousa, M.S. and Al-Share, M., *Ultramicroscopy*, 79(1-4) (1999) 195.
- [8] Andrews, J.N. and Ubbelohde, A.R., *Proc. R. Soc. Lond. A* 1955, 228 (1955) 435.
- [9] Mousa, M.S., Karpowicz, A. and Surma, S., *Vacuum*, 45(2/3) (1994) 249.
- [10] Alnawasreh, S.S., Mousa, M.S. and Al-Rabadi, A., *Jordan J. Phys.*, 2 (2015) 95.
- [11] Melmed, A.J., *Journal of Vacuum Science*, 9(2) (1991) 601.
- [12] Lathm, R.V. and Mousa, M.S., *Applied Physics*, 19 (1986) 699.
- [13] Mousa, M.S., *Surface Science*, 231 (1990) 142.
- [14] Mousa, M.S., Fischer, A. and Mussa, K.O., *Jordan J. Phys.*, 1 (2012) 21.
- [15] Al-Qudah, A., Mousa, M.S. and Fischer, A., *IOP Conf. Series: Materials Science and Engineering*, 92 (2015) 012021.
- [16] Mousa, M.S., Lorenz, K.L. and Xu, N.S., *Ultramicroscopy*, 79(1-4) (1999) 43.
- [17] Mousa, M.S., Alnawasreh, S., Madanat, M.A. and Al-Rabadi, A.N., *IOP Conf. Series: Materials Science and Engineering*, 92 (2015) 012022.

### Equations of Motion for Ideal Hydrodynamics in Rotating Frame Using Caputo's Definition

**Emad K. Jaradat** and **Rabea'h A. Al-Fuqaha**

*Physics Department, Mutah University, Al-Karak, Jordan.*

---

*Received on: 24/7/2017;*

*Accepted on: 25/10/2017*

---

**Abstract:** In this paper, we describe the motion of ideal hydrodynamics in a rotating frame by the equations of motion using Caputo's fractional derivative. Then, from the fractional Euler-Lagrangian equation, we obtain the equations that describe the motion of ideal fluid in fractional form, the Hamiltonian density and the energy-stress tensor obtained in fractional form from the fluid Lagrangian density. Finally, from the Hamiltonian density, we also find the Hamiltonian equations of motion for the ideal fluid in fractional form.

**Keywords:** Ideal fluid Lagrangian density, Caputo's definition, Fractional Hamiltonian.

#### Introduction

Fractional calculus is one of the generalizations of the classical calculus. It has been used successfully in various fields of science and engineering [1-4]. The physical and geometrical meanings of the fractional derivatives have been investigated by several authors. The fractional calculus has grown up as a pure mathematical field useful for mathematics only and had no acceptable geometrical or physical interpretation for nearly three decades. But, it did not remain as a mere field of mathematics and rose to the physical world. The first book on the topic was published by Oldham and Spinier in 1974 [1-4]. During the past decade, several studies were conducted on the fractional variational calculus and its applications. These applications include classical and quantum mechanics, field theory, optimal control and fractional minimization problem [1-4].

Fractional calculus appeared in many science and engineering fields, and has recently become widely used, because studies proved that the fractional derivatives and integrals are appropriate to solve many problems, such as the problem of viscoelasticity, which has been solved by Caputo [1-4].

In fluid field, Saarloos [4] showed that the density function (mass, momentum and energy fields) obeys a Liouville equation for hydrodynamic ideal fluid. Poplawski [5] combined two variational approaches (Taub and Ray) to relativistic hydrodynamics of perfect fluid into another simple formulation. Kass [6] used an Eulerian and Lagrangian representation of all prognostic variables to solve the equations in fluid dynamics, among many others.

The main goal of this work is to derive the equations of motion for ideal hydrodynamics in a rotating frame from the Lagrangian density and the Hamiltonian density in fractional form and determine the energy-stress tensor in fractional form by using Caputo's fractional derivative.

#### Basic Definitions

In fractional calculus, there are many definitions of derivatives: Riemann-Liouville, Caputo, Marchaud and Riesz fractional derivatives [7]. In this work, we use the Caputo fractional derivative. Caputo introduced the definition of Riemann-Liouville fractional derivative called Caputo's derivative in 1967, as shown in [8].

$${}_t^c D_b^\alpha = \frac{1}{\Gamma(n-\alpha)} \int_t^b (\tau - t)^{n-\alpha-1} \left(-\frac{d}{d\tau}\right)^n f(\tau) d\tau \quad (1)$$

$${}_a^c D_t^\alpha = \frac{1}{\Gamma(n-\alpha)} \int_a^t (t - \tau)^{n-\alpha-1} \left(\frac{d}{d\tau}\right)^n f(\tau) d\tau \quad (2)$$

where  $\alpha$  ( $\alpha \in +\mathbb{R}$ ) is the order of derivative and  $n - 1 \leq \alpha < n$ , where  $n$  is an integer. ( $a, b \in \mathbb{R}$ ) and ( $\Gamma$ ) denotes Euler's gamma function.

If  $\alpha = n$ , then:

$${}_a^c D_t^\alpha [f(t)] = \frac{d^n}{dt^n} f(t) \quad (3a)$$

$${}_t^c D_b^\alpha [f(t)] = (-1)^n \frac{d^n}{dt^n} f(t) \quad (3b)$$

The properties of Caputo's fractional derivative are [9]:

First, the derivative of a constant is zero:

$${}_t^c D_t^\alpha (C) = 0. \quad (4)$$

Another property is that the Caputo fractional derivative for the power function ( $t^\mu$ ) where  $\mu \geq 0$ , has the following expression:

$${}_t^c D_t^\alpha (t^\mu) = \frac{\Gamma(\mu+1)}{\Gamma(\mu+1-\alpha)} t^{\mu-\alpha}. \quad (5)$$

Finally, the Leibniz rule for the Caputo fractional derivative is:

$${}_t^c D^\alpha (f(t)g(t)) = \sum_{k=0}^{\infty} \binom{\alpha}{k} \left(D^{\alpha-k} f(t)\right) g^{(k)}(t) - \sum_{k=0}^{n-1} \frac{t^{k-\alpha}}{\Gamma(k+1-\alpha)} \left((f(t)g(t))^{(k)}(0)\right) \quad (6)$$

where the derivative of two functions is continuous in  $[0, t]$  and  $t > 0, \alpha \in \mathbb{R}, n - 1 < \alpha < n \in \mathbb{N}$ .

### Lagrangian Density for Ideal Hydrodynamics in a Rotating Frame

Ideal fluid does not exist, but some fluids have a very small viscosity that can be neglected. That means that the ideal fluid should be inviscid, steady, incompressible and irrotational [10].

The frames of reference are of two kinds:

An inertial frame in which Newton's law of inertia holds, where the velocity of the motion is constant; and a non-inertial frame such as rotating frame, where net force causes acceleration [11].

In rotating frame, the Lagrangian density for ideal hydrodynamics is :

$$\begin{aligned} \mathcal{L} = \rho_0 \left[ \frac{1}{2} \left( v^2 + 2\Omega v \cdot (\hat{\Omega} \times r) \right. \right. \\ \left. \left. + \Omega^2 \left( r^2 - (\hat{\Omega} \cdot r)^2 \right) \right) - \Phi(r) \right. \\ \left. - e(F\rho_0^{-1}, s_0) \right] \end{aligned} \quad (7)$$

where  $\rho_0$ : the density of the fluid at zero time.

$v$ : the velocity of the fluid and it is the time derivative of position ( $v = \partial_0 r$ ).

$r$ : displacement field.

$\Phi(r)$ : gravitational potential.

$e$ : internal energy per unit mass and it is a function of  $e(V, s)$ ; where the specific volume is :

$$V = \rho^{-1} \quad (8)$$

and  $s$ : is the specific entropy.

At fixed coordinates ( $a$ ),

$$s(a, t) = s_0(a) \quad (9a)$$

and

$$\rho(a, t) = F^{-1} \rho_0(a). \quad (9b)$$

Hence, the deformation tensor ( $F_{ij}$ ) is :

$$F_{ij} = \frac{\partial r_i}{\partial a_j} \quad (10)$$

and  $F = \det(F_{ij})$ .

The cofactor ( $C_{ij}$ ) of ( $F_{ij}$ ) is :

$$C_{ij} = \frac{\partial F}{\partial F_{ij}} \quad (11)$$

$\Omega = \frac{d\theta}{dt}$  : the angular rate.

$\hat{\Omega}$  : the rotating axis.

The Euler-Lagrangian equation of motion for the displacement field ( $r$ ) is [12] :

$$\begin{aligned} \frac{\partial \mathcal{L}}{\partial r} - \partial_\alpha \left( \frac{\partial \mathcal{L}}{\partial r_\alpha} \right) = \frac{\partial \mathcal{L}}{\partial r} - \partial_0 \left( \frac{\partial \mathcal{L}}{\partial r_0} \right) - \\ \partial_a \left( \frac{\partial \mathcal{L}}{\partial r_a} \right) = 0; \end{aligned} \quad (12)$$

where

$$\partial r_0 = \partial(\partial_0 r) = \partial \left( \frac{\partial r}{\partial t} \right) = \partial v$$

$$\partial r_a = \partial(\partial_a r) = \partial \left( \frac{\partial r_i}{\partial a_j} \right) = \partial F_{ij}.$$

Then, Eq.(11) becomes :



$$\frac{\partial \mathcal{L}}{\partial r} - \partial_0 \left( \frac{\partial \mathcal{L}}{\partial v} \right) - \partial_a \left( \frac{\partial \mathcal{L}}{\partial F_{ij}} \right) = 0. \quad (13)$$

Now, deriving the Lagrangian density for ideal hydrodynamics in a rotating frame from Eq. (7) with respect to the displacement field ( $r$ ) yields:

$$\frac{\partial \mathcal{L}}{\partial r} = \rho_0 \left( \Omega (v \times \hat{\Omega}) + \Omega^2 (r - (\hat{\Omega} \cdot r) \hat{\Omega}) - \frac{\partial \Phi(r)}{\partial r} \right) \quad (14)$$

and

$$\begin{aligned} \partial_0 \left( \frac{\partial \mathcal{L}}{\partial v} \right) &= \partial_0 \rho_0 (v + \Omega \cdot (\hat{\Omega} X r)) \\ &= \rho_0 (\partial_0 v + \Omega \cdot (\hat{\Omega} X \partial_0 r)) \end{aligned}$$

$$\partial_a \left( \frac{\partial \mathcal{L}}{\partial F_{ij}} \right) = \rho_0 (\partial_0 v + \Omega \cdot (\hat{\Omega} X v)) \quad (15)$$

and

$$\begin{aligned} \partial_a \left( \frac{\partial \mathcal{L}}{\partial F_{ij}} \right) &= \partial_a \left( -\rho_0 \frac{\partial e}{\partial F_{ij}} \right) \\ \partial_a \left( \frac{\partial \mathcal{L}}{\partial F_{ij}} \right) &= \partial_a \left( -\rho_0 \frac{\partial e}{\partial v} \frac{\partial v}{\partial F_{ij}} \right). \end{aligned} \quad (16a)$$

From thermodynamics ( $de = T ds - p dV$ ); with constant entropy, we get :

$$\frac{de}{dV} = -p$$

where  $T$ : temperature in Kelvin.

$s$  : entropy.

$p$  : pressure.

$V$  : volume.

Eq. (15a) becomes:

$$\partial_a \left( \frac{\partial \mathcal{L}}{\partial F_{ij}} \right) = \partial_a \left( \rho_0 p \frac{\partial v}{\partial F_{ij}} \right). \quad (16b)$$

From Eqs. (8) and (9b), we have:

$$V = \rho^{-1} = (F^{-1} \rho_0(a))^{-1} = F \rho_0^{-1}(a).$$

Substituting this result in Eq. (16b), we get:

$$\partial_a \left( \frac{\partial \mathcal{L}}{\partial F_{ij}} \right) = \partial_a \left( \rho_0 p \frac{\partial F \rho_0^{-1}}{\partial F_{ij}} \right) = \partial_a \left( p \frac{\partial F}{\partial F_{ij}} \right). \quad (16c)$$

Using Eq. (11) and Eq. (10), Eq. (16c) becomes:

$$\begin{aligned} \partial_a \left( \frac{\partial \mathcal{L}}{\partial F_{ij}} \right) &= \partial_a (p C_{ij}) = C_{ij} \frac{\partial p}{\partial a_j} = C_{ij} \frac{\partial p}{\partial r_i} \frac{\partial r_i}{\partial a_j} \\ &= C_{ij} F_{ij} \frac{\partial p}{\partial r_i} \end{aligned}$$

$$\partial_a \left( \frac{\partial \mathcal{L}}{\partial F_{ij}} \right) = F \frac{\partial p}{\partial r_i} \quad (17)$$

Substituting Eqs. (14), (15) and (17) in Eq. (13), we obtain:

$$\left[ \begin{array}{c} \rho_0 \left( \Omega (v \times \hat{\Omega}) + \Omega^2 (r - (\hat{\Omega} \cdot r) \hat{\Omega}) - \frac{\partial \Phi(r)}{\partial r} \right) \\ - \rho_0 (\partial_0 v + \Omega \cdot (\hat{\Omega} X v)) - F \frac{\partial p}{\partial r_i} \end{array} \right] = 0. \quad (18)$$

From the properties of cross-product ( $v \times \hat{\Omega} = -\hat{\Omega} X v$ ), Eq. (18) becomes:

$$\left[ \begin{array}{c} \rho_0 (\Omega (v \times \hat{\Omega}) + \Omega^2 (r - (\hat{\Omega} \cdot r) \hat{\Omega}) - \frac{\partial \Phi(r)}{\partial r}) - \rho_0 (\partial_0 v - \Omega (v \times \hat{\Omega})) - F \frac{\partial p}{\partial r_i} \end{array} \right] = 0$$

$$\left[ \begin{array}{c} \rho_0 \left( 2\Omega (v \times \hat{\Omega}) + \Omega^2 (r - (\hat{\Omega} \cdot r) \hat{\Omega}) - \frac{\partial \Phi(r)}{\partial r} \right) \\ - \rho_0 (\partial_0 v) - F \frac{\partial p}{\partial r_i} \end{array} \right] = 0. \quad (19)$$

Dividing Eq. (19) by the deformation force (F), we have:

$$\left[ \begin{array}{c} \rho_0 F^{-1} \left( 2\Omega (v \times \hat{\Omega}) + \Omega^2 (r - (\hat{\Omega} \cdot r) \hat{\Omega}) - \frac{\partial \Phi(r)}{\partial r} \right) \\ - \rho_0 F^{-1} (\partial_0 v) - \frac{\partial p}{\partial r_i} \end{array} \right] = 0. \quad (20)$$

Using Eq. (9b) and rearranging Eq. (20), it becomes:

$$\begin{aligned} \rho (\partial_0 v) &= \left[ \rho \left( 2\Omega (v \times \hat{\Omega}) + \Omega^2 (r - (\hat{\Omega} \cdot r) \hat{\Omega}) - \frac{\partial \Phi(r)}{\partial r} \right) - \frac{\partial p}{\partial r_i} \right] \end{aligned} \quad (21)$$

which is the Lagrangian equation of motion for

ideal hydrodynamics in a rotating frame.

To determine the Hamiltonian density ( $\mathcal{H}$ ) [12]:

$$\mathcal{H} = \pi \dot{r} - \mathcal{L} = \pi(\partial_0 r) - \mathcal{L} = \pi v - \mathcal{L} \quad (22)$$

where ( $\pi$ ) is the conjugate momentum [12]:

$$\pi = \frac{\partial \mathcal{L}}{\partial \dot{r}} = \frac{\partial \mathcal{L}}{\partial(\partial_0 r)} = \frac{\partial \mathcal{L}}{\partial v} = \rho_0 \left( v + \Omega \cdot (\hat{\Omega} X r) \right). \quad (23)$$

The Hamiltonian density ( $\mathcal{H}$ ) from Eq. (22) is:

$$\mathcal{H} = \left[ \begin{array}{c} \rho_0 \left( v + \Omega \cdot (\hat{\Omega} X r) \right) v \\ -\rho_0 \left( \frac{1}{2} \left( v^2 + 2\Omega v \cdot (\hat{\Omega} X r) \right) + \Omega^2 \left( r^2 - (\hat{\Omega} \cdot r)^2 \right) \right) \\ -\Phi(r) - e(F\rho_0^{-1}, s_0) \end{array} \right]$$

$$\mathcal{H} = \left[ \begin{array}{c} \rho_0 \left( v^2 + \Omega v \cdot (\hat{\Omega} X r) \right) \\ -\rho_0 \left( \frac{1}{2} \left( v^2 + 2\Omega v \cdot (\hat{\Omega} X r) \right) + \Omega^2 \left( r^2 - (\hat{\Omega} \cdot r)^2 \right) \right) \\ -\Phi(r) - e(F\rho_0^{-1}, s_0) \end{array} \right]$$

$$\mathcal{H} = \left[ \frac{1}{2} \rho_0 v^2 - \rho_0 \left( \frac{1}{2} \Omega^2 \left( r^2 - (\hat{\Omega} \cdot r)^2 \right) - \Phi(r) - e(F\rho_0^{-1}, s_0) \right) \right]. \quad (24)$$

The Hamiltonian equation of motion for the displacement field ( $r$ ) is:

$$\frac{\partial \mathcal{H}}{\partial r} = -\dot{\pi} - \partial_i \left( \frac{\partial \mathcal{L}}{\partial r_{,i}} \right). \quad (25)$$

Deriving the Hamiltonian density from Eq. (24) with respect to the displacement field ( $r$ ), we obtain:

$$\frac{\partial \mathcal{H}}{\partial r} = -\rho_0 \left( \Omega^2 (r - (\hat{\Omega} \cdot r) \hat{\Omega}) - \frac{\partial \Phi(r)}{\partial r} \right). \quad (26a)$$

From Eq. (17), we get:

$$\partial_i \frac{\partial \mathcal{L}}{\partial r_{,i}} = F \frac{\partial p}{\partial r_i}. \quad (26b)$$

In addition, the conjugate momentum from Eq. (23) is  $\pi = \rho_0 \left( v + \Omega \cdot (\hat{\Omega} X r) \right)$ .

Taking the time derivative for the conjugate momentum, we obtain :

$$\begin{aligned} \dot{\pi} &= \partial_0 \rho_0 \left( v + \Omega \cdot (\hat{\Omega} X r) \right) \\ &= \rho_0 \left( \partial_0 v + \Omega \cdot (\hat{\Omega} X \partial_0 r) \right) \end{aligned}$$

$$\dot{\pi} = \rho_0 \left( \partial_0 v + \Omega \cdot (\hat{\Omega} X v) \right) \quad (26c)$$

Substituting Eqs. (26a), (26b) and (26c) in Eq. (25), we get:

$$\begin{aligned} -\rho_0 \left( \Omega^2 (r - (\hat{\Omega} \cdot r) \hat{\Omega}) - \frac{\partial \Phi(r)}{\partial r} \right) = \\ -\rho_0 \left( \partial_0 v + \Omega \cdot (\hat{\Omega} X v) \right) - F \frac{\partial p}{\partial r_i}. \end{aligned}$$

Using  $\hat{\Omega} X v = -v X \hat{\Omega}$ ,

$$\begin{aligned} -\rho_0 \left( \Omega^2 (r - (\hat{\Omega} \cdot r) \hat{\Omega}) - \frac{\partial \Phi(r)}{\partial r} \right) = \\ \rho_0 \left( -\partial_0 v + \Omega \cdot (v X \hat{\Omega}) \right) - F \frac{\partial p}{\partial r_i}. \end{aligned}$$

Rearranging the equation, we get:

$$\begin{aligned} \rho_0(\partial_0 v) = \left[ \rho_0 \left( \Omega \cdot (v X \hat{\Omega}) + \Omega^2 (r - (\hat{\Omega} \cdot r) \hat{\Omega}) \right. \right. \\ \left. \left. - \frac{\partial \Phi(r)}{\partial r} \right) - F \frac{\partial p}{\partial r_i} \right]. \end{aligned} \quad (27)$$

Dividing Eq. (27) by the deformation force (F) and using Eq. (9b), we get:

$$\begin{aligned} \rho(\partial_0 v) = \left[ \rho \left( \Omega \cdot (v X \hat{\Omega}) + \Omega^2 (r - (\hat{\Omega} \cdot r) \hat{\Omega}) \right. \right. \\ \left. \left. - \frac{\partial \Phi(r)}{\partial r} \right) - \frac{\partial p}{\partial r_i} \right] \end{aligned} \quad (28)$$

which is the Hamiltonian equation of motion.

The energy-stress tensor can be determined as follows:

For the energy-stress tensor ( $T_0^0$ ), deriving the Lagrangian density in Eq. (7) with respect to the time derivative of displacement field ( $\partial_0 r = v$ ) then substituting the result in the equation below, we get [13]:

$$T_0^0 = \frac{\partial \mathcal{L}}{\partial(\partial_0 r)} \partial_0 r - \mathcal{L} = \frac{\partial \mathcal{L}}{\partial v} v - \mathcal{L} \quad (29)$$

$$\begin{aligned} T_0^0 = \left[ \begin{array}{c} \rho_0 \left( v + \Omega \cdot (\hat{\Omega} X r) \right) v \\ -\rho_0 \left( \frac{1}{2} \left( v^2 + 2\Omega v \cdot (\hat{\Omega} X r) \right) + \Omega^2 \left( r^2 - (\hat{\Omega} \cdot r)^2 \right) \right) \\ -\Phi(r) - e(F\rho_0^{-1}, s_0) \end{array} \right] \\ T_0^0 = \left[ \frac{1}{2} \rho_0 v^2 - \rho_0 \left( \frac{1}{2} \Omega^2 \left( r^2 - (\hat{\Omega} \cdot r)^2 \right) - \Phi(r) - e(F\rho_0^{-1}, s_0) \right) \right]. \end{aligned} \quad (30)$$

The result is the same as with the

Hamiltonian density,  $T_0^0 = \mathcal{H}$ .

The energy-stress tensor ( $T_i^0$ ) is:

$$T_i^0 = \frac{\partial \mathcal{L}}{\partial(\partial_0 r)} \partial_i r = \frac{\partial \mathcal{L}}{\partial v} \partial_i r = \rho_0 (v + \Omega \cdot (\hat{\Omega} X r)) \partial_i r. \quad (31)$$

The energy-stress tensor ( $T_0^i$ ) is:

$$T_0^i = \frac{\partial \mathcal{L}}{\partial(\partial_i r)} \partial_0 r \quad (32a)$$

From Eq. (10),  $(\partial_i r = \frac{\partial r_i}{\partial a_j} = F_{ij})$ , Eq. (32a) becomes:

$$T_0^i = \frac{\partial \mathcal{L}}{\partial F_{ij}} \partial_0 r. \quad (32b)$$

From the previous derivation of Lagrangian equation of motion:

$$\frac{\partial \mathcal{L}}{\partial F_{ij}} = p C_{ij}.$$

Then, Eq. (32b) becomes:

$$T_0^i = C_{ij} p v. \quad (33)$$

The energy-stress tensor ( $T_j^i$ ) is:

$$T_j^i = \frac{\partial \mathcal{L}}{\partial(\partial_i r)} \partial_j r = C_{ij} p \partial_j r. \quad (34)$$

The energy-stress tensor ( $T_i^i$ ) is:

$$T_i^i = \frac{\partial \mathcal{L}}{\partial(\partial_i r)} \partial_i r - \mathcal{L} = C_{ij} p \partial_i r - \mathcal{L}$$

where  $\partial_i r = F_{ij}$ , then  $T_i^i = C_{ij} p F_{ij} - \mathcal{L}$ .

From Eq. (11),  $C_{ij} F_{ij} = F$

$$T_i^i = p F - \mathcal{L} \quad (35)$$

### The Lagrangian Density for Ideal Hydrodynamics in Rotating Frame

To obtain the fractional Lagrangian density for ideal hydrodynamics in rotating frame, assume that  $v = \frac{\partial r}{\partial t} = \dot{r}$ , then Eq. (7) becomes:

$$\mathcal{L} = \rho_0 \left[ \frac{1}{2} (\dot{r}^2 + 2\Omega \dot{r} \cdot (\hat{\Omega} X r)) + \Omega^2 (r^2 - \hat{\Omega} \cdot r)^2 - \Phi(r) - e(F\rho_0^{-1}, s_0) \right].$$

The fractional form then is:

$$\mathcal{L} = \rho_0 \left[ \left( \begin{array}{c} ({}_a^c D_t^\alpha r)^2 \\ + 2\Omega ({}_a^c D_t^\alpha r) \cdot (\hat{\Omega} X r) \\ + \Omega^2 (r^2 - (\hat{\Omega} \cdot r)^2) \\ - \Phi(r) - e(F\rho_0^{-1}, s_0) \end{array} \right) \right]. \quad (36)$$

The Euler-Lagrangian equation in fractional form is:

$$\left[ \frac{\partial \mathcal{L}}{\partial r} + {}_t^c D_b^\alpha \frac{\partial \mathcal{L}}{\partial {}_a^c D_t^\alpha r} + x_i {}_b^c D_a^\alpha \frac{\partial \mathcal{L}}{\partial {}_a^c D_{x_i}^\alpha r} + {}_a^c D_t^\beta \frac{\partial \mathcal{L}}{\partial {}_t^c D_b^\beta r} + {}_a^c D_{x_i}^\beta \frac{\partial \mathcal{L}}{\partial x_i {}_t^c D_b^\beta r} \right] = 0. \quad (37)$$

Derive the Lagrangian density from Eq. (36) as follows:

$$\frac{\partial \mathcal{L}}{\partial r} = \rho_0 \left( \Omega ({}_a^c D_t^\alpha r X \hat{\Omega}) + \Omega^2 (r - (\hat{\Omega} \cdot r) \hat{\Omega}) - \frac{\partial \Phi(r)}{\partial r} \right) \quad (38a)$$

$${}_t^c D_b^\alpha \frac{\partial \mathcal{L}}{\partial {}_a^c D_t^\alpha r} = {}_t^c D_b^\alpha \rho_0 ({}_a^c D_t^\alpha r + \Omega \cdot (\hat{\Omega} X r))$$

$${}_t^c D_b^\alpha \frac{\partial \mathcal{L}}{\partial {}_a^c D_t^\alpha r} = \rho_0 ({}_t^c D_b^\alpha {}_a^c D_t^\alpha r + \Omega \cdot (\hat{\Omega} X {}_t^c D_b^\alpha r))$$

$$\text{Use } {}_t^c D_b^\alpha = -{}_a^c D_t^\alpha$$

$${}_t^c D_b^\alpha \frac{\partial \mathcal{L}}{\partial {}_a^c D_t^\alpha r} = -\rho_0 (({}_a^c D_t^\alpha)^2 r + \Omega \cdot (\hat{\Omega} X {}_a^c D_t^\alpha r)) \quad (38b)$$

Now,

$$x_i {}_b^c D_a^\alpha \frac{\partial \mathcal{L}}{\partial {}_a^c D_{x_i}^\alpha r}$$

$$\text{But, } ({}_a^c D_{x_i}^\alpha r = F_{ij}), \text{ then } x_i {}_b^c D_a^\alpha \frac{\partial \mathcal{L}}{\partial {}_a^c D_{x_i}^\alpha r} =$$

$$x_i {}_b^c D_a^\alpha \left( \frac{\partial \mathcal{L}}{\partial F_{ij}} \right)$$

$$x_i {}_b^c D_a^\alpha \frac{\partial \mathcal{L}}{\partial {}_a^c D_{x_i}^\alpha r} = x_i {}_b^c D_a^\alpha \left( \frac{\partial \mathcal{L}}{\partial F_{ij}} \right) =$$

$$x_i {}_b^c D_a^\alpha \left( -\rho_0 \frac{\partial e}{\partial F_{ij}} \right) = x_i {}_b^c D_a^\alpha \left( -\rho_0 \frac{\partial e}{\partial v} \frac{\partial v}{\partial F_{ij}} \right). \quad (39a)$$

From thermodynamics, we get  $\frac{de}{dv} = -p$ , then Eq. (39a) becomes:

$$x_i {}_b^c D_a^\alpha \frac{\partial \mathcal{L}}{\partial {}_a^c D_{x_i}^\alpha r} = x_i {}_b^c D_a^\alpha \left( \rho_0 p \frac{\partial v}{\partial F_{ij}} \right). \quad (39b)$$

Using Eq. (8), Eq. (9b) and Eq. (11), then

Eq. (39b) becomes:

$$\begin{aligned} x_i D_b^\alpha \frac{\partial \mathcal{L}}{\partial {}_a^c D_{x_i}^\alpha r} &= x_i D_b^\alpha \left( \rho_0 p \frac{\partial F \rho_0^{-1}}{\partial F_{ij}} \right) = \\ & x_i D_b^\alpha \left( p \frac{\partial F}{\partial F_{ij}} \right) = x_i D_b^\alpha (p C_{ij}) = \\ & C_{ij} x_i D_b^\alpha p \end{aligned}$$

$$\text{Let } x_i D_b^\alpha p = -{}_a^c D_{x_i}^\alpha p$$

$$\begin{aligned} x_i D_b^\alpha \frac{\partial \mathcal{L}}{\partial {}_a^c D_{x_i}^\alpha r} &= -C_{ij} {}_a^c D_{x_i}^\alpha p \\ &= -C_{ij} {}_a^c D_{r_i}^\alpha {}_r_i D_{x_i}^\alpha p = -C_{ij} F_{ij} {}_r_i D_{x_i}^\alpha p \\ x_i D_b^\alpha \frac{\partial \mathcal{L}}{\partial {}_a^c D_{x_i}^\alpha r} &= -F {}_r_i D_{x_i}^\alpha p \end{aligned} \quad (40)$$

$${}_a^c D_t^\beta \frac{\partial \mathcal{L}}{\partial {}_t^c D_b^\beta r} = 0, {}_a^c D_{x_i}^\beta \frac{\partial \mathcal{L}}{\partial {}_t^c D_b^\beta r} = 0 \quad (41)$$

Substituting the results in Eqs. (38a), (38b), (40) and (41) in Eq. (37), we obtain:

$$\begin{bmatrix} \rho_0 \left( \begin{array}{c} \Omega ({}_a^c D_t^\alpha r X \hat{\Omega}) \\ + \Omega^2 (r - (\hat{\Omega} \cdot r) \hat{\Omega}) - \frac{\partial \Phi(r)}{\partial r} \end{array} \right) \\ -\rho_0 \left( \begin{array}{c} ({}_a^c D_t^\alpha)^2 r \\ + \Omega \cdot (\hat{\Omega} X {}_a^c D_t^\alpha r) \end{array} \right) - F {}_r_i D_{x_i}^\alpha p \end{bmatrix} = 0. \quad (42)$$

Use  ${}_a^c D_t^\alpha r X \hat{\Omega} = -\hat{\Omega} X {}_a^c D_t^\alpha r$ , then Eq. (42) becomes:

$$\begin{bmatrix} \rho_0 \left( \begin{array}{c} \Omega ({}_a^c D_t^\alpha r X \hat{\Omega}) \\ + \Omega^2 (r - (\hat{\Omega} \cdot r) \hat{\Omega}) - \frac{\partial \Phi(r)}{\partial r} \end{array} \right) \\ -\rho_0 \left( \begin{array}{c} ({}_a^c D_t^\alpha)^2 r \\ - \Omega \cdot (\hat{\Omega} X {}_a^c D_t^\alpha r) \end{array} \right) - F {}_r_i D_{x_i}^\alpha p \end{bmatrix} = 0$$

$$\begin{aligned} \rho_0 \left( 2\Omega ({}_a^c D_t^\alpha r X \hat{\Omega}) + \Omega^2 (r - (\hat{\Omega} \cdot r) \hat{\Omega}) \right. \\ \left. - \frac{\partial \Phi(r)}{\partial r} \right) - \rho_0 (({}_a^c D_t^\alpha)^2 r) \\ - F {}_r_i D_{x_i}^\alpha p = 0 \end{aligned}$$

Rearranging the equation, we get:

$$\begin{aligned} \rho_0 (({}_a^c D_t^\alpha)^2 r) &= \left[ \rho_0 \left( 2\Omega ({}_a^c D_t^\alpha r X \hat{\Omega}) \right. \right. \\ & \left. \left. + \Omega^2 (r - (\hat{\Omega} \cdot r) \hat{\Omega}) - \frac{\partial \Phi(r)}{\partial r} \right) \right. \\ & \left. - F {}_r_i D_{x_i}^\alpha p \right]. \end{aligned}$$

Dividing the equation by the deformation force ( $F$ ) and using Eq. (9b), we get:

$$\rho (({}_a^c D_t^\alpha)^2 r) = \begin{bmatrix} 2\Omega ({}_a^c D_t^\alpha r X \hat{\Omega}) \\ \rho \left( +\Omega^2 (r - (\hat{\Omega} \cdot r) \hat{\Omega}) - \frac{\partial \Phi(r)}{\partial r} \right) \\ - {}_r_i D_{x_i}^\alpha p \end{bmatrix}. \quad (43)$$

The fractional conjugate momentum is:

$$(\pi_\alpha)_r = \frac{\partial \mathcal{L}}{\partial ({}_a^c D_t^\alpha r)} = \rho_0 \left( {}_a^c D_t^\alpha r + \Omega \cdot (\hat{\Omega} X r) \right). \quad (44)$$

The Hamiltonian density ( $\mathcal{H}$ ) in fractional form is:

$$\mathcal{H} = \pi {}_a^c D_t^\alpha r - \mathcal{L}. \quad (45)$$

Substituting the fractional conjugate momentum from Eq. (44) and the Lagrangian density from Eq.(36) in Eq.(45), the Hamiltonian density ( $\mathcal{H}$ ) becomes:

$$\begin{aligned} \mathcal{H} &= \begin{bmatrix} \rho_0 \left( {}_a^c D_t^\alpha r + \Omega \cdot (\hat{\Omega} X r) \right) {}_a^c D_t^\alpha r \\ - \rho_0 \left( \begin{array}{c} ({}_a^c D_t^\alpha r)^2 \\ + 2\Omega ({}_a^c D_t^\alpha r) \cdot (\hat{\Omega} X r) \\ + \Omega^2 (r^2 - (\hat{\Omega} \cdot r)^2) \end{array} \right) \\ - \Phi(r) - e(F \rho_0^{-1}, s_0) \end{bmatrix} \\ \mathcal{H} &= \rho_0 \begin{bmatrix} \left( \begin{array}{c} ({}_a^c D_t^\alpha r)^2 \\ + \Omega {}_a^c D_t^\alpha r \cdot (\hat{\Omega} X r) \end{array} \right) \\ - \left( \begin{array}{c} ({}_a^c D_t^\alpha r)^2 \\ + 2\Omega ({}_a^c D_t^\alpha r) \cdot (\hat{\Omega} X r) \\ + \Omega^2 (r^2 - (\hat{\Omega} \cdot r)^2) \end{array} \right) \\ - \Phi(r) - e(F \rho_0^{-1}, s_0) \end{bmatrix} \\ \mathcal{H} &= \rho_0 \begin{bmatrix} \left( \begin{array}{c} \frac{1}{2} ({}_a^c D_t^\alpha r)^2 \\ - \frac{1}{2} \Omega^2 (r^2 - (\hat{\Omega} \cdot r)^2) \end{array} \right) \\ + \Phi(r) + e(F \rho_0^{-1}, s_0) \end{bmatrix} \end{aligned} \quad (46)$$

which is the Hamiltonian density for ideal hydrodynamics in a rotating frame in fractional form.

The fractional Hamiltonian equation of motion for the displacement field ( $r$ ) is:

$$\begin{aligned} \frac{\partial \mathcal{H}}{\partial r} &= {}_t D_b^\alpha \pi_\alpha + {}_a^c D_t^\beta \pi_\beta + x_i D_b^\alpha \frac{\partial \mathcal{L}}{\partial {}_a^c D_{x_i}^\alpha r} + \\ & {}_a^c D_{x_i}^\beta \frac{\partial \mathcal{L}}{\partial {}_t^c D_b^\beta r}. \end{aligned} \quad (47)$$

Deriving the Hamiltonian density ( $\mathcal{H}$ ) with respect to ( $r$ ), we get:

$$\frac{\partial \mathcal{H}}{\partial r} = \rho_0 \left( -\Omega^2 (r - (\hat{\Omega} \cdot r) \hat{\Omega}) + \frac{\partial \Phi(r)}{\partial r} \right). \quad (48a)$$

In addition, calculate the conjugate momentum( $\pi$ ):

$$\begin{aligned} (\pi_\alpha)_r &= \frac{\partial \mathcal{L}}{\partial ({}^c_a D_t^\alpha r)} \\ (\pi_\alpha)_r &= \rho_0 \left( {}^c_a D_t^\alpha r + \Omega \cdot (\hat{\Omega} X r) \right) \\ (\pi_\beta)_r &= 0 \end{aligned} \quad (48b)$$

From Eq. (40), we obtain:

$$\begin{aligned} {}^c_{x_i} D_b^\alpha \frac{\partial \mathcal{L}}{\partial {}^c_a D_{x_i}^\alpha r} &= -F r_i {}^c_{x_i} D_{x_i}^\alpha p \\ {}^c_a D_{x_i}^\beta \frac{\partial \mathcal{L}}{\partial {}^c_{x_i} D_b^\beta r} &= 0 \end{aligned} \quad (48c)$$

Substituting the results in Eq. (48a, b, c) in Eq. (47), we have:

$$\begin{aligned} \left[ \rho_0 \left( -\Omega^2 (r - (\hat{\Omega} \cdot r) \hat{\Omega}) + \frac{\partial \Phi(r)}{\partial r} \right) \right] &= \\ \left[ {}^c_t D_b^\alpha \rho_0 \left( {}^c_a D_t^\alpha r + \Omega \cdot (\hat{\Omega} X r) \right) - F r_i {}^c_{x_i} D_{x_i}^\alpha p \right] & \\ \left[ \rho_0 \left( -\Omega^2 (r - (\hat{\Omega} \cdot r) \hat{\Omega}) + \frac{\partial \Phi(r)}{\partial r} \right) \right] &= \\ \left[ \rho_0 \left( {}^c_t D_b^\alpha {}^c_a D_t^\alpha r + \Omega \cdot (\hat{\Omega} X {}^c_t D_b^\alpha r) \right) \right. & \\ \left. - F r_i {}^c_{x_i} D_{x_i}^\alpha p \right] & \\ \text{Use } {}^c_t D_b^\alpha &= -{}^c_a D_t^\alpha \quad \text{and} \quad -\hat{\Omega} X {}^c_a D_t^\alpha r = \\ {}^c_a D_t^\alpha r X \hat{\Omega} & \\ \left[ \rho_0 \left( -\Omega^2 (r - (\hat{\Omega} \cdot r) \hat{\Omega}) + \frac{\partial \Phi(r)}{\partial r} \right) \right] &= \\ \left[ \rho_0 \left( -({}^c_a D_t^\alpha)^2 r + \Omega \cdot ({}^c_a D_t^\alpha r X \hat{\Omega}) \right) \right. & \\ \left. - F r_i {}^c_{x_i} D_{x_i}^\alpha p \right] & \\ \rho_0 ({}^c_a D_t^\alpha)^2 r &= \left[ \rho_0 \left( \begin{array}{l} \Omega \cdot ({}^c_a D_t^\alpha r X \hat{\Omega}) \\ + \Omega^2 (r - (\hat{\Omega} \cdot r) \hat{\Omega}) \end{array} \right) \right. \\ \left. - \rho_0 \frac{\partial \Phi(r)}{\partial r} - F r_i {}^c_{x_i} D_{x_i}^\alpha p \right] & \end{aligned} \quad (49)$$

Dividing Eq. (49) by deformation force ( $F$ ) and using Eq. (9b), we get:

$$\rho ({}^c_a D_t^\alpha)^2 r = \left[ \rho \left( \begin{array}{l} \Omega \cdot ({}^c_a D_t^\alpha r X \hat{\Omega}) \\ + \Omega^2 (r - (\hat{\Omega} \cdot r) \hat{\Omega}) \end{array} \right) \right. \\ \left. - \rho \frac{\partial \Phi(r)}{\partial r} - {}^c_{x_i} D_{x_i}^\alpha p \right] \quad (50)$$

The equation of motion from the fractional Hamiltonian density is the same as the classical one as  $\rightarrow 1$ .

The energy- stress tensor can be determined as follows:

$$\begin{aligned} T_0^0 &= \frac{\partial \mathcal{L}}{\partial {}^c_a D_t^\alpha r} {}^c_a D_t^\alpha r - \mathcal{L} \\ T_0^0 &= \left[ \rho_0 \left( \begin{array}{l} \frac{1}{2} ({}^c_a D_t^\alpha r)^2 \\ - \frac{1}{2} \Omega^2 (r^2 - (\hat{\Omega} \cdot r)^2) \\ + \Phi(r) + e(F \rho_0^{-1}, s_0) \end{array} \right) \right] \end{aligned} \quad (51)$$

We find that  $T_0^0 = \mathcal{H}$ .

The energy-stress tensor ( $T_i^0$ ) is:

$$\begin{aligned} T_i^0 &= \frac{\partial \mathcal{L}}{\partial {}^c_a D_{x_i}^\alpha r} {}^c_a D_{x_i}^\alpha r \text{ where } {}^c_a D_{x_i}^\alpha r = F_{ij} \\ T_i^0 &= \rho_0 ({}^c_a D_t^\alpha r + \Omega \cdot (\hat{\Omega} X r)) F_{ij} \end{aligned} \quad (52)$$

The energy-stress tensor ( $T_0^i$ ) is:

$$\begin{aligned} T_0^i &= \frac{\partial \mathcal{L}}{\partial {}^c_a D_{x_i}^\alpha r} {}^c_a D_t^\alpha r, {}^c_a D_{x_i}^\alpha r = F_{ij} \\ T_0^i &= \frac{\partial \mathcal{L}}{\partial F_{ij}} {}^c_a D_t^\alpha r = C_{ij} p {}^c_a D_t^\alpha r \end{aligned} \quad (53)$$

The energy-stress tensor ( $T_j^i$ ) is:

$$T_j^i = \frac{\partial \mathcal{L}}{\partial {}^c_a D_{x_j}^\alpha r} {}^c_a D_{x_j}^\alpha r = C_{ij} p {}^c_a D_{x_j}^\alpha r \quad (54)$$

The energy-stress tensor ( $T_i^i$ ) is:

$$T_i^i = \frac{\partial \mathcal{L}}{\partial {}^c_a D_{x_i}^\alpha r} {}^c_a D_{x_i}^\alpha r - \mathcal{L} = C_{ij} p {}^c_a D_{x_i}^\alpha r - \mathcal{L}$$

where  ${}^c_a D_{x_i}^\alpha r = F_{ij}$

$$T_i^i = C_{ij} p F_{ij} - \mathcal{L}$$

From Eq. (11),  $C_{ij} F_{ij} = F$ , then:

$$T_i^i = pF - \mathcal{L} \quad (55)$$

## Conclusion

The fluid field has very important applications and it is necessary to study its movement to explain the phenomena related. In calculus, the variation principle is used to find the equations that describe the motion of fluid and the calculations in fractional form give more accurate results. In this paper, we found that the equations of motion for fluids in a rotating frame could be derived in fractional form. Using the Caputo's fractional derivative and at  $\alpha = 1$ , the Lagrangian equation of motion, the Hamiltonian equation of motion and the energy-stress tensor for the displacement field ( $r$ ) in a rotating frame of fluid dynamics are reduced to the classical results, so that the fractional results agree with the classical ones.

## References

- [1] Podlubny, I., "Fractional Differential Equations", (Academic Press, New York, 1999).
- [2] Oldham, K.B. and Spanier, J., "The Fractional Calculus Theory and Applications of Differentiation and Integration to Arbitrary Order", (Academic Press, New York, London, 1974).
- [3] Debnath. L., "Recent Applications of Fractional Calculus for Science and Engineering", (Hindawi Publishing Corp., 2003).
- [4] Saarloos. W.V., Bordeaux, D. and Mazur. P., *Physica A: Statistical Mechanics and Its Applications*, 107(1) (1981) 109.
- [5] Poplawski, N.J., *Physics Letters A*, 373(31) (2009) 2620.
- [6] Kass, E., Sorensen, B., Lauritzen, P.H. and Hansen, A.B., *Geoscientific Model Development*, 6 (2013) 2023.
- [7] Jaradat, E.K., Hijjawi, R.S. and Khalifeh, J.M., *Jordan J. Phys.*, 3(2) (2010) 47.
- [8] Bologna, D., Golmankhaneh, A.K. and Baleanu, M.C., *Int. J. Theor. Phys.*, 49 (2010) 365.
- [9] Ishteva, M., Master Thesis, Department of Mathematics, Universität Karlsruhe (TH), (2005).
- [10] Finnemore, E. and John, F.J., "Fluid Mechanics with Engineering Applications", 10<sup>th</sup> Ed., (2002).
- [11] Fowler, M., "Notes on Special Relativity", (Physics 252, University of Virginia, 2008).
- [12] Mandl, F. and Shaw, G., "Quantum Field Theory", (Wiley-Interscience Publication, John Wiley & Sons, Chichester, New York, Brisbane, Toronto, Singapore).
- [13] McMahon, D., "Quantum Field Theory Demystified", (McGraw-Hill Co., 2008).

## Authors Index

A. M. Al-Qudah.....	59
C. Köppchen.....	45
C. Langer.....	45
D. Brown.....	27
D. Matykiewicz.....	59
E. K. Jaradat .....	69
H. Kropf .....	5
I.G. Koltshugina.....	1
L. C. Costa.....	35
M. A. Madanat.....	59
M. E. Achour .....	35
M. J. Hagmann.....	59
M. Jaskula.....	1
M. S. Mousa. ....	17, 59
M. Timpel.....	5
M.-A. H. Al-Akhras .....	17
N. Klapper .....	45
N. Wanderka.....	5
O. Trzaska .....	59
R. A. Al-Fuqaha.....	69
R. Belhimria .....	35
R. Reifarth.....	27, 45
S. Boukheir.....	35
S. Dababneh.....	27, 45
S. I. Daradkeh .....	17
S. M. Mosby .....	27
S. S. Alnawasreh.....	59
S. S. Alrawshdeh.....	59
Y. A. Litvinov.....	27
Yu. P. Perelygin.....	1
Z. Samir.....	35

## Subject Index

Bode diagram.....	35
Caputo's definition.....	69
Carbon black.....	35
Carbon nanotube fibers (CNTFs).....	17
Cole-Cole .....	35
Complex impedance.....	35
Composite tip.....	59
Dielectric layers .....	59
Facilities .....	45
Field electron emission .....	17
Field electron emitter .....	59
Field electron microscope .....	59
Focused ion beam tomography.....	5
Fractional Hamiltonian.....	69
Glycine .....	1
Hypoeutectic Al-Ge alloys .....	5
Ideal fluid Lagrangian density.....	69
Isoelectric .....	1
Modification of eutectic Ge phase .....	5
Network calculations.....	45
Neutron target .....	27
Neutron-induced reactions.....	27
Nuclear astrophysics .....	45
Nuclear physics.....	45
Nucleosynthesis .....	27
Percolation.....	35
Presolar grains .....	45
Scanning electron microscopy.....	5
Storage rings .....	27



**المراجع:** يجب طباعة المراجع بأسطر مزدوجة ومرقمة حسب تسلسلها في النص. وتكتب المراجع في النص بين قوسين مربعين. ويتم اعتماد اختصارات الدوريات حسب نظام Wordlist of Scientific Reviewers.

**الجدول:** تعطى الجداول أرقاماً متسلسلة يشار إليها في النص. ويجب طباعة كل جدول على صفحة منفصلة مع عنوان فوق الجدول. أما الحواشي التفسيرية، التي يشار إليها بحرف فوقي، فتكتب أسفل الجدول.

**الرسوم التوضيحية:** يتم ترقيم الأشكال والرسومات والرسومات البيانية (المخططات) والصور، بصورة متسلسلة كما وردت في النص.

تقبل الرسوم التوضيحية المستخرجة من الحاسوب والصور الرقمية ذات النوعية الجيدة بالأبيض والأسود، على أن تكون أصيلة وليست نسخة عنها، وكل منها على ورقة منفصلة ومعرفة برقمها بالمقابل. ويجب تزويد المجلة بالرسومات بحجمها الأصلي بحيث لا تحتاج إلى معالجة لاحقة، وألا تقل الحروف عن الحجم 8 من نوع Times New Roman، وألا تقل سماكة الخطوط عن 0.5 وبكثافة متجانسة. ويجب إزالة جميع الألوان من الرسومات ما عدا تلك التي ستنشر ملونة. وفي حالة إرسال الرسومات بصورة رقمية، يجب أن تتوافق مع متطلبات الحد الأدنى من التمايز (1200 dpi Resolution) لرسومات الأبيض والأسود الخطية، و 600 dpi للرسومات باللون الرمادي، و300 dpi للرسومات الملونة. ويجب تخزين جميع ملفات الرسومات على شكل (jpg)، وأن ترسل الرسوم التوضيحية بالحجم الفعلي الذي سيظهر في المجلة. وسواء أرسل المخطوط بالبريد أو عن طريق الشبكة (Online)، يجب إرسال نسخة ورقية أصلية ذات نوعية جيدة للرسومات التوضيحية.

**مواد إضافية:** تشجع المجلة الباحثين على إرفاق جميع المواد الإضافية التي يمكن أن تسهل عملية التحكيم. وتشمل المواد الإضافية أي اشتقاقات رياضية مفصلة لا تظهر في المخطوط.

**المخطوط المنقح (المعدل) والأقراص المدمجة:** بعد قبول البحث للنشر وإجراء جميع التعديلات المطلوبة، فعلى الباحثين تقديم نسخة أصلية ونسخة أخرى مطابقة للأصلية مطبوعة بأسطر مزدوجة، وكذلك تقديم نسخة إلكترونية تحتوي على المخطوط كاملاً مكتوباً على Microsoft Word for Windows 2000 أو ما هو استجد منه. ويجب إرفاق الأشكال الأصلية مع المخطوط النهائي المعدل حتى لو تم تقديم الأشكال إلكترونياً. وتخزن جميع ملفات الرسومات على شكل (jpg)، وتقدم جميع الرسومات التوضيحية بالحجم الحقيقي الذي ستظهر به في المجلة. ويجب إرفاق قائمة ببرامج الحاسوب التي استعملت في كتابة النص، وأسماء الملفات على قرص مدمج، حيث يعلم القرص بالاسم الأخير للباحث، وبالرقم المرجعي للمخطوط للمراسلة، وعنوان المقالة، والتاريخ. ويحفظ في مغلف واقٍ.



### حقوق الطبع

يُشكّل تقديم مخطوط البحث للمجلة اعترافاً صريحاً من الباحثين بأن مخطوط البحث لم يُنشر ولم يُقدّم للنشر لدى أي جهة أخرى كانت وبأي صيغة ورقية أو إلكترونية أو غيرها. ويشترط على الباحثين ملء نموذج يُنصّ على نقل حقوق الطبع لتصبح ملكاً لجامعة البرموك قبل الموافقة على نشر المخطوط. ويقوم رئيس التحرير بتزويد الباحثين بإنموذج نقل حقوق الطبع مع النسخة المرسلة للتتقيح. كما ويُمنع إعادة إنتاج أي جزء من الأعمال المنشورة في المجلة من دون إذن خطّي مُسبق من رئيس التحرير.

### إخلاء المسؤولية

إن ما ورد في هذه المجلة يعبر عن آراء المؤلفين، ولا يعكس بالضرورة آراء هيئة التحرير أو الجامعة أو سياسة اللجنة العليا للبحث العلمي أو وزارة التعليم العالي والبحث العلمي. ولا يتحمل ناشر المجلة أي تبعات مادية أو معنوية أو مسؤوليات عن استعمال المعلومات المنشورة في المجلة أو سوء استعمالها.

الفهرسة: المجلة مفهرسة في:

	<b>Emerging Sources Citation Index (ESCI)</b>	
---	---	---

## معلومات عامة

المجلة الأردنية للفيزياء هي مجلة بحوث علمية عالمية متخصصة مُحكمة تصدر بدعم من صندوق دعم البحث العلمي، وزارة التعليم العالي والبحث العلمي، عمان، الأردن. وتقوم بنشر المجلة عمادة البحث العلمي والدراسات العليا في جامعة اليرموك، إربد، الأردن. وتُنشر البحوث العلمية الأصلية، إضافة إلى المراسلات القصيرة Short Communications، والملاحظات الفنية Technical Notes، والمقالات الخاصة Feature Articles، ومقالات المراجعة Review Articles، في مجالات الفيزياء النظرية والتجريبية، باللغتين العربية والإنجليزية.

## تقديم مخطوط البحث

تقدم البحوث عن طريق إرسالها إلى البريد الإلكتروني : [jjp@yu.edu.jo](mailto:jjp@yu.edu.jo)

تقديم المخطوطات إلكترونياً: اتبع التعليمات في موقع المجلة على الشبكة العنكبوتية.

ويجري تحكيم البحوث الأصلية والمراسلات القصيرة والملاحظات الفنية من جانب مُحكمين اثنين في الأقل من ذوي الاختصاص والخبرة. وتُشجّع المجلة الباحثين على اقتراح أسماء المحكمين. أما نشر المقالات الخاصة في المجالات الفيزيائية النشطة، فيتم بدعوة من هيئة التحرير، ويُشار إليها كذلك عند النشر. ويُطلب من كاتب المقال الخاص تقديم تقرير واضح يتسم بالدقة والإيجاز عن مجال البحث تمهيداً للمقال. وتُنشر المجلة أيضاً مقالات المراجعة في الحقول الفيزيائية النشطة سريعة التغير، وتُشجّع كاتبي مقالات المراجعة أو مُستكثبيها على إرسال مقترح من صفحتين إلى رئيس التحرير. ويُرفق مع البحث المكتوب باللغة العربية ملخص (Abstract) وكلمات دالة (Keywords) باللغة الإنجليزية.

## ترتيب مخطوط البحث

يجب أن تتم طباعة مخطوط البحث بنظ 12 نوعه Times New Roman، وبسطر مزدوج، على وجه واحد من ورق A4 (21.6 × 27.9 سم) مع حواشي 3.71 سم، باستخدام معالج كلمات ميكروسوفت وورد 2000 أو ما استُجد منه. ويجري تنظيم أجزاء المخطوط وفق الترتيب التالي: صفحة العنوان، الملخص، رموز التصنيف (PACS)، المقدمة، طرق البحث، النتائج، المناقشة، الخلاصة، الشكر والعرفان، المراجع، الجداول، قائمة بدليل الأشكال والصور والإيضاحات، ثم الأشكال والصور والإيضاحات. وتُكتب العناوين الرئيسية بخط غامق، بينما تُكتب العناوين الفرعية بخط مانل.

صفحة العنوان: وتشمل عنوان المقالة، أسماء الباحثين الكاملة وعناوين العمل كاملة. ويكتب الباحث المسؤول عن المراسلات اسمه مشاراً إليه بنجمة، والبريد الإلكتروني الخاص به. ويجب أن يكون عنوان المقالة موجزاً وواضحاً ومعبراً عن فحوى (محتوى) المخطوط، وذلك لأهمية هذا العنوان لأغراض استرجاع المعلومات.

الملخص: المطلوب كتابة فقرة واحدة لا تزيد على مائتي كلمة، موضحة هدف البحث، والمنهج المتبع فيه والنتائج وأهم ما توصل إليه الباحثون.

الكلمات الدالة: يجب أن يلي الملخص قائمة من 4-6 كلمات دالة تعبر عن المحتوى الدقيق للمخطوط لأغراض الفهرسة.

PACS: يجب إرفاق الرموز التصنيفية، وهي متوافرة في الموقع <http://www.aip.org/pacs/pacs06/pacs06-toc.html>.

المقدمة: يجب أن توضّح الهدف من الدراسة وعلاقتها بالأعمال السابقة في المجال، لا أن تكون مراجعة مكثفة لما نشر (لا تزيد المقدمة عن صفحة ونصف الصفحة مطبوعة).

طرائق البحث (التجريبية / النظرية): يجب أن تكون هذه الطرائق موضحة بتفصيل كاف لإتاحة إعادة إجرائها بكفاءة، ولكن باختصار مناسب، حتى لا تكون تكراراً للطرائق المنشورة سابقاً.

النتائج: يستحسن عرض النتائج على صورة جداول وأشكال حيثما أمكن، مع شرح قليل في النص ومن دون مناقشة تفصيلية.

المناقشة: يجب أن تكون موجزة وتركز على تفسير النتائج.

الاستنتاج: يجب أن يكون وصفاً موجزاً لأهم ما توصلت إليه الدراسة ولا يزيد عن صفحة مطبوعة واحدة.

الشكر والعرفان: الشكر والإشارة إلى مصدر المنح والدعم المالي يكتبان في فقرة واحدة تسبق المراجع مباشرة.



Subscription Form

Jordan Journal of  
**PHYSICS**

An International Peer-Reviewed Research Journal issued by the  
Support of the Scientific Research Support Fund

Published by the Deanship of Research & Graduate Studies, Yarmouk University, Irbid, Jordan

Name: ..... الأسم:  
Specialty:..... التخصص:  
Address: ..... العنوان:  
P.O. Box:..... صندوق البريد:  
City & Postal Code: ..... المدينة/الرمز البريدي:  
Country: ..... الدولة:  
Phone: ..... رقم الهاتف:  
Fax No:..... رقم الفاكس:  
E-mail:..... البريد الإلكتروني:  
No. of Subscription: ..... عدد الاشتراكات:  
Method of Payment:..... طريقة الدفع:  
Amount Enclosed:..... المبلغ المرفق:  
Signature: ..... التوقيع:

Cheques should be paid to Deanship of Research and Graduate Studies - Yarmouk University.

I would like to subscribe to the Journal  
For

- One Year  
 Two Years  
 Three Years

**One Year Subscription Rates**

	Inside Jordan	Outside Jordan
Individuals	JD 8	€ 40
Students	JD 4	€ 20
Institutions	JD 12	€ 60

**Correspondence**

**Subscriptions and Sales:**

**Prof. Ibrahim O. Abu Al-Jarayesh**  
Deanship of Research and Graduate Studies  
Yarmouk University  
Irbid – Jordan  
**Telephone:** 00 962 2 711111 Ext. 2075  
**Fax No.:** 00 962 2 7211121





جامعة اليرموك



المملكة الأردنية الهاشمية

المجلة الأردنية  
**للفيزياء**

مجلة بحوث علمية عالمية متخصصة محكمة  
تصدر بدعم من صندوق دعم البحث العلمي

عدد خاص

المجلة الأردنية  
**للفيزياء**  
مجلة بحوث علمية عالمية محكمة

المجلد (11)، العدد (1)، نيسان 2018م / شعبان 1439هـ

المجلة الأردنية للفيزياء: مجلة علمية عالمية متخصصة محكمة تصدر بدعم من صندوق دعم البحث العلمي، عمان، الأردن، وتصدر عن عمادة البحث العلمي والدراسات العليا، جامعة اليرموك، إربد، الأردن.

رئيس التحرير:

ابراهيم عثمان أبو الجرايش  
قسم الفيزياء، جامعة اليرموك، إربد، الأردن.  
[ijaraysh@yu.edu.jo](mailto:ijaraysh@yu.edu.jo)

هيئة التحرير:

ضياء الدين محمود عرفة  
رئيس جامعة آل البيت، المفرق، الأردن.  
[darafah@ju.edu.jo](mailto:darafah@ju.edu.jo)

نبيل يوسف أيوب  
رئيس الجامعة الأمريكية في مادبا، مادبا، الأردن.  
[nabil.ayoub@gju.edu.jo](mailto:nabil.ayoub@gju.edu.jo)

جميل محمود خليفة  
قسم الفيزياء، الجامعة الأردنية، عمان، الأردن.  
[jkalifa@ju.edu.jo](mailto:jkalifa@ju.edu.jo)

سامي حسين محمود  
قسم الفيزياء، الجامعة الأردنية، عمان، الأردن.  
[s.mahmood@ju.edu.jo](mailto:s.mahmood@ju.edu.jo)

نهاده عبدالرؤوف يوسف  
قسم الفيزياء، جامعة الأميرة سمية للتكنولوجيا، عمان، الأردن  
[o.n.yusuf@psut.edu.jo](mailto:o.n.yusuf@psut.edu.jo)

مروان سليمان موسى  
قسم الفيزياء، جامعة مؤتة، الكرك، الأردن.  
[mmousa@mutah.edu.jo](mailto:mmousa@mutah.edu.jo)

أكرم عبد المجيد الروسان  
قسم الفيزياء التطبيقية، جامعة العلوم والتكنولوجيا الأردنية، إربد، الأردن.  
[akram@just.edu.jo](mailto:akram@just.edu.jo)

محمد خالد الصغير  
قسم الفيزياء، الجامعة الهاشمية، الزرقاء، الأردن.  
[msugh@hu.edu.jo](mailto:msugh@hu.edu.jo)

سكرتير التحرير: مجدي الشناق

ترسل البحوث إلى العنوان التالي:

الأستاذ الدكتور إبراهيم عثمان أبو الجرايش  
رئيس تحرير المجلة الأردنية للفيزياء  
عمادة البحث العلمي والدراسات العليا، جامعة اليرموك  
إربد، الأردن

هاتف 00 962 2 7211111 فرعي 2075

E-mail: [jjp@yu.edu.jo](mailto:jjp@yu.edu.jo) Website: <http://Journals.yu.edu.jo/jjp>